UNIVERSITY OF CALIFORNIA SAN DIEGO

Measuring the Polarization of the Cosmic Microwave Background with POLARBEAR-1 and Developing the Next-Generation Experiment POLARBEAR-2

A dissertation submitted in partial satisfaction of the
requirements for the degree
Doctor of Philosophy

in

Physics

by

Tucker James Elleflot

Committee in charge:

Professor Brian Keating, Chair
Professor Kam Arnold
Professor Craig Callender
Professor Thomas Murphy
Professor Daniel Sievenpiper

2019

The dissertation of Tucker James Elleflot is approved, and it is acceptable in quality and form for publication on microfilm and electronically:

_____

_____

_____

_____

_____

Chair

University of California San Diego

2019

TABLE OF CONTENTS

LIST OF FIGURES

LIST OF TABLES

ACKNOWLEDGEMENTS

This work would not have been possible without the love, support, and encouragement of my mom, my dad, my wonderful girlfriend Elena, and my friend Luke.

Thank you to Brian and Kam for the guidance throughout the last six years. The opportunity to work in this field with such esteemed mentors has been a dream come true for me.

To all my lab mates, past and present: thank you for the good times, for the interesting conversations, for challenging me intellectually. I'm sad to be leaving our lab, but I don't expect that this is the end of the line for us. I hope to see you all again at conferences, collaboration meetings, and at 17,000 feet.

Chapter 2 contains a reprint of material as it appears in S. Adachi, M. A. O. A. Faundez, K. Arnold, C. Baccigalupi, D. Barron, D. Beck, S. Beckman, F. Bianchini, D. Boettger, J. Borrill, J. Carron, S. Chapman, K. Cheung, Y. Chinone, K. Crowley, A. Cukierman, M. Dobbs, H. E. Bouhargani, T. Elleflot, J. Errard, G. Fabbian, C. Feng, T. Fujino, N. Galitzki, N. Goeckner-Wald, J. Groh, G. Hall, N. Halverson, T. Hamada, M. Hasegawa, M. Hazumi, C. A. Hill, L. Howe, Y. Inoue, G. Jaehnig, O. Jeong, D. Kaneko, N. Katayama, B. Keating, R. Keskitalo, S. Kikuchi, T. Kisner, N. Krachmalnicoff, A. Kusaka, A. T. Lee, D. Leon, E. Linder, L. N. Lowry, A. Mangu, F. Matsuda, Y. Minami, M. Navaroli, H. Nishino, A. T. P. Pham, D. Poletti, G. Puglisi, C. L. Reichardt, Y. Segawa, M. Silva-Feaver, P. Siritanasak, N. Stebor, R. Stompor, A. Suzuki, O. Tajima, S. Takakura, S. Takatori, D. Tanabe, G. P. Teply, C. Tsai, C. Verges, B. Westbrook, and Y. Zhou, "A measurement of the degree scale cmb b-mode angular power spectrum with polarbear," 2019. Submitted to The Astrophysical Journal. The dissertation author made essential contributions to this work.

Chapter 4 contains an updated reprint of material as it appears in T. Elleflot, Y. Akiba, K. Arnold, J. Avva, D. Barron, A. N. Bender, A. Cukierman, T. deHaan, M. Dobbs, J. Groh, M. Hasegawa, M. Hazumi, W. Holzapfel, L. Howe, G. Jaehnig, B. Keating, A. Kusaka, A. T. Lee, L.

Lowry, J. Montgomery, H. Nishino, C. Raum, K. M. Rotermund, M. Silva-Feaver, A. Suzuki, B. Westbrook, and N. Whitehorn, "Detector and readout assembly and characterization for the simons array," Journal of Low Temperature Physics, vol. 193, pp. 1094–1102, Dec 2018. The dissertation author was the primary author of this work.

Chapter 5 contains an updated reprint of material as it appears in T. Elleflot, Y. Akiba, K. Arnold, J. Avva, D. Barron, A. N. Bender, A. Cukierman, T. deHaan, M. Dobbs, J. Groh, M. Hasegawa, M. Hazumi, W. Holzapfel, L. Howe, G. Jaehnig, B. Keating, A. Kusaka, A. T. Lee, L. Lowry, J. Montgomery, H. Nishino, C. Raum, K. M. Rotermund, M. Silva-Feaver, A. Suzuki, B. Westbrook, and N. Whitehorn, "Detector and readout assembly and characterization for the simons array," Journal of Low Temperature Physics, vol. 193, pp. 1094–1102, Dec 2018. The dissertation author was the primary author of this work.

Chapter 5 contains an updated reprint of material as it appears in T. Elleflot, K. Arnold, D. Barron, K. T. Crowley, M. Dobbs, J. Groh, M. Hasegawa, M. Hazumi, C. Hill, L. Howe, J. Ito, O. Jeong, D. Kaneko, N. Katayama, B. Keating, A. Kusaka, A. T. Lee, L. N. Lowry, C. Raum, J. Seibert, M. Silva-Feaver, P. Siritanasak, A. Suzuki, S. Takakura, S. Takatori, C. Tsai, B. Westbrook. "Effect of Stray Impedance in Frequency-Division Multiplexed Readout of TES Sensors in POLARBEAR-2B." Submitted to Journal of Low Temperature Physics. The dissertation author was the primary author of this work.

VITA

2011	B. S. in Physics, University of California Santa Barbara
2015	M. S. in Physics, University of California San Diego
2019	Ph. D. in Physics, University of California San Diego

PUBLICATIONS

T. Elleflot, Y. Akiba, K. Arnold, J. Avva, D. Barron, A. N. Bender, A. Cukierman, T. de Haan, M. Dobbs, J. Groh, M. Hasegawa, M. Hazumi, W. Holzapfel, L. Howe, G. Jaehnig, B. Keating, A. Kusaka, A. T. Lee, L. Lowry, J. Montgomery, H. Nishino, C. Raum, K. M. Rotermund, M. Silva-Feaver, A. Suzuki, B. Westbrook, and N. Whitehorn, "Detector and readout assembly and characterization for the simons array," Journal of Low Temperature Physics, vol. 193, pp. 1094–1102, Dec 2018.

S. Adachi, M. A. O. A. Faundez, K. Arnold, C. Baccigalupi, D. Barron, D. Beck, S. Beck- man, F. Bianchini, D. Boettger, J. Borrill, J. Carron, S. Chapman, K. Cheung, Y. Chinone, K. Crowley, A. Cukierman, M. Dobbs, H. E. Bouhargani, T. Elleflot, J. Errard, G. Fab- bian, C. Feng, T. Fujino, N. Galitzki, N. Goeckner-Wald, J. Groh, G. Hall, N. Halverson, T. Hamada, M. Hasegawa, M. Hazumi, C. A. Hill, L. Howe, Y. Inoue, G. Jaehnig, O. Jeong, D. Kaneko, N. Katayama, B. Keating, R. Keskitalo, S. Kikuchi, T. Kisner, N. Krachmal- nicoff, A. Kusaka, A. T. Lee, D. Leon, E. Linder, L. N. Lowry, A. Mangu, F. Matsuda, Y. Minami, M. Navaroli, H. Nishino, A. T. P. Pham, D. Poletti, G. Puglisi, C. L. Reichardt, Y. Segawa, M. Silva-Feaver, P. Siritanasak, N. Stebor, R. Stompor, A. Suzuki, O. Tajima, S. Takakura, S. Takatori, D. Tanabe, G. P. Teply, C. Tsai, C. Verges, B. Westbrook, and Y. Zhou, "A measurement of the degree scale cmb b-mode angular power spectrum with polarbear," 2019.

S. Adachi, M. A. O. A. Faundez, Y. Akiba, A. Ali, K. Arnold, C. Baccigalupi, D. Barron, D. Beck, F. Bianchini, J. Borrill, J. Carron, K. Cheung, Y. Chinone, K. Crowley, H. E. Bouhargani, T. Elleflot, J. Errard, G. Fabbian, C. Feng, T. Fujino, N. Goeckner-Wald, M. Hasegawa, M. Hazumi, C. A. Hill, L. Howe, N. Katayama, B. Keating, S. Kikuchi, A. Kusaka, A. T. Lee, D. Leon, E. Linder, L. N. Lowry, F. Matsuda, T. Matsumura, Y. Mi- nami, T. Namikawa, H. Nishino, J. Peloton, A. T. P. Pham, D. Poletti, G. Puglisi, C. L. Re- ichardt, Y. Segawa, B. D. Sherwin, M. Silva-Feaver, P. Siritanasak, R. Stompor, O. Tajima, S. Takatori, D. Tanabe, G. P. Teply, and C. Verges, "Internal delensing of cosmic microwave background polarization b-modes with the polarbear experiment," 2019.

F. Matsuda, L. Lowry, A. Suzuki, M. A. Fa'undez, K. Arnold, D. Barron, F. Bian- chini, K. Cheung, Y. Chinone, T. Elleflot, G. Fabbian, N. Goeckner-Wald, M. Hasegawa, D. Kaneko, N. Katayama, B. Keating, A. Lee, M. Navaroli, H. Nishino, H. Paar, G. Puglisi, P. Richards, J. Seibert, P. Siritanasak, O. Tajima, S. Takatori, C. Tsai, and B. Westbrook, "The polarbear fourier transform spectrometer calibrator and spectroscopic characterization of the polarbear instrument," 2019.

T. Namikawa, Y. Chinone, H. Miyatake, M. Oguri, R. Takahashi, A. Kusaka, N. Katayama, S. Adachi, M. Aguilar, H. Aihara, A. Ali, R. Armstrong, K. Arnold, C. Baccigalupi, D. Bar- ron, D. Beck, S. Beckman, F. Bianchini, D. Boettger, J. Borrill, K. Cheung, L. Cor- bett, K. T. Crowley, H. E. Bouhargani, T. Elleflot, J. Errard, G. Fabbian, C. Feng, N. Galitzki, N. Goeckner-Wald, J. Groh, T. Hamada, M. Hasegawa, M. Hazumi, C. Hill, L. Howe, O. Jeong, D. Kaneko, B. Keating, A. T. Lee, D. Leon, E. Linder, L. N. Lowry, A. Mangu, F. Matsuda, Y. Minami, S. Miyazaki, H. Murayama, M. Navaroli, H. Nishino, A. J. Nishizawa, A. T. P. Pham, D. Poletti, G. Puglisi, C. L. Reichardt, B. D. Sherwin, M. Silva-Feaver, P. Siritanasak, J. S. Speagle, R. Stompor, A. Suzuki, P. J. Tait, O. Tajima, M. Takada, S. Takakura, S. Takatori, D. Tanabe, M. Tanaka, G. P. Teply, C. Tsai, C. Verges, B. Westbrook, Y. Zhou, T. P. Collaboration, and the Subaru HSC SSP Collaboration, "Ev- idence for the cross-correlation between cosmic microwave background polarization lensing from polarbear and cosmic shear from subaru hyper suprime-cam," The Astrophysical Jour- nal, vol. 882, p. 62, Sep 2019.

M. A. Faundez, K. Arnold, C. Baccigalupi, D. Barron, D. Beck, F. Bianchini, D. Boettger, J. Borrill, J. Carron, K. Cheung, Y. Chinone, H. E. Bouhargani, T. Elleflot, J. Errard, G. Fabbian, C. Feng, N. Galitzki, N. Goeckner-Wald, M. Hasegawa, M. Hazumi, L. Howe, D. Kaneko, N. Katayama, B. Keating, N. Krachmalnicoff, A. Kusaka, A. T. Lee, D. Leon, E. Linder, L. N. Lowry, F. Matsuda, Y. Minami, M. Navaroli, H. Nishino, A. T. P. Pham, D. Poletti, G. Puglisi, C. L. Reichardt, B. D. Sherwin, M. Silva-Feaver, R. Stompor, A. Suzuki, O. Tajima, S. Takakura, S. Takatori, G. P. Teply, C. Tsai, and C. Verges, "Cross-correlation of polarbear cmb polarization lensing with high-z sub-mm herschel-atlas galaxies," 2019.

M. Hazumi, P. A. R. Ade, Y. Akiba, D. Alonso, K. Arnold, J. Aumont, C. Baccigalupi, D. Barron, S. Basak, S. Beckman, J. Borrill, F. Boulanger, M. Bucher, E. Calabrese, Y. Chinone, S. Cho, A. Cukierman, D. W. Curtis, T. de Haan, M. Dobbs, A. Domin- jon, T. Dotani, L. Duband, A. Ducout, J. Dunkley, J. M. Duval, T. Elleflot, H. K. Eriksen, J. Errard, J. Fischer, T. Fujino, T. Funaki, U. Fuskeland, K. Ganga, N. Goeckner-Wald, J. Grain, N. W. Halverson, T. Hamada, T. Hasebe, M. Hasegawa, K. Hattori, M. Hattori, L. Hayes, N. Hidehira, C. A. Hill, G. Hilton, J. Hubmayr, K. Ichiki, T. Iida, H. Imada, M. Inoue, Y. Inoue, K. D. Irwin, H. Ishino, O. Jeong, H. Kanai, D. Kaneko, S. Kashima, N. Katayama, T. Kawasaki, S. A. Kernasovskiy, R. Keskitalo, A. Kibayashi, Y. Kida, K. Kimura, T. Kisner, K. Kohri, E. Komatsu, K. Komatsu, C. L. Kuo, N. A. Kurinsky, A. Kusaka, A. Lazarian, A. T. Lee, D. Li, E. Linder, B. Maffei, A. Mangilli, M. Maki, T. Matsumura, S. Matsuura, D. Meilhan, S. Mima, Y. Minami, K. Mitsuda, L. Montier, M. Nagai, T. Nagasaki, R. Nagata, M. Nakajima, S. Nakamura, T. Namikawa, M. Naruse, H. Nishino, T. Nitta, T. Noguchi, H. Ogawa, S. Oguri, N. Okada, A. Okamoto, T. Okamura, C. Otani, G. Patanchon, G. Pisano, G. Rebeiz, M. Remazeilles, P. L. Richards, S. Sakai, Y. Sakurai, Y. Sato, N. Sato, M. Sawada, Y. Segawa, Y. Sekimoto, U. Seljak, B. D. Sher- win, T. Shimizu, K. Shinozaki, R. Stompor, H. Sugai, H. Sugita, A. Suzuki, J. Suzuki, O. Tajima, S. Takada, R. Takaku, S. Takakura, S. Takatori, D. Tanabe, E. Taylor, K. L. Thompson, B. Thorne, T. Tomaru, T. Tomida, N. Tomita, M. Tristram, C. Tucker, P. Turin, M. Tsujimoto, S. Uozumi, S. Utsunomiya, Y. Uzawa, F. Vansyngel, I. K. Wehus, B. West- brook, M. Willer, N. Whitehorn, Y. Yamada, R. Yamamoto, N. Yamasaki, T. Yamashita, and M. Yoshida, "Litebird: A satellite for the studies of b-mode polarization and inflation from cosmic background radiation detection," Journal of Low

Temperature Physics, vol. 194, pp. 443–452, Mar 2019.

S. Takakura, M. A. O. Aguilar-Faundez, Y. Akiba, K. Arnold, C. Baccigalupi, D. Bar- ron, D. Beck, F. Bianchini, D. Boettger, J. Borrill, K. Cheung, Y. Chinone, T. Elleflot, J. Errard, G. Fabbian, C. Feng, N. Goeckner-Wald, T. Hamada, M. Hasegawa, M. Hazumi, L. Howe, D. Kaneko, N. Katayama, B. Keating, R. Keskitalo, T. Kisner, N. Krachmalnicoff, A. Kusaka, A. T. Lee, L. N. Lowry, F. T. Matsuda, A. J. May, Y. Minami, M. Navaroli, H. Nishino, L. Piccirillo, D. Poletti, G. Puglisi, C. L. Reichardt, Y. Segawa, M. Silva-Feaver, P. Siritanasak, A. Suzuki, O. Tajima, S. Takatori, D. Tanabe, G. P. Teply, and C. Tsai, "Measurements of tropospheric ice clouds with a ground-based CMB polarization experi- ment, POLARBEAR," The Astrophysical Journal, vol. 870, p. 102, jan 2019.

B. Westbrook, P. A. R. Ade, M. Aguilar, Y. Akiba, K. Arnold, C. Baccigalupi, D. Barron, D. Beck, S. Beckman, A. N. Bender, F. Bianchini, D. Boettger, J. Borrill, S. Chapman, Y. Chinone, G. Coppi, K. Crowley, A. Cukierman, T. de Haan, R. Dunner, M. Dobbs, T. Elleflot, J. Errard, G. Fabbian, S. M. Feeney, C. Feng, G. Fuller, N. Galitzki, A. Gilbert, N. Goeckner-Wald, J. Groh, N. W. Halverson, T. Hamada, M. Hasegawa, M. Hazumi, C. A. Hill, W. Holzapfel, L. Howe, Y. Inoue, G. Jaehnig, A. Jaffe, O. Jeong, D. Kaneko, N. Katayama, B. Keating, R. Keskitalo, T. Kisner, N. Krachmalnicoff, A. Kusaka, M. Le Je- une, A. T. Lee, D. Leon, E. Linder, L. Lowry, A. Madurowicz, D. Mak, F. Matsuda, A. May, N. J. Miller, Y. Minami, J. Montgomery, M. Navaroli, H. Nishino, J. Peloton, A. Pham, L. Piccirillo, D. Plambeck, D. Poletti, G. Puglisi, C. Raum, G. Rebeiz, C. L. Reichardt, P. L. Richards, H. Roberts, C. Ross, K. M. Rotermund, Y. Segawa, B. Sherwin, M. Silva-Feaver, P. Siritanasak, R. Stompor, A. Suzuki, O. Tajima, S. Takakura, S. Takatori, D. Tanabe, R. Tat, G. P. Teply, A. Tikhomirov, T. Tomaru, C. Tsai, N. Whitehorn, and A. Zahn, "The polarbear-2 and simons array focal plane fabrication status," Journal of Low Temperature Physics, vol. 193, pp. 758–770, Dec 2018.

T. Hasebe, S. Kashima, P. A. R. Ade, Y. Akiba, D. Alonso, K. Arnold, J. Aumont, C. Bacci- galupi, D. Barron, S. Basak, S. Beckman, J. Borrill, F. Boulanger, M. Bucher, E. Calabrese, Y. Chinone, H.-M. Cho, A. Cukierman, D. W. Curtis, T. de Haan, M. Dobbs, A. Dominjon, T. Dotani, L. Duband, A. Ducout, J. Dunkley, J. M. Duval, T. Elleflot, H. K. Eriksen, J. Er- rard, J. Fischer, T. Fujino, T. Funaki, U. Fuskeland, K. Ganga, N. Goeckner-Wald, J. Grain, N. W. Halverson, T. Hamada, M. Hasegawa, K. Hattori, M. Hattori, L. Hayes, M. Hazumi, N. Hidehira, C. A. Hill, G. Hilton, J. Hubmayr, K. Ichiki, T. Iida, H. Imada, M. Inoue, Y. In- oue, K. D. Irwin, H. Ishino, O. Jeong, H. Kanai, D. Kaneko, N. Katayama, T. Kawasaki, S. A. Kernasovskiy, R. Keskitalo, A. Kibayashi, Y. Kida, K. Kimura, T. Kisner, K. Kohri, E. Komatsu, K. Komatsu, C. L. Kuo, N. A. Kurinsky, A. Kusaka, A. Lazarian, A. T. Lee, D. Li, E. Linder, B. Maffei, A. Mangilli, M. Maki, T. Matsumura, S. Matsuura, D. Meilhan, S. Mima, Y. Minami, K. Mitsuda, L. Montier, M. Nagai, T. Nagasaki, R. Nagata, M. Naka- jima, S. Nakamura, T. Namikawa, M. Naruse, H. Nishino, T. Nitta, T. Noguchi, H. Ogawa, S. Oguri, N. Okada, A. Okamoto, T. Okamura, C. Otani, G. Patanchon, G. Pisano, G. Re- beiz, M. Remazeilles, P. L. Richards, S. Sakai, Y. Sakurai, Y. Sato, N. Sato, M. Sawada, Y. Segawa, Y. Sekimoto, U. Seljak, B. D. Sherwin, T. Shimizu, K. Shinozaki, R. Stompor, H. Sugai, H. Sugita, A. Suzuki, J. Suzuki, O. Tajima, S. Takada, R. Takaku, S. Takakura, S. Takatori, D. Tanabe, E. Taylor, K. L. Thompson, B. Thorne, T.

Tomaru, T. Tomida, N. Tomita, M. Tristram, C. Tucker, P. Turin, M. Tsujimoto, S. Uozumi, S. Utsunomiya, Y. Uzawa, F. Vansyngel, I. K. Wehus, B. Westbrook, M. Willer, N. Whitehorn, Y. Yamada, R. Yamamoto, N. Yamasaki, T. Yamashita, and M. Yoshida, "Concept study of optical con- figurations for high-frequency telescope for litebird," Journal of Low Temperature Physics, vol. 193, pp. 841–850, Dec 2018.

A. Suzuki, P. A. R. Ade, Y. Akiba, D. Alonso, K. Arnold, J. Aumont, C. Baccigalupi, D. Barron, S. Basak, S. Beckman, J. Borrill, F. Boulanger, M. Bucher, E. Calabrese, Y. Chi- none, S. Cho, B. Crill, A. Cukierman, D. W. Curtis, T. de Haan, M. Dobbs, A. Dominjon, T. Dotani, L. Duband, A. Ducout, J. Dunkley, J. M. Duval, T. Elleflot, H. K. Eriksen, J. Errard, J. Fischer, T. Fujino, T. Funaki, U. Fuskeland, K. Ganga, N. Goeckner-Wald, J. Grain, N. W. Halverson, T. Hamada, T. Hasebe, M. Hasegawa, K. Hattori, M. Hattori, L. Hayes, M. Hazumi, N. Hidehira, C. A. Hill, G. Hilton, J. Hubmayr, K. Ichiki, T. Iida, H. Imada, M. Inoue, Y. Inoue, K. D. Irwin, H. Ishino, O. Jeong, H. Kanai, D. Kaneko, S. Kashima, N. Katayama, T. Kawasaki, S. A. Kernasovskiy, R. Keskitalo, A. Kibayashi, Y. Kida, K. Kimura, T. Kisner, K. Kohri, E. Komatsu, K. Komatsu, C. L. Kuo, N. A. Kurin- sky, A. Kusaka, A. Lazarian, A. T. Lee, D. Li, E. Linder, B. Maffei, A. Mangilli, M. Maki, T. Matsumura, S. Matsuura, D. Meilhan, S. Mima, Y. Minami, K. Mitsuda, L. Montier, M. Nagai, T. Nagasaki, R. Nagata, M. Nakajima, S. Nakamura, T. Namikawa, M. Naruse, H. Nishino, T. Nitta, T. Noguchi, H. Ogawa, S. Oguri, N. Okada, A. Okamoto, T. Okamura, C. Otani, G. Patanchon, G. Pisano, G. Rebeiz, M. Remazeilles, P. L. Richards, S. Sakai, Y. Sakurai, Y. Sato, N. Sato, M. Sawada, Y. Segawa, Y. Sekimoto, U. Seljak, B. D. Sher- win, T. Shimizu, K. Shinozaki, R. Stompor, H. Sugai, H. Sugita, J. Suzuki, O. Tajima, S. Takada, R. Takaku, S. Takakura, S. Takatori, D. Tanabe, E. Taylor, K. L. Thompson, B. Thorne, T. Tomaru, T. Tomida, N. Tomita, M. Tristram, C. Tucker, P. Turin, M. Tsu- jimoto, S. Uozumi, S. Utsunomiya, Y. Uzawa, F. Vansyngel, I. K. Wehus, B. Westbrook, M. Willer, N. Whitehorn, Y. Yamada, R. Yamamoto, N. Yamasaki, T. Yamashita, and M. Yoshida, "The litebird satellite mission: Sub-kelvin instrument," Journal of Low Tem- perature Physics, vol. 193, pp. 1048–1056, Dec 2018.

J. S. Avva, P. A. R. Ade, Z. Ahmed, A. J. Anderson, J. E. Austermann, R. B. Thakur, D. Barron, A. N. Bender, B. A. Benson, J. E. Carlstrom, F. W. Carter, T. Cecil, C. L. Chang, J. F. Cliche, A. Cukierman, E. V. Denison, T. de Haan, J. Ding, M. A. Dobbs, D. Dutcher, T. Elleflot, W. Everett, A. Foster, R. N. Gannon, A. Gilbert, J. C. Groh, N. W. Halverson, A. H. Harke-Hosemann, N. L. Harrington, M. Hasegawa, K. Hattori, J. W. Henning, G. C. Hilton, W. L. Holzapfel, Y. Hori, N. Huang, K. D. Irwin, O. B. Jeong, M. Jonas, T. Khaire, A. M. Kofman, M. Korman, D. Kubik, S. Kuhlmann, C. L. Kuo, A. T. Lee, A. E. Lowitz, S. S. Meyer, J. Montgomery, A. Nadolski, T. Natoli, H. Nguyen, H. Nishino, G. I. Noble, V. Novosad, S. Padin, Z. Pan, J. Pearson, C. M. Posada, A. Rahlin, K. Rotermund, J. E. Ruhl, L. J. Saunders, J. T. Sayre, I. Shirley, E. Shirokoff, G. Smecher, J. A. Sobrin, A. A. Stark, K. T. Story, A. Suzuki, Q. Y. Tang, K. L. Thompson, C. Tucker, L. R. Vale, K. Vanderlinde, J. D. Vieira, G. Wang, N. Whitehorn, V. Yefremenko, K. W. Yoon, and M. R. Young, "Design and assembly of spt-3g cold readout hardware," Journal of Low Temperature Physics, vol. 193, pp. 547–555, Nov 2018.

Y. Sekimoto, P. Ade, K. Arnold, J. Aumont, J. Austermann, C. Baccigalupi, A. Ban- day, R. Banerji, S. Basak, S. Beckman, M. Bersanelli, J. Borrill, F. Boulanger, M. L. Brown, M. Bucher,

E. Calabrese, A. Challinor, Y. Chinone, F. Columbro, A. Cukierman, D. Curtis, P. de Bernardis, M. de Petris, M. Dobbs, T. Dotani, L. Duband, A. Ducout, K. Ebisawa, T. Elleflot, H. Eriksen, J. Errard, R. Flauger, C. Franceschet, U. Fuskeland, K. Ganga, J. Gao, T. Ghigna, J. Grain, A. Gruppuso, N. Halverson, P. Hargrave, T. Hasebe, M. Hasegawa, M. Hattori, M. Hazumi, S. Henrot-Versille, C. Hill, Y. Hirota, E. Hivon, D. T. Hoang, J. Hubmayr, K. Ichiki, H. Imada, H. Ishino, G. Jaehnig, H. Kanai, S. Kashima, Y. Kataoka, N. Katayama, T. Kawasaki, R. Keskitalo, A. Kibayashi, T. Kikuchi, K. Kimura, T. Kisner, Y. Kobayashi, N. Kogiso, K. Kohri, E. Komatsu, K. Komatsu, K. Konishi, N. Krachmalnicoff, C. L. Kuo, N. Kurinsky, A. Kushino, L. Lamagna, A. T. Lee, E. Linder, B. Maffei, M. Maki, A. Mangilli, E. Martinez-Gonzalez, S. Masi, T. Matsumura, A. Mennella, Y. Minami, K. Mistuda, D. Molinari, L. Montier, G. Morgante, B. Mot, Y. Murata, A. Mur- phy, M. Nagai, R. Nagata, S. Nakamura, T. Namikawa, P. Natoli, T. Nishibori, H. Nishino, F. Noviello, C. O'Sullivan, H. Ochi, H. Ogawa, H. Ogawa, H. Ohsaki, I. Ohta, N. Okada, G. Patanchon, F. Piacentini, G. Pisano, G. Polenta, D. Poletti, G. Puglisi, C. Raum, S. Re- alini, M. Remazeilles, H. Sakurai, Y. Sakurai, G. Savini, B. Sherwin, K. Shinozaki, M. Shi- raishi, G. Signorelli, G. Smecher, R. Stompor, H. Sugai, S. Sugiyama, A. Suzuki, J. Suzuki, R. Takaku, H. Takakura, S. Takakura, E. Taylor, Y. Terao, K. L. Thompson, B. Thorne, M. Tomasi, H. Tomida, N. Trappe, M. Tristram, M. Tsuji, M. Tsujimoto, S. Uozumi, S. Ut- sunomiya, N. Vittorio, N. Watanabe, I. Wehus, B. Westbrook, B. Winter, R. Yamamoto, N. Y. Yamasaki, M. Yanagisawa, T. Yoshida, J. Yumoto, M. Zannoni, and A. Zonca, "Con- cept design of the LiteBIRD satellite for CMB B-mode polarization," in Space Telescopes and Instrumentation 2018: Optical, Infrared, and Millimeter Wave (M. Lystrup, H. A. MacEwen, G. G. Fazio, N. Batalha, N. Siegler, and E. C. Tong, eds.), vol. 10698, pp. 613 – 629, International Society for Optics and Photonics, SPIE, 2018.

D. Barron, K. Arnold, T. Elleflot, J. Groh, D. Kaneko, N. Katayama, A. Lee, L. Lowry, H. Nishino, A. Suzuki, S. Takatori, P. Ade, Y. Akiba, A. Ali, M. Aguilar, A. Ander- son, P. Ashton, J. Avva, D. Beck, C. Baccigalupi, S. Beckman, A. Bender, F. Bian- chini, D. Boettger, J. Borrill, J. Carron, S. Chapman, Y. Chinone, G. Coppi, K. Crow- ley, A. Cukierman, T. de Haan, M. Dobbs, R. Dunner, J. Errard, G. Fabbian, S. Feeney, C. Feng, G. Fuller, N. Galitzki, A. Gilbert, N. Goeckner-Wald, T. Hamada, N. Halverson, M. Hasegawa, M. Hazumi, C. Hill, W. Holzapfel, L. Howe, Y. Inoue, J. Ito, G. Jaehnig, O. Jeong, B. Keating, R. Keskitalo, T. Kisner, N. Krachmalnicoff, A. Kusaka, M. L. Je- une, D. Leon, E. Linder, A. Lowitz, A. Madurowicz, D. Mak, F. Matsuda, T. Matsumura, A. May, N. Miller, Y. Minami, J. Montgomery, T. Natoli, M. Navroli, J. Peloton, A. Pham, L. Piccirillo, D. Plambeck, D. Poletti, G. Puglisi, C. Raum, G. Rebeiz, C. Reichardt, P. Richards, H. Roberts, C. Ross, K. Rotermund, M. S. Feaver, Y. Segawa, B. Sherwin, P. Siritanasak, L. Steinmetz, R. Stompor, O. Tajima, S. Takakura, D. Tanabe, R. Tat, G. Teply, A. Tikhomirov, T. Tomaru, C. Tsai, C. Verges, B. Westbrook, N. Whitehorn, and A. Zahn, "Electrical characterization and tuning of the integrated POLARBEAR-2a focal plane and readout (Conference Presentation)," in Millimeter, Submillimeter, and Far- Infrared Detectors and Instrumentation for Astronomy IX (J. Zmuidzinas and J.-R. Gao, eds.), vol. 10708, International Society for Optics and Photonics, SPIE, 2018.

M. Hasegawa, T. P. COLLABORATION, P. Ade, M. Aguilar, Y. Akiba, A. Ali, K. Arnold, P. Ashton, C. Baccigalupi, D. Barron, D. Beck, S. Beckman, A. Bender, F. Bianchini, D. Boettger, J.

Borrill, J. Carron, S. Chapman, Y. Chinone, G. Coppi, K. Crowley, A. Cukierman, M. Dobbs, R. Dunner, T. Elleflot, J. Errard, G. Fabbian, S. Feeney, C. Feng, G. Fuller, N. Galitzki, A. Gilbert, N. Goeckner-Wald, J. Groh, T. Haan, N. Halverson, T. Hamada, M. Hazumi, C. Hill, W. Holzapfel, L. Howe, Y. Inoue, J. Ito, G. Jaehnig, A. Jaffe, O. Jeong, M. Jeune, D. Kaneko, N. Katayama, B. Keating, R. Keskitalo, T. Kisner, N. Krachmalnicoff, A. Kusaka, A. Lee, D. Leon, E. Linder, L. Lowry, A. Madurowicz, S. Mak, F. Matsuda, T. Matsumura, A. May, N. Miller, Y. Minami, J. Montgomery, M. Navaroli, H. Nishino, J. Peloton, A. Pham, L. Piccirillo, R. Plambeck, D. Poletti, G. Puglisi, C. Raum, G. Rebeiz, C. Reichardt, P. Richards, H. Roberts, C. Ross, K. R. Rotermund, Y. Segawa, B. Sherwin, M. Silva-Feaver, P. Siritanasak, L. Steinmetz, R. Stompor, A. Suzuki, O. Tajima, S. Takakura, S. Takatori, D. Tanabe, R. Tat, G. Teply, T. Tomaru, C. T. Tsai, C. Verges, B. Westbrook, N. Whitehorn, A. Zahn, J. Suzuki, and T. Okamura, "POLARBEAR-2: a new CMB polarization receiver system for the Simons array (Conference Presentation)," in Millimeter, Submillimeter, and Far-Infrared Detectors and Instrumentation for Astronomy IX (J. Zmuidzinas and J.-R. Gao, eds.), vol. 10708, International Society for Optics and Photonics, SPIE, 2018.

P. A. R. Ade, M. Aguilar, Y. Akiba, K. Arnold, C. Baccigalupi, D. Barron, D. Beck, F. Bianchini, D. Boettger, J. Borrill, S. Chapman, Y. Chinone, K. Crowley, A. Cukierman, R. Dunner, M. Dobbs, A. Ducout, T. Elleflot, J. Errard, G. Fabbian, S. M. Feeney, C. Feng, T. Fujino, N. Galitzki, A. Gilbert, N. Goeckner-Wald, J. C. Groh, G. Hall, N. Halverson, T. Hamada, M. Hasegawa, M. Hazumi, C. A. Hill, L. Howe, Y. Inoue, G. Jaehnig, A. H. Jaffe, O. Jeong, D. Kaneko, N. Katayama, B. Keating, R. Keskitalo, T. Kisner, N. Krachmalnicoff, A. Kusaka, M. L. Jeune, A. T. Lee, E. M. Leitch, D. Leon, E. Linder, L. Lowry, F. Matsuda, T. Matsumura, Y. Minami, J. Montgomery, M. Navaroli, H. Nishino, H. Paar, J. Peloton, A. T. P. Pham, D. Poletti, G. Puglisi, C. L. Reichardt, P. L. Richards, C. Ross, Y. Segawa, B. D. Sherwin, M. Silva-Feaver, P. Siritanasak, N. Stebor, R. Stompor, A. Suzuki, O. Tajima, S. Takakura, S. Takatori, D. Tanabe, G. P. Teply, T. Tomaru, C. Tucker, N. Whitehorn, and A. Zahn, "A measurement of the cosmic microwave BackgroundB-mode polarization power spectrum at subdegree scales from two years of polarbear data," The Astrophysical Journal, vol. 848, p. 121, oct 2017.

P. A. R. Ade, Y. Akiba, A. E. Anthony, K. Arnold, M. Atlas, D. Barron, D. Boettger, J. Borrill, S. Chapman, Y. Chinone, M. Dobbs, T. Elleflot, J. Errard, G. Fab- bian, C. Feng, D. Flanigan, A. Gilbert, W. Grainger, N. W. Halverson, M. Hasegawa, K. Hattori, M. Hazumi, W. L. Holzapfel, Y. Hori, J. Howard, P. Hyland, Y. Inoue, G. C. Jaehnig, A. H. Jaffe, B. Keating, Z. Kermish, R. Keskitalo, T. Kisner, M. L. Jeune, A. T. Lee, E. M. Leitch, E. Linder, M. Lungu, F. Matsuda, T. Matsumura, X. Meng, N. J. Miller, H. Morii, S. Moyerman, M. J. Myers, M. Navaroli, H. Nishino, A. Orlando, H. Paar, J. Pelo- ton, D. Poletti, E. Quealy, G. Rebeiz, C. L. Reichardt, P. L. Richards, C. Ross, I. Schan- ning, D. E. Schenck, B. D. Sherwin, A. Shimizu, C. Shimmin, M. Shimon, P. Siritanasak, G. Smecher, H. Spieler, N. Stebor, B. Steinbach, R. Stompor, A. Suzuki, S. Takakura, T. Tomaru, B. Wilson, A. Yadav, and O. Zahn, "Erratum: "a measurement of the cos- mic microwave background b-mode polarization power spectrum at sub-degree scales with POLARBEAR" (2014, ApJ, 794, 171)," The Astrophysical Journal, vol. 848, p. 73, oct 2017.

S. Takakura, M. Aguilar, Y. Akiba, K. Arnold, C. Baccigalupi, D. Barron, S. Beckman, D. Boettger, J. Borrill, S. Chapman, Y. Chinone, A. Cukierman, A. Ducout, T. Elle- flot, J. Errard,

G. Fabbian, T. Fujino, N. Galitzki, N. Goeckner-Wald, N. W. Halver- son, M. Hasegawa, K. Hattori, M. Hazumi, C. Hill, L. Howe, Y. Inoue, A. H. Jaffe, O. Jeong, D. Kaneko, N. Katayama, B. Keating, R. Keskitalo, T. Kisner, N. Krachmal- nicoff, A. Kusaka, A. T. Lee, D. Leon, L. Lowry, F. Matsuda, T. Matsumura, M. Navaroli, H. Nishino, H. Paar, J. Peloton, D. Poletti, G. Puglisi, C. L. Reichardt, C. Ross, P. Siri- tanasak, A. Suzuki, O. Tajima, S. Takatori, and G. Teply, "Performance of a continuously rotating half-wave plate on the POLARBEAR telescope," Journal of Cosmology and As- troparticle Physics, vol. 2017, pp. 008–008, may 2017.

Poletti, Davide, Fabbian, Giulio, Le Jeune, Maude, Peloton, Julien, Arnold, Kam, Baccigalupi, Carlo, Barron, Darcy, Beckman, Shawn, Borrill, Julian, Chapman, Scott, Chinone, Yuji, Cukierman, Ari, Ducout, Anne, Elleflot, Tucker, Errard, Josquin, Feeney, Stephen, Goeckner-Wald, Neil, Groh, John, Hall, Grantland, Hasegawa, Masaya, Hazumi, Masashi, Hill, Charles, Howe, Logan, Inoue, Yuki, Jaffe, Andrew H., Jeong, Oliver, Katayama, Nobuhiko, Keating, Brian, Keskitalo, Reijo, Kisner, Theodore, Kusaka, Akito, Lee, Adrian T., Leon, David, Linder, Eric, Lowry, Lindsay, Matsuda, Frederick, Navaroli, Martin, Paar, Hans, Puglisi, Giuseppe, Reichardt, Christian L., Ross, Colin, Siritanasak, Praween, Stebor, Nathan, Steinbach, Bryan, Stompor, Radek, Suzuki, Aritoki, Tajima, Osamu, Teply, Grant, and Whitehorn, Nathan, "Making maps of cosmic microwave background polarization for b-mode studies: the polarbear example," A&A, vol. 600, p. A60, 2017.

Y. Inoue, P. Ade, Y. Akiba, C. Aleman, K. Arnold, C. Baccigalupi, B. Barch, D. Barron, A. Bender, D. Boettger, J. Borrill, S. Chapman, Y. Chinone, A. Cukierman, T. de Haan, M. A. Dobbs, A. Ducout, R. Dunner, T. Elleflot, J. Errard, G. Fabbian, S. Feeney, C. Feng, G. Fuller, A. J. Gilbert, N. Goeckner-Wald, J. Groh, G. Hall, N. Halverson, T. Hamada, M. Hasegawa, K. Hattori, M. Hazumi, C. Hill, W. L. Holzapfel, Y. Hori, L. Howe, F. Irie, G. Jaehnig, A. Jaffe, O. Jeong, N. Katayama, J. P. Kaufman, K. Kazemzadeh, B. G. Keating, Z. Kermish, R. Keskitalo, T. S. Kisner, A. Kusaka, M. L. Jeune, A. T. Lee, D. Leon, E. V. Linder, L. Lowry, F. Matsuda, T. Matsumura, N. Miller, K. Mizukami, J. Montgomery, M. Navaroli, H. Nishino, H. Paar, J. Peloton, D. Poletti, G. Puglisi, C. R. Raum, G. M. Rebeiz, C. L. Reichardt, P. L. Richards, C. Ross, K. M. Rotermund, Y. Segawa, B. D. Sherwin, I. Shirley, P. Siritanasak, N. Stebor, R. Stompor, J. Suzuki, A. Suzuki, O. Tajima, S. Takada, S. Takatori, G. P. Teply, A. Tikhomirov, T. Tomaru, N. Whitehorn, A. Zahn, and O. Zahn, "POLARBEAR-2: an instrument for CMB polarization measurements," in Millimeter, Submillimeter, and Far-Infrared Detectors and Instrumentation for Astronomy VIII (W. S. Holland and J. Zmuidzinas, eds.), vol. 9914, pp. 372 – 380, International Society for Optics and Photonics, SPIE, 2016.

T. Matsumura, Y. Akiba, K. Arnold, J. Borrill, R. Chendra, Y. Chinone, A. Cukierman, T. de Haan, M. Dobbs, A. Dominjon, T. Elleflot, J. Errard, T. Fujino, H. Fuke, N. Goeckner- wald, N. Halverson, P. Harvey, M. Hasegawa, K. Hattori, M. Hattori, M. Hazumi, C. Hill, G. Hilton, W. Holzapfel, Y. Hori, J. Hubmayr, K. Ichiki, J. Inatani, M. Inoue, Y. Inoue, F. Irie, K. Irwin, H. Ishino, H. Ishitsuka, O. Jeong, K. Karatsu, S. Kashima, N. Katayama, I. Kawano, B. Keating, A. Kibayashi, Y. Kibe, Y. Kida, K. Kimura, N. Kimura, K. Kohri, E. Komatsu, C. L. Kuo, S. Kuromiya, A. Kusaka, A. Lee, E. Linder, H. Matsuhara, S. Matsuoka, S. Matsuura, S. Mima, K. Mitsuda, K. Mizukami, H. Morii, T. Morishima, M. Nagai, T. Nagasaki, R. Nagata, M. Nakajima,

S. Nakamura, T. Namikawa, M. Naruse, K. Natsume, T. Nishibori, K. Nishijo, H. Nishino, T. Nitta, A. Noda, T. Noguchi, H. Ogawa, S. Oguri, I. S. Ohta, C. Otani, N. Okada, A. Okamoto, A. Okamoto, T. Okamura, G. Rebeiz, P. Richards, S. Sakai, N. Sato, Y. Sato, Y. Segawa, S. Sekiguchi, Y. Sekimoto, M. Sekine, U. Seljak, B. Sherwin, K. Shinozaki, S. Shu, R. Stompor, H. Sugai, H. Sugita, T. Suzuki, A. Suzuki, O. Tajima, S. Takada, S. Takakura, K. Takano, Y. Takei, T. Tomaru, N. Tomita, P. Turin, S. Utsunomiya, Y. Uzawa, T. Wada, H. Watanabe, B. Westbrook, N. Whitehorn, Y. Ya- mada, N. Yamasaki, T. Yamashita, M. Yoshida, T. Yoshida, and Y. Yotsumoto, "Litebird: Mission overview and focal plane layout," Journal of Low Temperature Physics, vol. 184, pp. 824–831, Aug 2016.

A. Suzuki, P. Ade, Y. Akiba, C. Aleman, K. Arnold, C. Baccigalupi, B. Barch, D. Barron, A. Bender, D. Boettger, J. Borrill, S. Chapman, Y. Chinone, A. Cukierman, M. Dobbs, A. Ducout, R. Dunner, T. Elleflot, J. Errard, G. Fabbian, S. Feeney, C. Feng, T. Fujino, G. Fuller, A. Gilbert, N. Goeckner-Wald, J. Groh, T. D. Haan, G. Hall, N. Halverson, T. Hamada, M. Hasegawa, K. Hattori, M. Hazumi, C. Hill, W. Holzapfel, Y. Hori, L. Howe, Y. Inoue, F. Irie, G. Jaehnig, A. Jaffe, O. Jeong, N. Katayama, J. Kaufman, K. Kazemzadeh, B. Keating, Z. Kermish, R. Keskitalo, T. Kisner, A. Kusaka, M. L. Jeune, A. Lee, D. Leon, E. Linder, L. Lowry, F. Matsuda, T. Matsumura, N. Miller, K. Mizukami, J. Montgomery, M. Navaroli, H. Nishino, J. Peloton, D. Poletti, G. Puglisi, G. Rebeiz, C. Raum, C. Re- ichardt, P. Richards, C. Ross, K. Rotermund, Y. Segawa, B. Sherwin, I. Shirley, P. Siri- tanasak, N. Stebor, R. Stompor, J. Suzuki, O. Tajima, S. Takada, S. Takakura, S. Takatori, A. Tikhomirov, T. Tomaru, B. Westbrook, N. Whitehorn, T. Yamashita, A. Zahn, and O. Zahn, "The polarbear-2 and the simons array experiments," Journal of Low Temperature Physics, vol. 184, pp. 805–810, Aug 2016.

H. Ishino, Y. Akiba, K. Arnold, D. Barron, J. Borrill, R. Chendra, Y. Chinone, S. Cho, A. Cukierman, T. de Haan, M. Dobbs, A. Dominjon, T. Dotani, T. Elleflot, J. Errard, T. Fujino, H. Fuke, T. Funaki, N. Goeckner-Wald, N. Halverson, P. Harvey, T. Hasebe, M. Hasegawa, K. Hattori, M. Hattori, M. Hazumi, N. Hidehira, C. Hill, G. Hilton, W. Holzapfel, Y. Hori, J. Hubmayr, K. Ichiki, H. Imada, J. Inatani, M. Inoue, Y. Inoue, F. Irie, K. Irwin, H. Ishitsuka, O. Jeong, H. Kanai, K. Karatsu, S. Kashima, N. Katayama, I. Kawano, T. Kawasaki, B. Keating, S. Kernasovskiy, R. Keskitalo, A. Kibayashi, Y. Kida, N. Kimura, K. Kimura, T. Kisner, K. Kohri, E. Komatsu, K. Komatsu, C.-L. Kuo, S. Kuromiya, A. Kusaka, A. Lee, D. Li, E. Linder, M. Maki, H. Matsuhara, T. Matsumura, S. Matsuoka, S. Matsuura, S. Mima, Y. Minami, K. Mitsuda, M. Nagai, T. Nagasaki, R. Nagata, M. Nakajima, S. Nakamura, T. Namikawa, M. Naruse, T. Nishibori, K. Nishijo, H. Nishino, A. Noda, T. Noguchi, H. Ogawa, W. Ogburn, S. Oguri, I. Ohta, N. Okada, A. Okamoto, T. Okamura, C. Otani, G. Pisano, G. Rebeiz, P. Richards, S. Sakai, Y. Saku- rai, Y. Sato, N. Sato, Y. Segawa, S. Sekiguchi, Y. Sekimoto, M. Sekine, U. Seljak, B. Sherwin, T. Shimizu, K. Shinozaki, S. Shu, R. Stompor, H. Sugai, H. Sugita, J. Suzuki, T. Suzuki, A. Suzuki, O. Tajima, S. Takada, S. Takakura, K. Takano, S. Takatori, Y. Takei, D. Tanabe, T. Tomaru, N. Tomita, P. Turin, S. Uozumi, S. Utsunomiya, Y. Uzawa, T. Wada, H. Watan- abe, B. Westbrook, N. Whitehorn, Y. Yamada, R. Yamamoto, N. Yamasaki, T. Yamashita, T. Yoshida, M. Yoshida, and K. Yotsumoto, "LiteBIRD: lite satellite for the study of B- mode polarization and inflation from cosmic microwave background radiation detection," in Space Telescopes and Instrumentation 2016: Optical, Infrared, and Millimeter Wave (H. A. MacEwen, G. G. Fazio, M. Lystrup, N.

Batalha, N. Siegler, and E. C. Tong, eds.), vol. 9904, pp. 354 – 361, International Society for Optics and Photonics, SPIE, 2016.

N. Stebor, P. Ade, Y. Akiba, C. Aleman, K. Arnold, C. Baccigalupi, B. Barch, D. Barron, S. Beckman, A. Bender, D. Boettger, J. Borrill, S. Chapman, Y. Chinone, A. Cukierman, T. de Haan, M. Dobbs, A. Ducout, R. Dunner, T. Elleflot, J. Errard, G. Fabbian, S. Feeney, C. Feng, T. Fujino, G. Fuller, A. J. Gilbert, N. Goeckner-Wald, J. Groh, G. Hall, N. Halver- son, T. Hamada, M. Hasegawa, K. Hattori, M. Hazumi, C. Hill, W. L. Holzapfel, Y. Hori, L. Howe, Y. Inoue, F. Irie, G. Jaehnig, A. Jaffe, O. Jeong, N. Katayama, J. P. Kaufman, K. Kazemzadeh, B. G. Keating, Z. Kermish, R. Keskitalo, T. Kisner, A. Kusaka, M. L. Jeune, A. T. Lee, D. Leon, E. V. Linder, L. Lowry, F. Matsuda, T. Matsumura, N. Miller, J. Montgomery, M. Navaroli, H. Nishino, H. Paar, J. Peloton, D. Poletti, G. Puglisi, C. R. Raum, G. M. Rebeiz, C. L. Reichardt, P. L. Richards, C. Ross, K. M. Rotermund, Y. Segawa, B. D. Sherwin, I. Shirley, P. Siritanasak, L. Steinmetz, R. Stompor, A. Suzuki, O. Tajima, S. Takada, S. Takatori, G. P. Teply, A. Tikhomirov, T. Tomaru, B. Westbrook, N. White- horn, A. Zahn, and O. Zahn, "The Simons Array CMB polarization experiment," in Mil- limeter, Submillimeter, and Far-Infrared Detectors and Instrumentation for Astronomy VIII (W. S. Holland and J. Zmuidzinas, eds.), vol. 9914, pp. 363 – 371, International Society for Optics and Photonics, SPIE, 2016.

K. Hattori, Y. Akiba, K. Arnold, D. Barron, A. N. Bender, A. Cukierman, T. de Haan, M. Dobbs, T. Elleflot, M. Hasegawa, M. Hazumi, W. Holzapfel, Y. Hori, B. Keating, A. Kusaka, A. Lee, J. Montgomery, K. Rotermund, I. Shirley, A. Suzuki, and N. White- horn, "Development of readout electronics for polarbear-2 cosmic microwave background experiment," Journal of Low Temperature Physics, vol. 184, pp. 512–518, Jul 2016.

P. A. R. Ade, K. Arnold, M. Atlas, C. Baccigalupi, D. Barron, D. Boettger, J. Borrill, S. Chapman, Y. Chinone, A. Cukierman, M. Dobbs, A. Ducout, R. Dunner, T. Elleflot, J. Errard, G. Fabbian, S. Feeney, C. Feng, A. Gilbert, N. Goeckner-Wald, J. Groh, G. Hall, N. W. Halverson, M. Hasegawa, K. Hattori, M. Hazumi, C. Hill, W. L. Holzapfel, Y. Hori, L. Howe, Y. Inoue, G. C. Jaehnig, A. H. Jaffe, O. Jeong, N. Katayama, J. P. Kaufman, B. Keating, Z. Kermish, R. Keskitalo, T. Kisner, A. Kusaka, M. Le Jeune, A. T. Lee, E. M. Leitch, D. Leon, Y. Li, E. Linder, L. Lowry, F. Matsuda, T. Matsumura, N. Miller, J. Mont- gomery, M. J. Myers, M. Navaroli, H. Nishino, T. Okamura, H. Paar, J. Peloton, L. Pogosian, D. Poletti, G. Puglisi, C. Raum, G. Rebeiz, C. L. Reichardt, P. L. Richards, C. Ross, K. M. Rotermund, D. E. Schenck, B. D. Sherwin, M. Shimon, I. Shirley, P. Siritanasak, G. Smecher, N. Stebor, B. Steinbach, A. Suzuki, J.-i. Suzuki, O. Tajima, S. Takakura, A. Tikhomirov, T. Tomaru, N. Whitehorn, B. Wilson, A. Yadav, A. Zahn, and O. Zahn, "Polarbear con- straints on cosmic birefringence and primordial magnetic fields," Phys. Rev. D, vol. 92, p. 123509, Dec 2015.

J. Errard, P. A. R. Ade, Y. Akiba, K. Arnold, M. Atlas, C. Baccigalupi, D. Barron, D. Boettger, J. Borrill, S. Chapman, Y. Chinone, A. Cukierman, J. Delabrouille, M. Dobbs, A. Ducout, T. Elleflot, G. Fabbian, C. Feng, S. Feeney, A. Gilbert, N. Goeckner-Wald, N. W. Halverson, M. Hasegawa, K. Hattori, M. Hazumi, C. Hill, W. L. Holzapfel, Y. Hori, Y. Inoue, G. C. Jaehnig, A. H. Jaffe, O. Jeong, N. Katayama, J. Kaufman, B. Keating, Z. Kermish, R. Keskitalo, T. Kisner,

M. L. Jeune, A. T. Lee, E. M. Leitch, D. Leon, E. Linder, F. Mat- suda, T. Matsumura, N. J. Miller, M. J. Myers, M. Navaroli, H. Nishino, T. Okamura, H. Paar, J. Peloton, D. Poletti, G. Puglisi, G. Rebeiz, C. L. Reichardt, P. L. Richards, C. Ross, K. M. Rotermund, D. E. Schenck, B. D. Sherwin, P. Siritanasak, G. Smecher, N. Stebor, B. Steinbach, R. Stompor, A. Suzuki, O. Tajima, S. Takakura, A. Tikhomirov, T. Tomaru, N. Whitehorn, B. Wilson, A. Yadav, and O. Zahn, "MODELING ATMO- SPHERIC EMISSION FOR CMB GROUND-BASED OBSERVATIONS," The Astrophysi- cal Journal, vol. 809, p. 63, aug 2015.

P. A. R. Ade, Y. Akiba, A. E. Anthony, K. Arnold, M. Atlas, D. Barron, D. Boettger, J. Borrill, S. Chapman, Y. Chinone, M. Dobbs, T. Elleflot, J. Errard, G. Fab- bian, C. Feng, D. Flanigan, A. Gilbert, W. Grainger, N. W. Halverson, M. Hasegawa, K. Hattori, M. Hazumi, W. L. Holzapfel, Y. Hori, J. Howard, P. Hyland, Y. Inoue, G. C. Jaehnig, A. H. Jaffe, B. Keating, Z. Kermish, R. Keskitalo, T. Kisner, M. L. Jeune, A. T. Lee, E. M. Leitch, E. Linder, M. Lungu, F. Matsuda, T. Matsumura, X. Meng, N. J. Miller, H. Morii, S. Moyerman, M. J. Myers, M. Navaroli, H. Nishino, A. Orlando, H. Paar, J. Pelo- ton, D. Poletti, E. Quealy, G. Rebeiz, C. L. Reichardt, P. L. Richards, C. Ross, I. Schan- ning, D. E. Schenck, B. D. Sherwin, A. Shimizu, C. Shimmin, M. Shimon, P. Siritanasak, G. Smecher, H. Spieler, N. Stebor, B. Steinbach, R. Stompor, A. Suzuki, S. Takakura, T. Tomaru, B. Wilson, A. Yadav, and O. Zahn, "A MEASUREMENT OF THE COS- MIC MICROWAVE BACKGROUNDB-MODE POLARIZATION POWER SPECTRUM AT SUB-DEGREE SCALES WITH POLARBEAR," The Astrophysical Journal, vol. 794, p. 171, oct 2014.

A. Suzuki, P. Ade, Y. Akiba, C. Aleman, K. Arnold, M. Atlas, D. Barron, J. Borrill, S. Chapman, Y. Chinone, A. Cukierman, M. Dobbs, T. Elleflot, J. Errard, G. Fabbian, G. Feng, A. Gilbert, W. Grainger, N. Halverson, M. Hasegawa, K. Hattori, M. Hazumi, W. Holzapfel, Y. Hori, Y. Inoue, G. Jaehnig, N. Katayama, B. Keating, Z. Kermish, R. Keskitalo, T. Kisner, A. Lee, F. Matsuda, T. Matsumura, H. Morii, S. Moyerman, M. Myers, M. Navaroli, H. Nishino, T. Okamura, C. Reichart, P. Richards, C. Ross, K. Roter- mund, M. Sholl, P. Siritanasak, G. Smecher, N. Stebor, R. Stompor, J. Suzuki, S. Takada, S. Takakura, T. Tomaru, B. Wilson, H. Yamaguchi, and O. Zahn, "The polarbear-2 experi- ment," Journal of Low Temperature Physics, vol. 176, pp. 719–725, Sep 2014.

K. Arnold, N. Stebor, P. A. R. Ade, Y. Akiba, A. E. Anthony, M. Atlas, D. Barron, A. Ben- der, D. Boettger, J. Borrill, S. Chapman, Y. Chinone, A. Cukierman, M. Dobbs, T. Elle- flot, J. Errard, G. Fabbian, C. Feng, A. Gilbert, N. Goeckner-Wald, N. W. Halverson, M. Hasegawa, K. Hattori, M. Hazumi, W. L. Holzapfel, Y. Hori, Y. Inoue, G. C. Jaehnig, A. H. Jaffe, N. Katayama, B. Keating, Z. Kermish, R. Keskitalo, T. Kisner, M. L. Jeune, A. T. Lee, E. M. Leitch, E. Linder, F. Matsuda, T. Matsumura, X. Meng, N. J. Miller, H. Morii, M. J. Myers, M. Navaroli, H. Nishino, T. Okamura, H. Paar, J. Peloton, D. Po- letti, C. Raum, G. Rebeiz, C. L. Reichardt, P. L. Richards, C. Ross, K. M. Rotermund, D. E. Schenck, B. D. Sherwin, I. Shirley, M. Sholl, P. Siritanasak, G. Smecher, B. Stein- bach, R. Stompor, A. Suzuki, J. Suzuki, S. Takada, S. Takakura, T. Tomaru, B. Wilson, A. Yadav, and O. Zahn, "The Simons Array: expanding POLARBEAR to three multi-chroic telescopes," in Millimeter, Submillimeter, and Far-Infrared Detectors and Instrumentation for

Astronomy VII (W. S. Holland and J. Zmuidzinas, eds.), vol. 9153, pp. 466 – 473, International Society for Optics and Photonics, SPIE, 2014.

Y. Inoue, N. Stebor, P. A. R. Ade, Y. Akiba, K. Arnold, A. E. Anthony, M. Atlas, D. Barron, A. Bender, D. Boettger, J. Borrilll, S. Chapman, Y. Chinone, A. Cukierman, M. Dobbs, T. Elleflot, J. Errard, G. Fabbian, C. Feng, A. Gilbert, N. W. Halverson, M. Hasegawa, K. Hattori, M. Hazumi, W. L. Holzapfel, Y. Hori, G. C. Jaehnig, A. H. Jaffe, N. Katayama, B. Keating, Z. Kermish, R. Keskitalo, T. Kisner, M. L. Jeune, A. T. Lee, E. M. Leitch, E. Lin- der, F. Matsuda, T. Matsumura, X. Meng, H. Morii, M. J. Myers, M. Navaroli, H. Nishino, T. Okamura, H. Paar, J. Peloton, D. Poletti, G. Rebeiz, C. L. Reichardt, P. L. Richards, C. Ross, D. E. Schenck, B. D. Sherwin, P. Siritanasak, G. Smecher, M. Sholl, B. Steinbach, R. Stompor, A. Suzuki, J. Suzuki, S. Takada, S. Takakura, T. Tomaru, B. Wilson, A. Yadav, H. Yamaguchi, and O. Zahn, "Thermal and optical characterization for POLARBEAR-2 op- tical system," in Millimeter, Submillimeter, and Far-Infrared Detectors and Instrumentation for Astronomy VII (W. S. Holland and J. Zmuidzinas, eds.), vol. 9153, pp. 1018 – 1026, In- ternational Society for Optics and Photonics, SPIE, 2014.

D. Barron, P. A. R. Ade, Y. Akiba, C. Aleman, K. Arnold, M. Atlas, A. Bender, J. Bor- rill, S. Chapman, Y. Chinone, A. Cukierman, M. Dobbs, T. Elleflot, J. Errard, G. Fab- bian, G. Feng, A. Gilbert, N. W. Halverson, M. Hasegawa, K. Hattori, M. Hazumi, W. L. Holzapfel, Y. Hori, Y. Inoue, G. C. Jaehnig, N. Katayama, B. Keating, Z. Kermish, R. Keski- talo, T. Kisner, M. L. Jeune, A. T. Lee, F. Matsuda, T. Matsumura, H. Morii, M. J. My- ers, M. Navroli, H. Nishino, T. Okamura, J. Peloton, G. Rebeiz, C. L. Reichardt, P. L. Richards, C. Ross, M. Sholl, P. Siritanasak, G. Smecher, N. Stebor, B. Steinbach, R. Stom- por, A. Suzuki, J. Suzuki, S. Takada, T. Takakura, T. Tomaru, B. Wilson, H. Yamaguchi, and O. Zahn, "Development and characterization of the readout system for POLARBEAR-2," in Millimeter, Submillimeter, and Far-Infrared Detectors and Instrumentation for Astronomy VII (W. S. Holland and J. Zmuidzinas, eds.), vol. 9153, pp. 993 – 1000, International Society for Optics and Photonics, SPIE, 2014.

P. A. R. Ade, Y. Akiba, A. E. Anthony, K. Arnold, M. Atlas, D. Barron, D. Boettger, J. Borrill, S. Chapman, Y. Chinone, M. Dobbs, T. Elleflot, J. Errard, G. Fabbian, C. Feng, D. Flanigan, A. Gilbert, W. Grainger, N. W. Halverson, M. Hasegawa, K. Hat- tori, M. Hazumi, W. L. Holzapfel, Y. Hori, J. Howard, P. Hyland, Y. Inoue, G. C. Jaehnig, A. Jaffe, B. Keating, Z. Kermish, R. Keskitalo, T. Kisner, M. Le Jeune, A. T. Lee, E. Lin- der, E. M. Leitch, M. Lungu, F. Matsuda, T. Matsumura, X. Meng, N. J. Miller, H. Morii, S. Moyerman, M. J. Myers, M. Navaroli, H. Nishino, H. Paar, J. Peloton, E. Quealy, G. Re- beiz, C. L. Reichardt, P. L. Richards, C. Ross, I. Schanning, D. E. Schenck, B. Sherwin, A. Shimizu, C. Shimmin, M. Shimon, P. Siritanasak, G. Smecher, H. Spieler, N. Stebor, B. Steinbach, R. Stompor, A. Suzuki, S. Takakura, T. Tomaru, B. Wilson, A. Yadav, and O. Zahn, "Measurement of the cosmic microwave background polarization lensing power spectrum with the polarbear experiment," Phys. Rev. Lett., vol. 113, p. 021301, Jul 2014.

P. A. R. Ade, Y. Akiba, A. E. Anthony, K. Arnold, M. Atlas, D. Barron, D. Boettger, J. Borrill, C. Borys, S. Chapman, Y. Chinone, M. Dobbs, T. Elleflot, J. Errard, G. Fab- bian, C. Feng, D. Flanigan, A. Gilbert, W. Grainger, N. W. Halverson, M. Hasegawa, K. Hattori, M. Hazumi, W. L. Holzapfel, Y. Hori, J. Howard, P. Hyland, Y. Inoue, G. C. Jaehnig, A. Jaffe, B. Keating, Z.

Kermish, R. Keskitalo, T. Kisner, M. Le Jeune, A. T. Lee, E. M. Leitch, E. Linder, M. Lungu, F. Matsuda, T. Matsumura, X. Meng, N. J. Miller, H. Morii, S. Moyerman, M. J. Myers, M. Navaroli, H. Nishino, H. Paar, J. Peloton, D. Poletti, E. Quealy, G. Rebeiz, C. L. Reichardt, P. L. Richards, C. Ross, K. Rotermund, I. Schan- ning, D. E. Schenck, B. D. Sherwin, A. Shimizu, C. Shimmin, M. Shimon, P. Siritanasak, G. Smecher, H. Spieler, N. Stebor, B. Steinbach, R. Stompor, A. Suzuki, S. Takakura, A. Tikhomirov, T. Tomaru, B. Wilson, A. Yadav, and O. Zahn, "Evidence for gravitational lensing of the cosmic microwave background polarization from cross-correlation with the cosmic infrared background," Phys. Rev. Lett., vol. 112, p. 131302, Apr 2014.

T. Matsumura, P. Ade, Y. Akiba, C. Aleman, K. Arnold, M. Atlas, D. Barron, J. Borrill, S. Chapman, Y. Chinone, A. Cukierman, M. Dobbs, T. Elleflot, J. Errard, G. Fabbian, G. Feng, A. Gilbert, W. Grainger, N. Halverson, M. Hasegawa, K. Hattori, M. Hazumi, W. Holzapfel, Y. Hori, Y. Inoue, G. Jaehnig, N. Katayama, B. Keating, Z. Kermish, R. Keskitalo, T. Kisner, A. Lee, F. Matsuda, H. Morii, S. Moyerman, M. Myers, M. Navaroli, H. Nishino, T. Okamura, C. Reichart, P. Richards, C. Ross, K. Rotermund, M. Sholl, P. Siritanasak, G. Smecher, N. Stebor, R. Stompor, J. ichi Suzuki, A. Suzuki, S. Takada, S. Takakura, T. Tomaru, B. Wilson, H. Yamaguchi, and O. Zahn, Cosmic Microwave Back- ground B-Mode Polarization Experiment POLARBEAR-2.

ABSTRACT OF THE DISSERTATION

Measuring the Polarization of the Cosmic Microwave Background with POLARBEAR-1 and Developing the Next-Generation Experiment POLARBEAR-2

by

Tucker James Elleflot

Doctor of Philosophy in Physics

University of California San Diego, 2019

Professor Brian Keating, Chair

Measurements of the polarization of the Cosmic Microwave Background (CMB) have the potential to provide very strong evidence for cosmic inflation. However, the polarization signal that is expected to have been created by inflation is extremely small. This has motivated the construction of extremely sensitive instruments with thousands of cryogenic detectors.

Simons Array is a CMB polarization experiment comprised of three telescopes located in northern Chile and each containing a cryogenic receiver. The Simons Array will observe in four frequency bands in order to measure the CMB signal as well as polarized foreground signals. The design of the detectors and readout system has been optimized to provide a low noise

measurement and an experiment that can observe in varying weather conditions. Characterizing the detectors and readout system has been a crucial part of the development of the Simons Array receivers.

This dissertation describes the development and deployment of the Simons Array experiment with a focus on characterization of the cryogenic detector and readout electronics.

Chapter 1

Introduction

In this chapter, I lay out our basic understanding of cosmology and how that motivates observations of the Cosmic Microwave Background (CMB).

1.1 The Expanding Universe

Our current model of cosmology is fundamentally based on three assumptions: that General Relativity accurately describes the large scale dynamics of the universe, that the universe is homogeneous and isotropic, and that the energy density of the universe is comprised of four components: non-relativistic matter, radiation, non-relativistic dark matter, and dark energy.

There are three possibilities for the spatial curvature of an isotropic and homogeneous universe: positively curved, flat, and negatively curved. The curvature is determined by the ratio of the total energy density in the universe, ρ, to the critical energy density, ρ_c. This ratio is often labeled Ω. If Ω is greater than, equal to, or less than one, then the geometry of the universe of negatively curved, flat, or positively curved, respectively. The best measurements of the geometry of the universe indicate that the universe is spatially flat and come from a combined analysis of measurements of the CMB temperature and polarization anisotropies, gravitational lensing, and baryon acoustic oscillations [8].

The energy density also governs the dynamics of the universe through Friedmann's equation [9]:

$$H(t)^2 = \frac{8\pi G\rho(t)}{3} - \frac{k^2}{a(t)^2}. \tag{1.1}$$

The scale factor, $a(t)$, represents the size of the universe, k represents spatial curvature and is zero for a flat universe, and $H(t)$ is the Hubble parameter, given by:

$$H(t) = \frac{\dot{a(t)}}{a(t)}. \tag{1.2}$$

The over-dots in Eq. 1.2 represent derivatives with respect to time.

Three components contribute to the energy density of the universe: non-relativistic matter, radiation, and dark energy. Their energy densities are functions of the scale factor. In a spatially flat universe, the energy densities of these three components, respectively, are:

$$\rho_m(t) = \rho_{m,0}\left(\frac{a_0}{a(t)}\right)^3, \tag{1.3}$$

$$\rho_\gamma(t) = \rho_{\gamma,0}\left(\frac{a_0}{a(t)}\right)^4, \tag{1.4}$$

and

$$\rho_\Lambda(t) = \rho_{\Lambda,0}. \tag{1.5}$$

The subscript 0 is used to denote the value of the parameter at present and a_0 is conventionally set to unity without any loss of generality.

The scale factor can increase or decrease with time, corresponding to an expansion or contraction of the universe. For a spatially flat universe dominated by radiation, matter, and dark energy, respectively, the scale factor is given by:

$$a(t) = \left(\frac{t}{t_0}\right)^{2/3} \tag{1.6}$$

$$a(t) = \left(\frac{t}{t_0}\right)^{1/2} \tag{1.7}$$

$$a(t) = e^{H(t-t_0)} \tag{1.8}$$

For small and large enough values of $a(t)$, the total energy density will be dominated by radiation and dark energy, respectively.

Eq. 1.4 implies that the temperature of a photon gas scales inversely with $a(t)$. This effect is known as cosmological redshift and is defined in analog to the Doppler shift as

$$1 + z = \frac{\lambda_{obs}}{\lambda_{emit}}, \tag{1.9}$$

where z is redshift, λ_{obs} and λ_{emit} are the wavelength of the photon when it was observed at the present time and emitted at time t_{emit}, respectively. In a flat universe, a grows monotonically with time and the redshift can be used as a proxy for the lookback time to the emitter.

State-of-the-art measurements of the CMB, distant supernovae, and large scale structure indicate that we live in a universe that is spatially flat with an energy content that is composed of about 4% luminous matter, 27% non-luminous matter, and 69% dark energy [8]. There is also strong evidence of the existence of non-luminous matter and dark energy from measurements of the local universe [10, 11].

Inflation

Inflation is a period of hypothesized accelerated expansion in the very early universe [12]. It has the potential to explain the observed flatness and isotropy of the universe as well as the small over and under densities in the early universe that led to the growth of large scale structures and the temperature and polarization anisotropies in the CMB.

Inflation would have created tensor modes in the spacetime metric of General Relativity (called inflationary gravitational waves). Tensor modes would create a particular pattern in the

temperature and polarization of the CMB. The CMB temperature anisotropies are dominated by the signal from acoustic oscillations except at large angular scales. The polarization signal, however, is not affected by acoustic oscillations, so it is a more sensitive probe of tensor modes than the temperature anisotropies. The ratio of power in tensor modes to power in scalar modes is given by r. The current best constraints on r are $r < 0.06$ and come from the BICEP collaboration using CMB data from the BICEP2/Keck experiments, WMAP, Planck, and other data [13].

1.2 The Cosmic Microwave Background

Photons and matter were held in thermal equilibrium in the early universe through Thomson scattering. This was an efficient coupling mechanism because the universe was very hot and nearly every electron was unbound to an atomic nucleus. As the universe expanded, it cooled to the point that neutral hydrogen could form ($\sim$3700 K), an event that is referred to as recombination. This resulted in a dramatic decrease in the density of free electrons and in the electron-photon scattering rate. The thermal photon gas essentially decoupled from matter at that point in time.

The CMB was first detected by Arno Penzias and Robert Wilson in 1964 when they noticed an isotropic excess antenna temperature in the 20-foot horn reflector antenna at the Crawford Hill Laboratory in Holmdel, New Jersey [14]. It was soon realized that this 3.5 K signal was relic radiation from the early universe [15]. Their discovery began a nearly thirty year campaign to precisely measure the temperature of the CMB, which culminated with the measurement of the CMB blackbody spectrum using the FIRAS instrument on the COBE satellite. The CMB spectrum was determined to be that of a 2.725 ± 0.002 K blackbody [16, 17].

With the results from COBE/FIRAS, we learned that the temperature of the CMB is remarkably constant across sky, with fluctuations on the order of one part in 100,000. At first glance, this result seems highly improbable. Patches of the sky that are separated by more

than about 2 degrees were out of causal contact during recombination, yet the entire CMB sky appears to have been in thermal equilibrium at some point before recombination. However, this contradiction disappears if there was a period of accelerated expansion before recombination, i.e. inflation. Inflation shrinks the comoving Hubble radius, meaning that patches of the sky that were out of causal contact during recombination, could have been in causal contact much earlier.

1.2.1 Temperature Anisotropies

With the first detection of temperature anisotropies [18] and subsequent measurements, the predictions of acoustic waves sourced by slight over and under densities in the early universe were validated [19]. And after two decades of continued pursuit of higher precision measurements, the Planck satellite has mapped the temperature anisotropies of the CMB over the entire sky with the highest precision to date [20], allowing for high precision statistical studies of the CMB and ΛCDM.

Measurements of the CMB temperature are typically decomposed into a basis of spherical harmonics:

$$T(\hat{n}) = \sum_{\ell,m} a_{\ell m} Y_{\ell m} \tag{1.10}$$

Under the assumption of Gaussianity and isotropy, an angular power spectrum of the $a_{\ell m}$ coefficients contains all of the information in the CMB. The power spectrum is defined as:

$$C_\ell = \frac{1}{2\ell+1} \sum_{m=-\ell}^{\ell} a^*_{\ell m} a_{\ell m}. \tag{1.11}$$

Peaks in the angular power spectrum represent modes of the acoustic oscillation that were maximally compressed/expanded during recombination. The physical size of the longest wavelength mode is given by the ratio of the sound speed to the Hubble parameter. The lowest-ℓ peak corresponds to the longest wavelength oscillating mode and its angular size is set by the physical wavelength of the mode and the angular diameter distance to the surface of last scattering.

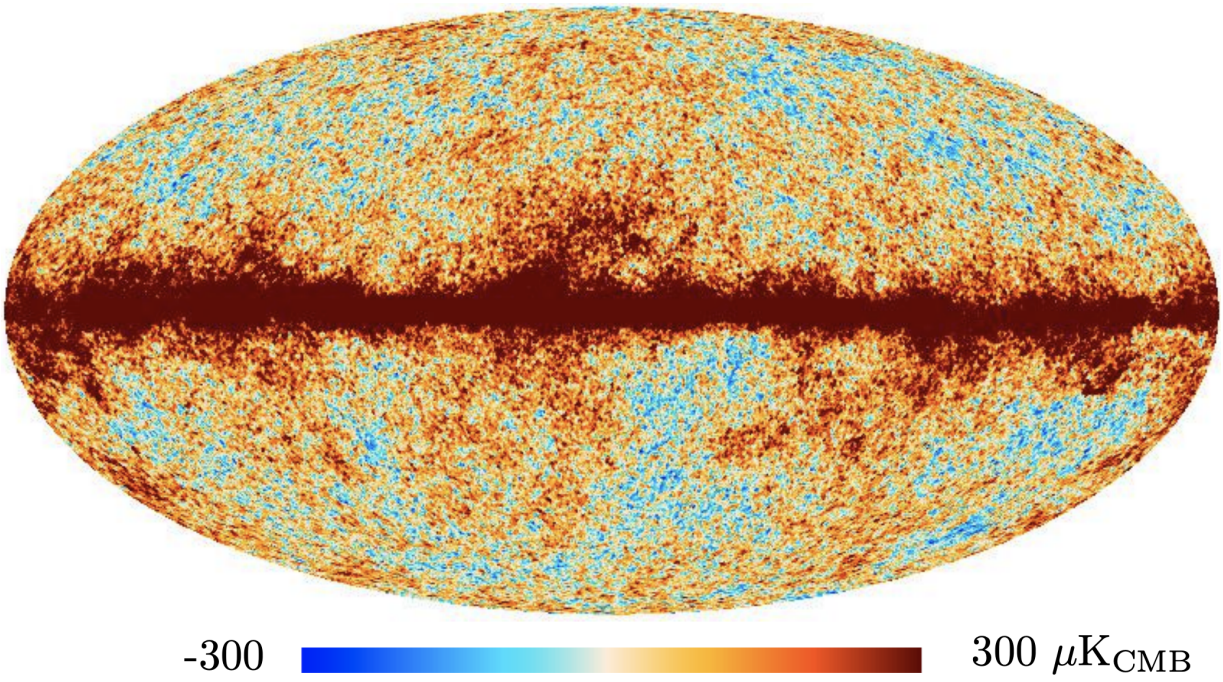

Figure 1.1: Map of temperature anisotropies of the CMB [1]. The plane of the Milky Way is visible as a broad horizontal band through the center of the map.

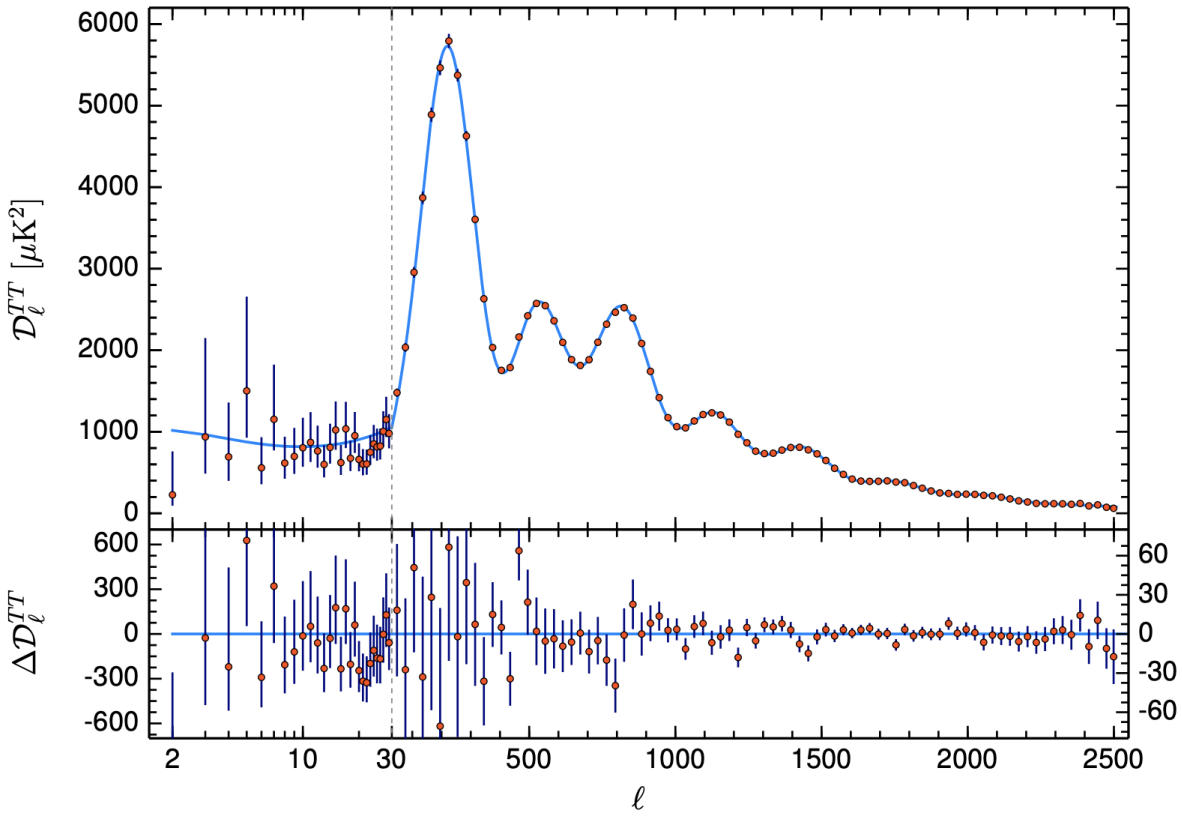

Figure 1.2: CMB temperature anisotropy power spectrum measurements and best-fit cosmological model (*top*) and residuals (*bottom*) from [2]. D_ℓ is related to C_ℓ by $D_\ell = \ell(\ell+1)C_\ell/(2\pi)$. Note the change in horizontal and vertical axes at the dashed line at ℓ=30.

Higher-ℓ peaks are harmonics of the low-ℓ peak. The suppression of power at high ℓ is referred to as Silk damping.

1.2.2 Polarization

The CMB is also very slightly polarized by quadrupolar temperature anisotropies at the surface of last scattering [9]. The polarization field can be decomposed into an orthogonal, coordinate independent basis of parity symmetric E-modes and parity antisymmetric B-modes. Analogously to temperature anisotropies, CMB polarization is commonly characterized by its angular power spectra, C_ℓ^{EE} and C_ℓ^{BB}. E-mode polarization was created by the same phenomenon that

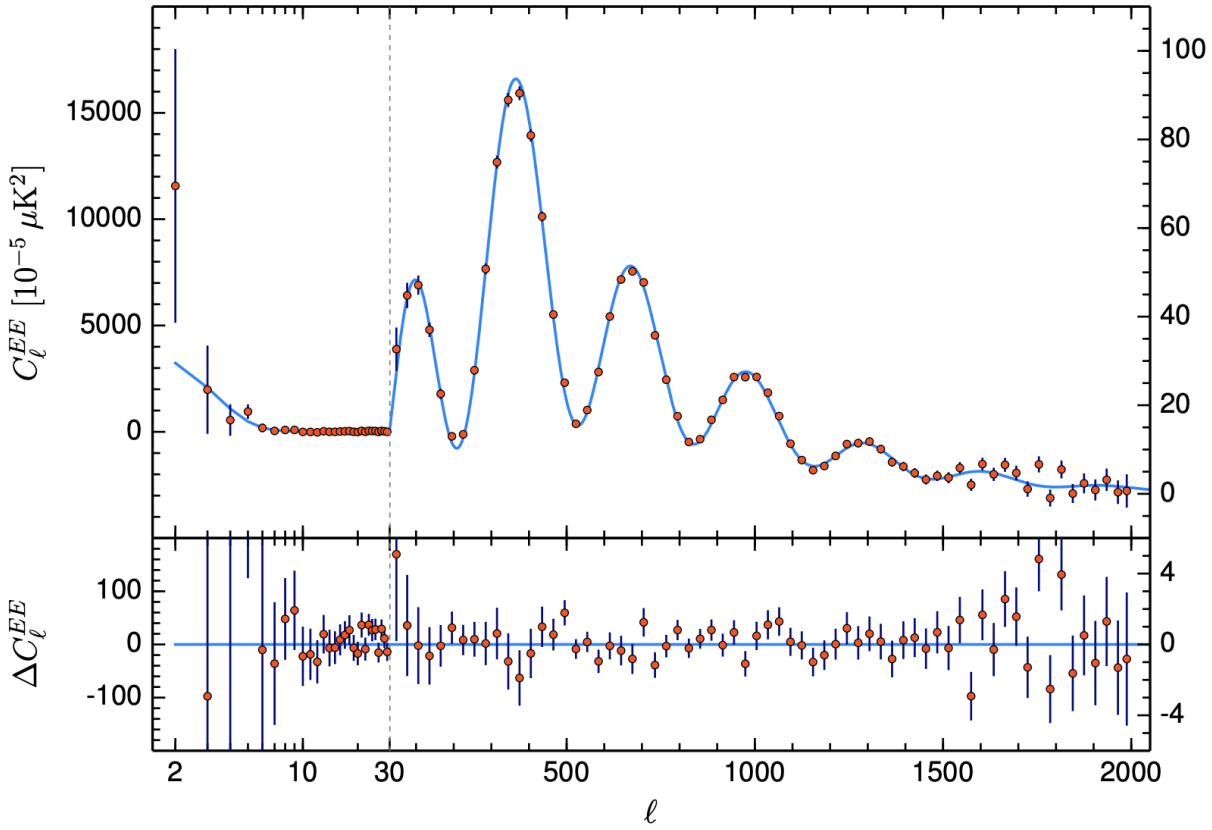

Figure 1.3: CMB E-mode power spectrum measurements and best-fit cosmological model (*top*) and residuals (*bottom*) from [2]. Note the change in horizontal and vertical axes at the dashed line at ℓ=30.

created temperature anisotropies (i.e. acoustic oscillations). B-mode polarization is hypothesized to have been created by gravitational waves from inflation [21].

Additionally, B-mode power exists at small angular scales due to conversion of E-modes to B-modes by gravitational lensing. Gravitational lensing of the CMB provides information about the integrated matter density along the line of sight, which can be used to constrain the neutrino mass [22].

The goal of many modern CMB experiments is to detect the expected low-ℓ B-mode signal from inflationary gravitational waves and to more precisely measure the high-ℓ B-mode signal from gravitational lensing.

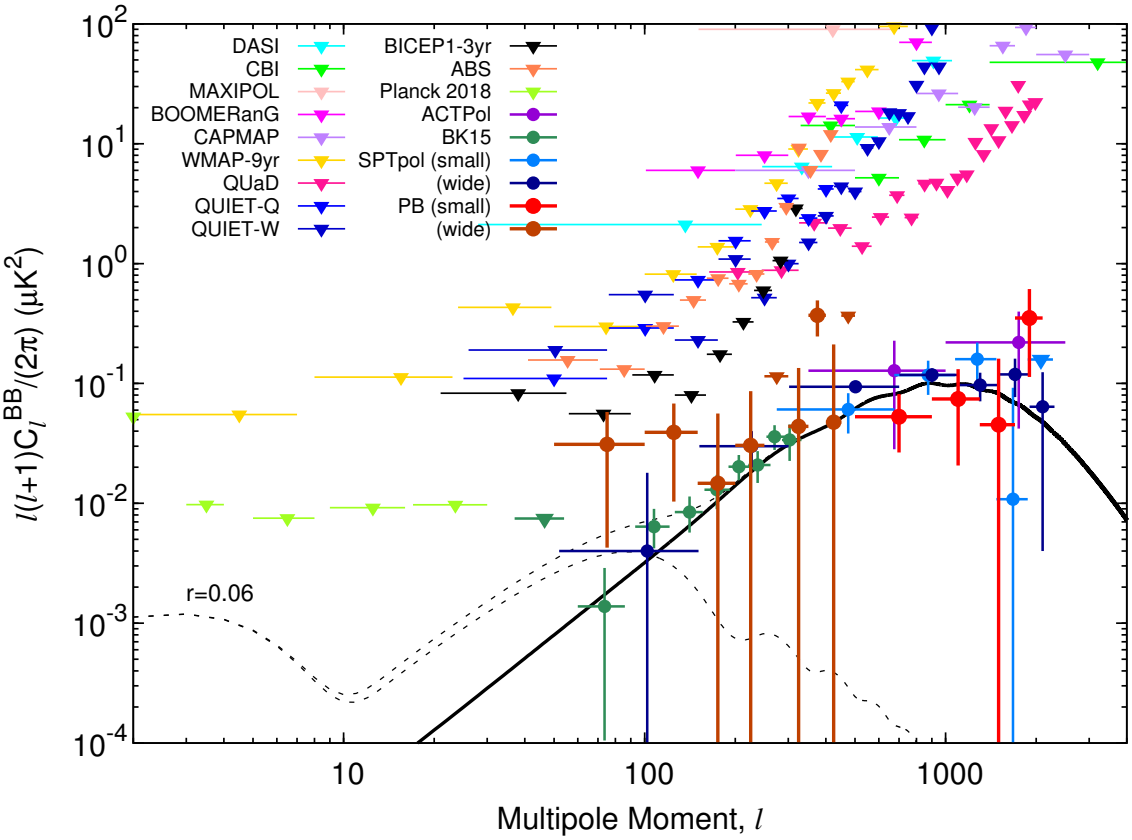

Figure 1.4: Compilation of B-mode measurements from nearly two decades of CMB polarization measurements. Four experiments to date have measured the high-ℓ signal from gravitational lensing. The "PB (wide)" data shown are foreground subtracted for display only. Please see [3] for details of the foreground model. Image credit: Yuji Chinone.

1.2.3 Polarized Galactic Foregrounds

Polarized foregrounds constitute one of the biggest challenges to high-fidelity measurements of the B-mode power spectrum. Because the power in B-modes is so small, even a small polarized foreground signal can dominate the polarization measurement. There are two main sources of polarized foregrounds in our galaxy, both of which are affected by the local alignment of the galactic magnetic field.

Synchrotron emission is created by cosmic electrons that are accelerated in the local magnetic field. Synchrotron has an intensity that declines with frequency with a spectral index of approximately -3. Polarized thermal dust emission is the result of spinning, asymmetric dust grains aligning with the local magnetic field and emitting thermally with a polarization preferentially aligned with their long axes. Polarized thermal dust emission gets stronger at higher frequencies.

Unfortunately, it does not appear to be possible to avoid galactic foregrounds by observing in unaffected patches of sky. This is because the effect is caused by locally aligned magnetic fields, and an empty part of the galaxy likely has a more aligned magnetic field. The path forward for CMB B-mode studies is to better understand the spectral and spatial dependence of the foreground sources and to make judicious choice of frequencies with which to observe the CMB. Current experiments are observing in a wide frequency range, covering nearly an order of magnitude above and below the peak frequency of the CMB, in order to both measure polarized foregrounds and measure the CMB in the bands of lowest contamination.

Chapter 2

POLARBEAR-1 Large Patch

POLARBEAR-1 (PB-1) is a Cosmic Microwave Background (CMB) polarization experiment that observed from northern Chile between 2012 and 2016 [23]. PB-1 has reported measurements of the B-mode power spectrum over the multipole range of ℓ=50-2100 [24, 25, 3] and has provided evidence for gravitational lensing of the CMB including the first measurement of gravitational lensing using CMB data alone [26, 27]. The low ℓ measurements reported in [3] were facilitated by the installation of a continuously rotating ambient-temperature half-wave plate [28]. In this section, I give a description of the PB-1 experiment and the telescope pointing analysis that I performed for [3].

2.1 Instrument Overview

PB-1 observes from the Huan Tran Telescopes (HTT), which is an off-axis Gregorian-Dragone telescope with a 2.5 m primary mirror. This diameter provides $3.5'$ resolution at 150 GHz, allowing PB-1 to probe multipoles up to $\ell \sim 2500$, which is well above the lensing peak at $\ell \sim 1000$. Together with the optics of the receiver, PB-1 has a large diffraction limited field of view of about 2.3 degrees. HTT's lower boom includes two electronics enclosures called saddlebags. These are used to house the ambient-temperature detector readout electronics as well

Figure 2.1: Pictures of HTT at its Chilean observing site taken in 2014 by the author.

as equipment for instrument calibration and monitoring.

Light enters the receiver through a 30 cm thick Zotefoam window. The first optical elements are an IR filter stack and a cryogenic half wave plate. The IR filter stack is used to divert optical power away from the subsequent elements. The cryogenic half wave plate is used to modulate the polarization of the incoming light. Since the atmospheric signal is expected to be predominantly unpolarized, this allows for separation of cosmic polarization from atmospheric intensity. Light is then reimaged by three cryogenic lenses and a set of hemispherical lenslets onto 1,274 Transition Edge Sensor (TES) bolometers each with band-defining, on-chip filters. The TESs convert the optical power to a current signal, which is read out using Superconducting Quantum Interference Devices (SQUIDs) in the Digital Frequency Multiplexing (DfMux) architecture with a multiplexing factor of eight.

The PB-1 receiver is cooled by two refrigerators. The first is a two-stage PTC with temperature stages of 50 K and 4 K. The 50 K stage is used to cool the IR filter stack and the CHWP and as a buffer to the 4 K stage. The 4 K stage cools the reimaging lenses, a cryogenic aperture stop, and the SQUID amplifiers. Cooling the optics of the receiver reduces the total optical power on the detectors, which reduces both the photon noise and the intrinsic detector noise. Cooling the SQUIDs is necessary for their operation and to achieve low readout noise.

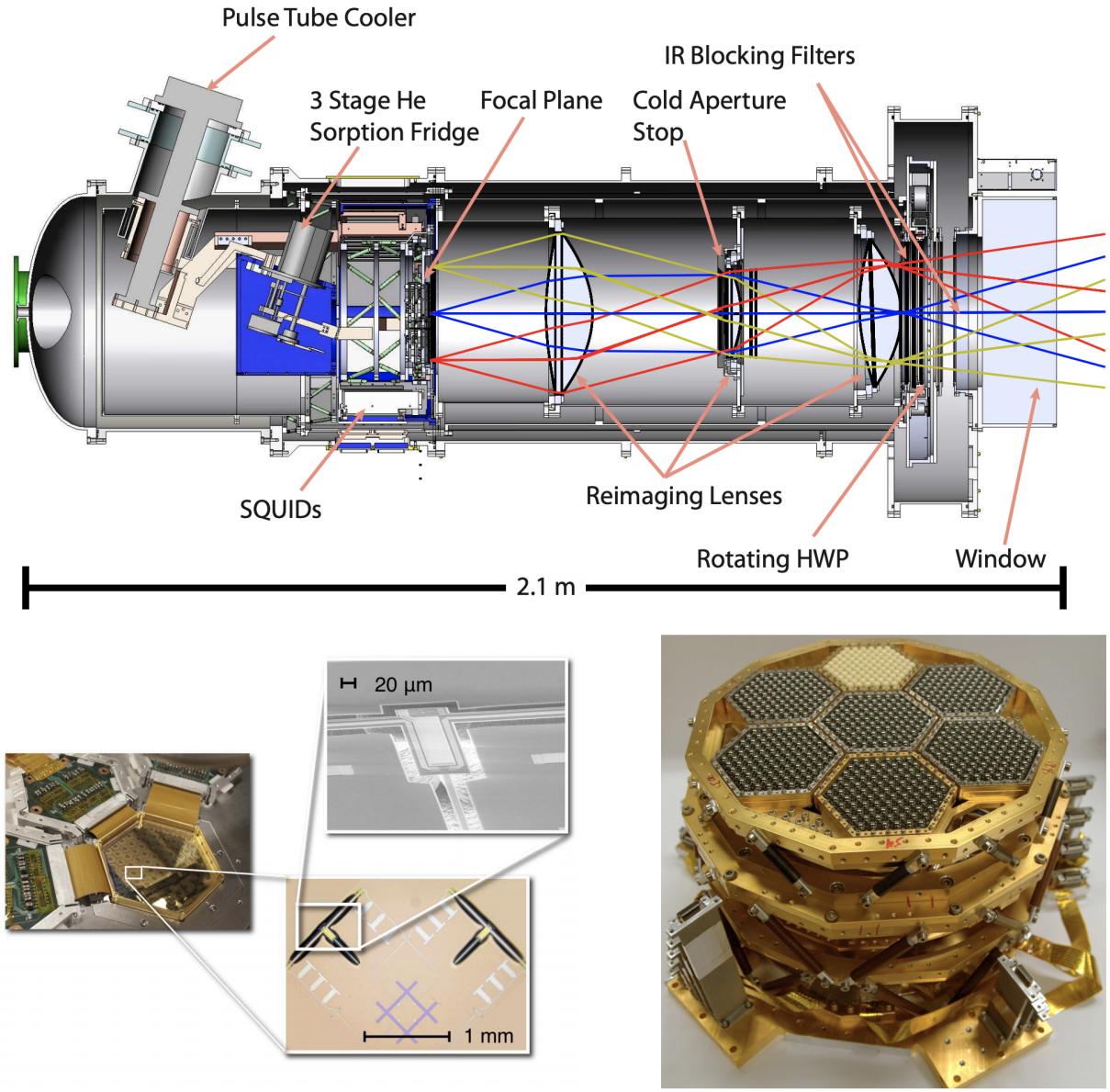

Figure 2.2: A schematic and pictures of the PB-1 receiver. Top: PB-1 receiver cutaway. Light enters the receiver from the right, passes through IR filters, a cold stop, and reimaging lenses before arriving at the 250 mK focal plane. Bottom right: PB-1 focal plane tower, each hexagon is a TES wafer with 182 TES bolometers. Bottom left: A disassembled PB-1 TES wafer with close-up views of the TESs and antennae. All images taken from [23].

The 4 K stage also provides a base for the second refrigerator, a three-stage ^{3}He and ^{4}He adsorption fridge, that is used to cool the detector stage to 250 mK. The dominant detector noise source scales with the square root of this base temperature, so it is important to make it as small as necessary in order to reduce the detector noise below the photon noise.

2.2 Large Patch

In February 2014, an anti-reflection coated, single-crystal sapphire, continuously-rotating half-wave plate (HWP) was installed at the focus of the HTT primary mirror [28]. The half-wave plate was continuously rotated at 2 Hz to reduce the impact of low-frequency noise, allowing for a measurement of the polarized CMB at multipoles down to ℓ=50, below the expected peak of the IGW B-mode signal at $\ell \sim$100.

Observations using the HWP began in July 2014 and continued through December 2016. PB-1 used constant elevation scans (CES) at elevation angles of 30°, 35.2°, and a range between 45.5° and 65.5° to observe a 670 square-degree patch of sky near the south celestial pole. This patch was chosen because of its overlap with South Pole experiments such as BICEP, the Keck Array, and SPT. Each CES lasted approximately four hours and a map of the patch was produced every ten days. Calibration measurements were performed when the patch was not visible, include dedicated observations of astrophysical and terrestrial sources for pointing, beams, gains, polarization angle, and detector time constants. Pointing reconstruction will be covered in detail in Sec. 2.2.1.

The effects of systematics were studied by comparing simulated power spectra with and without the systematic implemented. A signal-only sky map was simulated and scanned to produce simulated TOD. The systematic under study was used to distort the TOD. Then the TOD was made into a map and a power spectrum was produced using the same analysis pipeline as was used for real data. A power spectrum was similarly made from the undistorted TOD

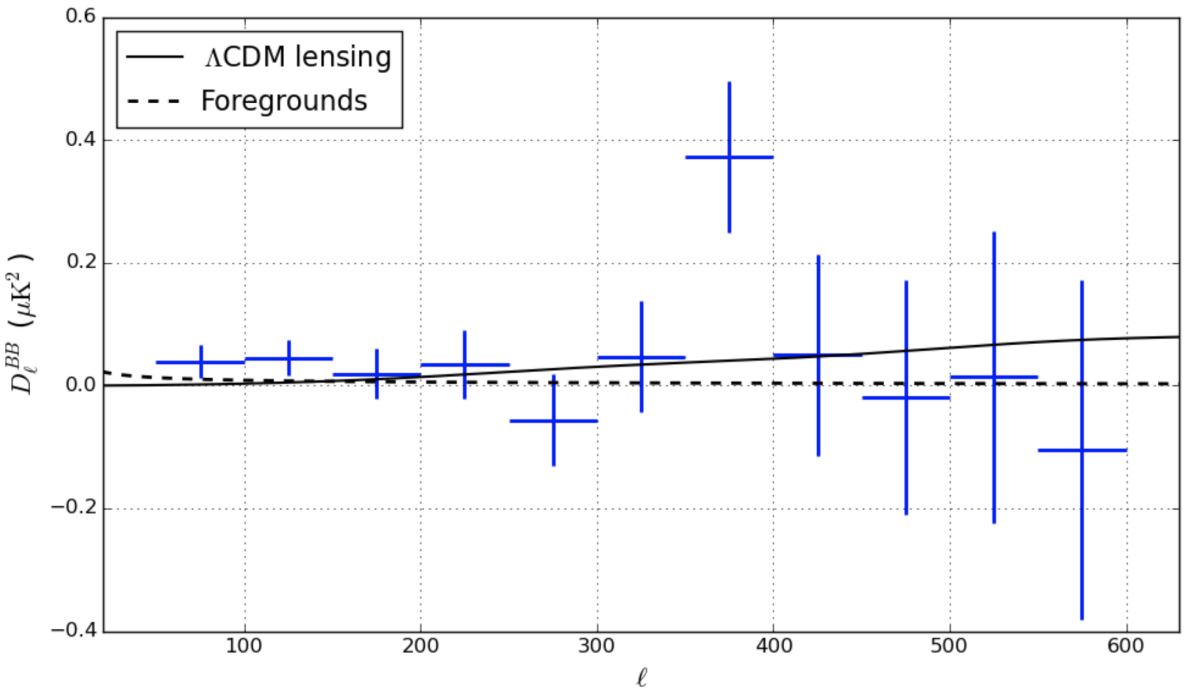

Figure 2.3: The B-mode power spectrum from [3]. The solid and dashed lines are the power from the best-fit cosmological and foreground models, respectively. D_ℓ is related to C_ℓ by $D_\ell = \ell(\ell+1)C_\ell/(2\pi)$.

and the difference of the two power spectra was taken to be the effect of the systematic. The systematics considered are expected to be mostly uncorrelated, but their linear sum was computed when calculating their combined effect on the B-mode power spectrum, therefore this is likely a pessimistic expectation for the effect of systematics in this data set. It was found that the B-mode power spectrum was dominated by statistical noise in all ℓ bins.

These observations produced polarization maps with an effective map depth of 32 μK-arcmin, which are the deepest produced to date using a continuous polarization modulator. The sensitivity of the measurement was not affected by low-frequency drift above ℓ=90. The C_ℓ^{BB} spectrum (Fig 2.3) is consistent with ΛCDM and a single component foreground model and disfavors the $C_\ell^{BB} = 0$ hypothesis at 2.3 σ. Using this data set alone, we place an upper limit on the tensor-to-scalar ratio of $r < 0.9$ at 95% confidence.

2.2.1 Large Patch Pointing Analysis

Telescope pointing refers to the sky position that the telescope is observing in telescope coordinates of azimuth and elevation. Pointing information recorded during CMB observations is used to convert the recorded data into a CMB map. Due to structural imperfections and telescope flexure as well as changes in observing conditions over time, the position reported by the azimuth and elevation encoders of HTT do not match exactly the true telescope pointing. This is a common effect in astronomical observations and the process of measuring and mitigating this effect is known as pointing reconstruction. A random offset between the measured pointing and true pointing degrades the resolution and the high-ℓ sensitivity of the instrument.

Pointing error is parameterized by an azimuth and elevation offset, ΔAz and ΔEl, respectively. We measure the pointing offsets with observations of bright point and extended sources with known, fixed positions in right ascension (RA) and declination (DEC). The known RA and DEC are converted to the expected azimuth and elevation, $Az_{expected}$ and $El_{expected}$, using knowledge of the precise time and location of the observation. The difference between the measured and expected azimuth and elevation positions are the pointing offsets:

$$\Delta Az = Az_{measured} - Az_{expected} \tag{2.1}$$

and

$$\Delta El = El_{measured} - El_{expected}. \tag{2.2}$$

The goal of pointing reconstruction is to use the measured values of ΔAz and ΔEl to determine the true pointing of the telescope. The pointing offsets will, in general, be functions of the azimuth and elevation of the telescope, and may also depend on environmental or other factors. We want to determine both the form of the pointing model and the values of the model parameters. A figure of merit for the success of pointing reconstruction is given by the root-mean-square (RMS) of the pointing offsets after a pointing model has been applied to calculated $Az_{expected}$ and

$El_{expected}$

I performed pointing reconstruction analysis for the PB-1 large patch data set following the analysis in [29]. All analyses use five pointing model terms that are used to model structural imperfections of the telescope. These terms depend on the azimuth and elevation reported by the telescope encoders and are not functions of time. There are two terms to account for an offset in the zero point of the azimuth and elevation encoders (*ia* and *ie*), one term to account for an offset of the optical axis relative to the azimuth encoder (*ca*), and two terms to account for a tilt in the azimuth axis relative to a plane tangential to the surface of the Earth (*an* and *aw*). An additional term to account for small inaccuracies of the GPS clock used to record observation times was also used for all pointing analyses (*dt*).

Significant improvements in pointing reconstruction can be achieved by including terms in the pointing model that model the effects of environmental conditions, such as temperature and insolation [29]. In addition to the six model terms listed, [29] provides six more terms that can be used to account for environmental conditions. These terms are: linear offsets in azimuth and elevation proportional to the measured ambient temperature ($te1$ and $ta1$), offsets due to insolation that depend on the position of the sun relative to the boresight of the telescope (*sa* and *se*), and offsets that depend on the measured solar irradiance at the HTT site and the suns position relative to the boresight (*sai* and *sei*). Generally, these six terms are intended to account for flexure of the telescope structure due to heating from the sun. The *sai* and *sei* terms are intended to account for the same effects as the other four terms, so I do not use all six terms simultaneously.

These pointing models were fit to observations of Jupiter and bright point-like and extended sources that were chosen from [30, 31] based on their expected brightness at 150 GHz and their positions in azimuth and elevation during transit. In order to achieve a good pointing model fit, it is necessary to use many sources that are distributed throughout the azimuth and elevation positions that are used during CMB observations. The azimuth and elevation positions of the pointing observations are shown in Fig. 2.4.

Table 2.1: The pointing model parameters are listed here, along with their effects on the azimuth and elevation pointing offsets. The first set of six parameters accounts for structural imperfections and timing offsets. The next set of four terms accounts for flexure due to temperature gradients and insolation. The last set of two parameters also accounts for flexure due to temperature gradients and insolation, but with fewer terms.

Parameter	Description	ΔAz	ΔEl
ia	Azimuth encoder offset	$\cos(Az)$	0
ie	Elevation encoder offset and collimation error	0	-1
ca	Azimuth collimation error	-1	0
an	Azimuth axis tilt toward north	$\sin(Az)\sin(El)$	$\cos(Az)$
aw	Azimuth axis tilt toward west	$-\cos(Az)\sin(El)$	$\sin(Az)$
dt	Timing error in hour angle direction	$\cos(Az)\cos(lat)\tan(El)$ $-\sin(lat)$	$-\cos(lat)\sin(Az)$
$ta1$	Flexure in elevation due to temperature	T	0
$te1$	Flexure in azimuth due to temperature	0	T
sa	Flexure in elevation from differential insolation	$\sin\theta_s \sin\phi_s$	0
se	Flexure in azimuth from differential insolation	0	$\sin\theta_s \cos\phi_s$
sai	Flexure in azimuth due to solar irradiation	$(I_s/I_{s,0})^{(1/4)} \sin\theta_s \sin\phi_s$	0
sei	Flexure in elevation due to solar irradiation	0	$(I_s/I_{s,0})^{(1/4)} \sin\theta_s \cos\phi_s$

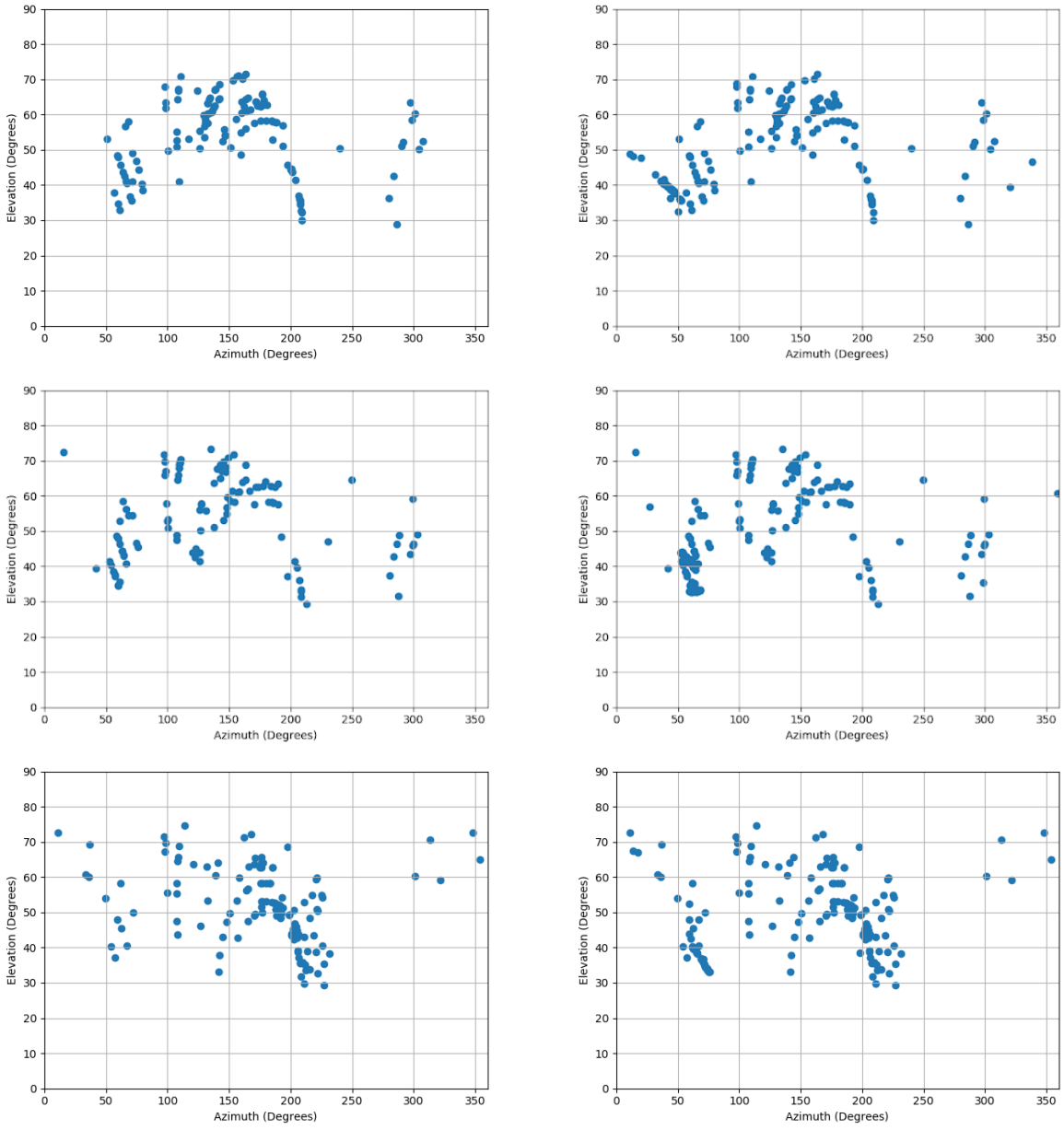

Figure 2.4: Azimuth and elevation positions of the pointing observations used for this analysis. The left column includes only fixed sources and the right column includes fixed sources and Jupiter.

In order to determine which pointing model and set of observations produced the best pointing reconstruction, I performed the pointing model reconstruction three times with different combinations of pointing model terms and source types. The pointing models used are referred to as the ”ten parameter model” and ”eight parameter model.” The ten parameter model uses the five structural imperfection terms (*ia*, *ie*, *ca*, *an*, *aw*), the timing error term (*dt*), and four of the environmental terms ($te1$, $ta1$, *se*, *se*). The eight parameter model uses the same five structural imperfection terms and one timing error term, and the two insolation terms (*sei* and *sai*). The ten parameter model was fit to the fixed sources only and the eight parameter model was fit to fixed sources only and fixed sources and Jupiter. Including Jupiter in the analysis tended to increase the total pointing RMS without improving the azimuth and elevation coverage of the observations dramatically. We decided to use only the dedicated pointing scans for the pointing reconstruction analysis. The ten parameter and eight parameter models produced similar results when fitting the fixed source data, with an overall pointing RMS of about 50”, which was sufficiently small for the ℓ range of this study. The eight parameter model more naturally takes into account the effects of solar heating on the telescope and produces similar results with fewer parameter, so it was chosen as our fiducial pointing model. Further improvements to the pointing model will be required for higher ℓ analysis in order to further reduce the pointing RMS.

2.3 Acknowledgments

Sec. 2.2 is an updated reprint of material as it appears in S. Adachi, M. A. O. A. Faundez, K. Arnold, C. Baccigalupi, D. Barron, D. Beck, S. Beckman, F. Bianchini, D. Boettger, J. Borrill, J. Carron, S. Chapman, K. Cheung, Y. Chinone, K. Crowley, A. Cukierman, M. Dobbs, H. E. Bouhargani, T. Elleflot, J. Errard, G. Fabbian, C. Feng, T. Fujino, N. Galitzki, N. Goeckner-Wald, J. Groh, G. Hall, N. Halverson, T. Hamada, M. Hasegawa, M. Hazumi, C. A. Hill, L. Howe, Y. Inoue, G. Jaehnig, O. Jeong, D. Kaneko, N. Katayama, B. Keating, R. Keskitalo, S. Kikuchi, T.

Kisner, N. Krachmalnicoff, A. Kusaka, A. T. Lee, D. Leon, E. Linder, L. N. Lowry, A. Mangu, F. Matsuda, Y. Minami, M. Navaroli, H. Nishino, A. T. P. Pham, D. Poletti, G. Puglisi, C. L. Reichardt, Y. Segawa, M. Silva-Feaver, P. Siritanasak, N. Stebor, R. Stompor, A. Suzuki, O. Tajima, S. Takakura, S. Takatori, D. Tanabe, G. P. Teply, C. Tsai, C. Verges, B. Westbrook, and Y. Zhou, "A measurement of the degree scale cmb b-mode angular power spectrum with polarbear," 2019. Submitted to The Astrophysical Journal. The dissertation author made essential contributions to this work.

Chapter 3

The Simons Array

The Simons Array is an expansion of POLARBEAR-1 (PB-1) to three telescopes. Each telescope will contain an individual cryogenic receiver called POLARBEAR-2a (PB-2a), POLARBEAR-2b (PB-2b), and POLARBEAR-2c (PB-2c) with a six-fold increase in detector count and a five-fold increase in multiplexing factor compared to PB-1, a continuously-rotating half-wave plate, a dedicated Pulse Tube Cryocooler (PTC) for the receiver optics, and increased frequency coverage, with observing bands centered at 90, 250, 220, and 270 GHz. SA has two primary science goals: to detect the low-ℓ B-mode signal from inflationary gravitational waves and to measure the high-ℓ B-mode signal from gravitational lensing of the E-mode polarization of the Cosmic Microwave Background (CMB).

3.1 Observing Site

The high altitude and arid climate of the Atacama Desert make it one of the premier locations for astronomical observations in millimeter and sub-millimeter wavelengths. As such, it is the home of several ongoing CMB experiments, namely POLARBEAR/SA, CLASS, ACT, as well as the site for the future Simons Observatory and a candidate site for CMB-S4. Being a tropical-latitude site, the Atacama Desert has access to about 80% of the sky and benefits from

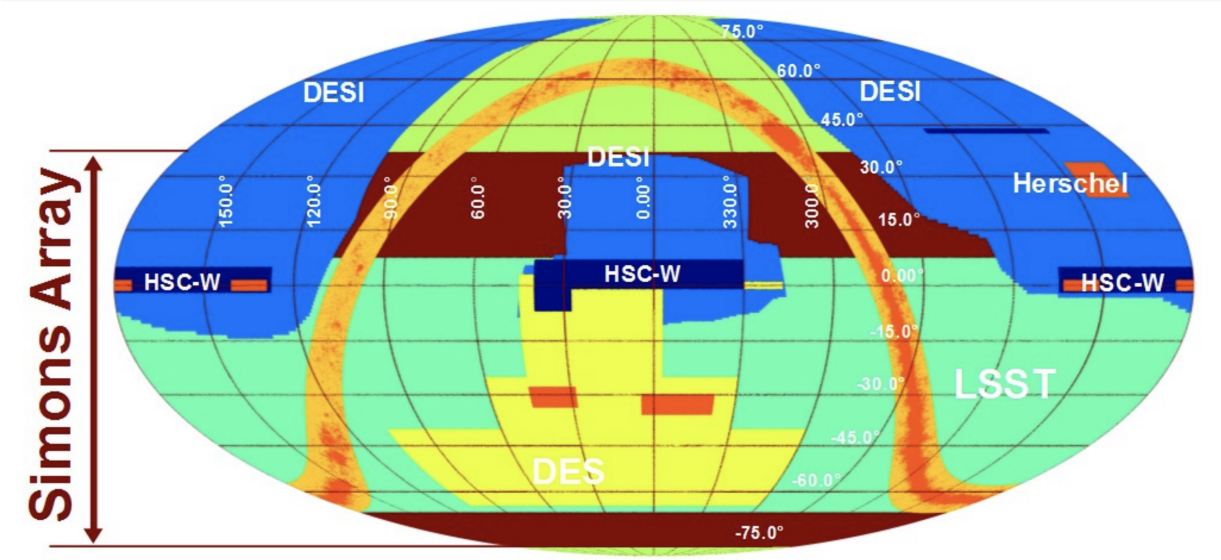

Figure 3.1: Map of sky with portion accessible from the SA observing site labeled [4]. SA will have access to 80% of the sky and overlap with many other astrophysical surveys.

polarization modulation on day time-scales due to sky rotation.

3.2 Telescopes

The SA telescopes include the original PB-1 Huan Tran Telescope (HTT), along with two additional telescopes that were based on the HTT design. These telescopes are off-axis Gregorian Dragone designs with 2.5 m primary mirrors that produce a resolution of 3.5' at 150 GHz. The telescopes have comoving ground shields that reduce ground pickup. Along with the optics of the receivers, this provides a diffraction-limited field of view of 2.3 degrees at 150 GHz.

Although the new SA telescopes were based on the HTT design, there were some changes made to the mechanical structure in order to allow for improved baffling, space for additional counterweights for the elevation axis since the SA receivers are much heavier than PB-1, and a larger receiver enclosure and two additional saddlebags.

The saddlebags are temperature-controlled, weather-sealed electronics enclosures that

mount to the lower boom of the telescope. They are used to hold all of the on-telescope ambient-temperature electronics, including electronics used for detector biasing and readout, receiver thermometry, telescope thermometry, and calibration. The saddlebags also have electronics racks that are made from insulating polycarbonate to make it easier to control how things are grounded. The detector bias and readout electronics are very sensitive to their grounding configuration as well as the ambient air temperature, so both of these things are very important for good readout noise performance.

The two new SA telescopes were fabricated in 2015 by General Dynamics. A test assembly at the fabrication facility in northern Italy was performed in order to establish an assembly procedure and to ensure that the telescopes were fabricated to the correct specifications. We installed the primary and secondary mirrors, counterweights, a dummy weight to mimic the torque of the receiver, the comoving ground shield, and the saddlebags. Pictures of the test assembly at the fabrication facility are shown in Fig. 3.2.

The telescopes were shipped to Chile and assembled on-site in March-April of 2016. Pictures from the on-site assembly are shown in Fig. 3.3.

3.3 Cryogenic Receivers

Each telescope contains a cryogenic receiver whose purpose is to provide a cryogenic environment for the detectors and optics of the instrument. It is necessary to cool these components below ambient temperature in order to measure the extremely small polarized signal of the CMB. This section provides an overview of the design of the POLARBEAR-2 cryogenic receivers. For more information, see [32, 33, 5, 6].

Figure 3.2: Pictures from the factory acceptance testing of the new SA telescopes in 2015. *Top right:* telescope structure before installation of the primary or secondary mirrors. A dummy weight is installed at the end of the lower boom in order to simulate the torque from the weight of the receiver. The unpainted steel structure on the telescope is the backing structure for the comoving ground shield. *Top left:* Test installation of the primary mirror. *Bottom left:* Test installation of the saddlebags. *Bottom right:* The fully assembled comoving ground shield. The elevation cable wrap has also been installed. The telescope is pointing toward zenith.

Figure 3.3: Pictures of SA telescope assembly in April 2016. *Top:* The author installing the azimuth cable wrap in an SA telescope. *Bottom left:* An SA telescope before installation of the primary mirror. *Bottom right:* An SA telescope after installation of the primary mirror.

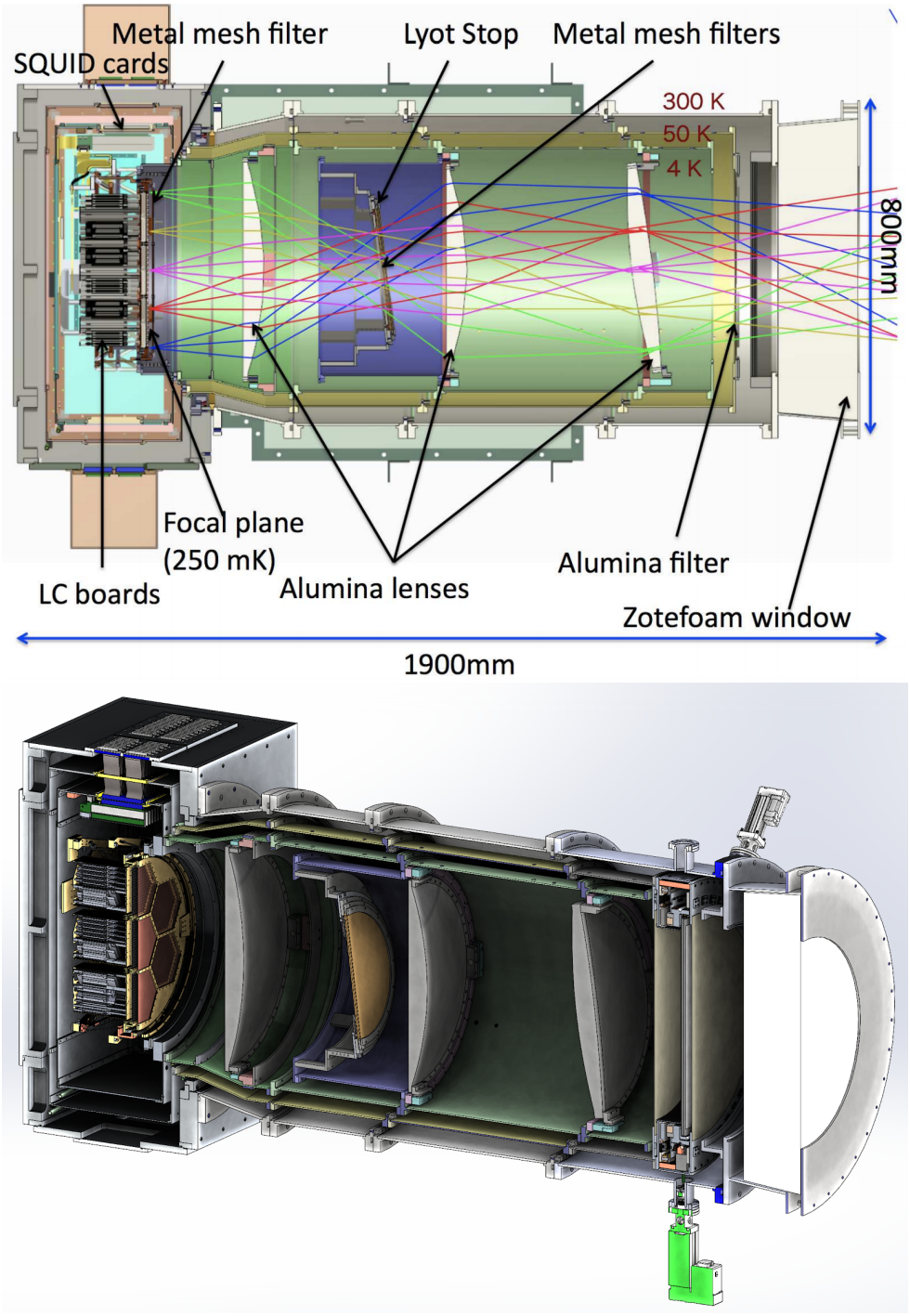

Figure 3.4: Receiver cutaways of PB-2a (top) and PB-2b/c (bottom). The primary difference is that the PB-2b/c receivers have a cryogenic half wave plate inside the receiver. Images from [5, 6]

3.3.1 Cryogenics

Each receiver uses a pair of PTCs to reach internal temperatures of approximately 50 K and 4 K. The 50 K stage is used to cool filters and a cryogenic half wave plate in PB-2b and PB-2c and as a buffer for the 4 K stage. The 4 K stage is used to cool the base of the detector stage, the Superconducting Quantum Interference Device (SQUID) amplifiers, and optical elements. One of the PTCs in each receiver is dedicated to cooling the optics tube and the other is used to cool the backend.

In addition to the PTCs, the receivers each contain a sub-kelvin refrigeration system constituted of ^{4}He and ^{3}He adsorption refrigerators. Each of the three receivers has a slightly different sub-kelvin cooler design, but they all provide a base temperature of approximately 0.3 K to the detector stage. Loading on the detector stage and buffer sub-kelvin stages determines the base temperature and hold time of the sub-kelvin refrigerators.

3.3.2 Optics

The optics of the receiver are designed in order to minimize in-band reflections, scattering and optical loading on the detectors.

The first optical element is an ambient temperature window holds the vacuum of the receiver. The next optical elements are an alumina filter and RT-MLI at the 50 K stage. PB-2b and PB-2c also have a continuously-rotating cryogenic half-wave plate (HWP) that is radiatively cooled by the 50 K stage. The three reimaging lenses, the Lyot stop, and a metal mesh low-pass filter are cooled by the 4 K stage. Finally, there is a low-pass MMF cooled by the sub-Kelvin refrigerator.

The optics are cooled to cryogenic temperatures in order to reduce their contribution to the optical power incident on the detectors. The photon noise from a single element in the optical

chain is given by [34, 35, 36]

$$NEP_\gamma = \sqrt{2\int_0^\infty \left[h\nu p(\nu) + p(\nu)^2\right] B(\nu) d\nu}, \tag{3.1}$$

where $p(\nu)$ is the power spectral density of the optical element referred to the detector input and $B(\nu)$ is the bandpass of the detector. The power radiated by the optical element can be considered a blackbody with emissivity less than one, so NEP_γ is a strong power of temperature. A lower optical power also means that a lower detector saturation power can be used. The detector's thermal carrier noise is proportional to the square root of the saturation power, so a decrease in optical power corresponds to a decrease in thermal carrier noise.

The half-wave plate is used to modulate the linear polarization of incoming radiation. One of the most significant sources of low-frequency drift in the incoming power signal is due to changes in atmospheric conditions and weather. The polarized sky signal, will be modulated at four times the rotation frequency of the HWP, which moves it away from the slow drift of the unpolarized atmospheric signal.

3.3.3 Detectors

Each SA receiver contains over 7,500 Transition Edeg Sensor (TES) bolometers, six times as many detectors as PB-1. TES bolometers are very sensitive optical sensors that are routinely operated such that the dominant noise source is the photon noise of the incoming radiation. The bolometers are optimized for observations in the 90, 150, 220, and 270 GHz band by modifying their saturation power to accommodate the expected optical power in those observing bands.

The bolometers are fabricated on 150 mm silicon wafers at University of California Berkeley's Marvel Nanofabrication Laboratory. Each wafer has 271 dichroic pixels and each pixel contains four optical bolometers for observing both linear polarizations in two frequency bands. The observing bands are defined on-wafer with band-defining filters. The TESs are

coupled to a sinuous antenna with a niobium microstrip. The sinuous antenna is a broadband, polarization sensitive antenna. The beam of the antenna is collimated by a directly-contacting hemispherical silicon lenslet [37, 38].

3.3.4 Readout

Optimized TES bolometers operate at the photon-noise limit. The only way to increase the sensitivity of an array of single-moded detectors operating at the photon-noise limit is to increase the number of detectors. This motivated an increase in detector count by a factor of 6. In order to achieve this increase in detector-count while maintaining reasonable cryogenic wiring complexity, an increase in multiplexing factor was required. PB-2 has a multiplexing factor of 40, five times higher than that of PB-1. Increasing the multiplexing factor was achieved by using a larger readout bandwidth, low-loss lithographed LC resonators, superconducting niobium-titanium broadside-coupled striplines, and low input inductance SQUIDs [39, 40, 41, 42, 43, 44].

Chapter 4

Simons Array Detectors and Readout

4.1 Transition Edge Sensor Bolometers

Cosmic Microwave Background (CMB) imaging experiments have historically used either semiconducting or superconducting bolometers as their detectors. Bolometers are capable of operating with low enough noise that the measurement noise is dominated by the photon noise of the incoming optical signal rather than the detector itself [34]. This has driven CMB experiments to increase detector counts by orders of magnitude in order to increase their total experimental sensitivity.

Both bolometer types operate on the principle that the detector's resistance varies with temperature. When the optical power on the detector changes, a change in its resistance changes the electrical signal measured. The advantage of superconducting bolometers over semiconducting bolometers is that they are well-suited to a voltage bias, rather than a current bias, and that they have a much stronger dependence of resistance on temperature. This gives them the ability to be operated at high loop gain, increasing uniformity across arrays of detectors and making them very well-suited to multiplexing [45]. Superconducting bolometers are now used by almost every modern CMB experiment. They are commonly fabricated on 100-150 mm silicon wafers with

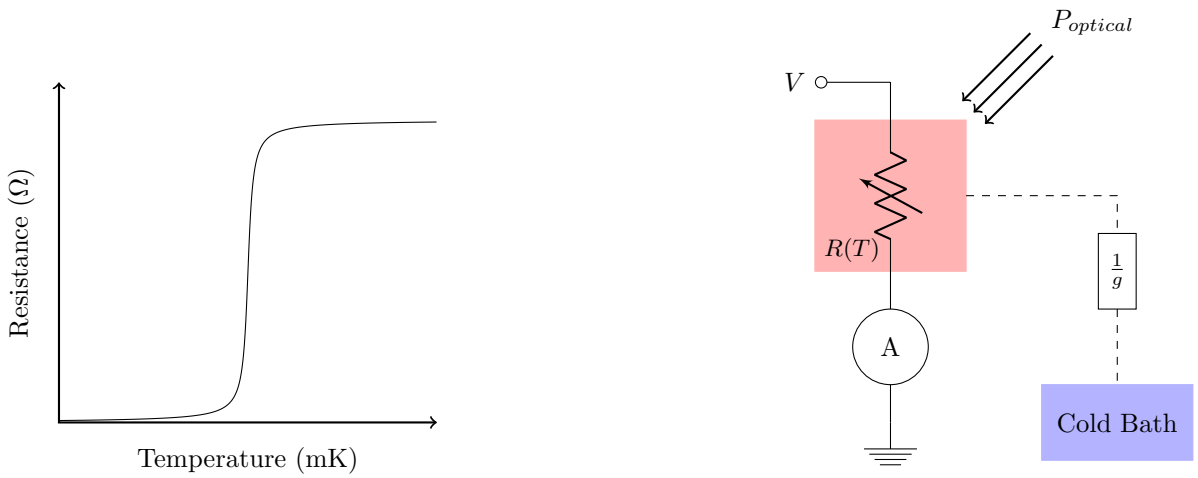

Figure 4.1: *Left*: A simulated superconducting transition is shown. *Right*: A TES is operated under voltage bias and thermally connected to a cold bath.

1,000-2,000 detectors on a single wafer. This allows for more uniform detector properties, more efficient fabrication, and very close packing of detectors.

A schematic of a superconducting bolometer, commonly referred to as a Transition Edge Sensor (TES), is shown in Fig. 4.1. A typical TES consists of a thin film of a superconducting material that is weakly thermally coupled to a cold bath. The TES is operated by applying a voltage bias to heat it to its superconducting transition temperature. In this state, a small change of the TES temperature causes a large change in its resistance and the current driven through it. In this way, the TES transduces temperature fluctuations into current fluctuations. In order to make the TES an optical power sensor, it must be coupled to an optical signal. This is commonly done by putting a load resistor coupled to an antenna in thermal contact with the TES. Optical signals are absorbed in the antenna and dissipated on the load resistor, heating the TES and modulating the bias current.

4.1.1 Definition of TES Parameters

In order to simplify notation later, I will use this subsection to define a number of important TES parameters. The parameters are summarized in Table 4.1.

The TES resistance is R. Without subscript, R refers to the operating resistance of the TES. R_n is the normal resistance of the TES. R_{frac} is the fractional resistance of the TES relative to its normal resistance, i.e. $R_{frac} \equiv R/R_n$.

Variables that change in time will be written as a sum of a steady state term, denoted with a subscript 0, and a time-varying term, denoted with a prefix δ. For example, the steady-state and time-varying parts of the TES resistance will be written as R_0 and δR, respectively. The TES resistance R is the sum of R_0 and δR.

The critical temperature of the TES is labeled T_c, the cold bath temperature is T_b and the TES operating temperature is T. The TES operates in its superconducting transition, so $T \approx T_c$, but T can vary slightly away from T_c during operations with finite loop gain. The heat capacity of the TES is C, its thermal energy is E. The thermal conductance of the legs that connect the TES to the thermal bath, g, is given by the integral of the temperature-dependent thermal conductivity of the legs, k, between T_b and T_c. The differential thermal conductance, dP_{bath}/dT, is labeled G.

The incident power terms associated with a TES are: P_{elec}, the Joule power; P_{opt}, optical power coupled through the load resistor; and P_{bath}, the power flowing from the bath to the TES ($P_{bath} < 0$ because $T > T_b$). The TES saturation power, P_{sat} is that amount of power that is required to drive the TES above its superconducting transition temperature, given by $P_{sat} = g(T_c - T_b)$. The turnaround power, P_{turn}, is used as a proxy for P_{sat} during TES characterization and is defined as the Joule power on the TES when the slope of the IV curve is zero (more on IV curves in later parts). P_{turn} is typically about 10% larger than P_{sat} for PB-2a and PB-2b detectors.

The TES power-to-current responsivity (hereafter referred to as simply "responsivity"), S_I is given by $S_I \equiv dI/dP_{opt}$. The TES time constant in the absence of electrothermal feedback is called the natural time constant, denoted by τ_0, and given by $\tau_0 = C/G$. The electrothermal

feedback enhanced TES time constant is given by τ. In the text, "time constant" will always refer to τ and "natural time constant" to τ_0. Electrothermal feedback is parameterized by the TES loop gain, $\mathcal{L}$, defined as $\mathcal{L} \equiv \alpha P_{elec,0}/GT_0$

4.1.2 Small Signal Response

TESs under voltage bias benefit from a phenomenon known as electrothermal feedback (ETF). ETF stabilizes the TES in its superconducting transition, linearizes the detector's response, and decreases its response time. We can see this with some simple analysis based on conservation of energy.

Energy flows into the TES from Joule heating, optical power, and the cold bath (negative power flow because $T_{bath} < T_c$). Conservation of energy requires that the sum of these three terms equal the change in the TES energy. This is written as:

$$P_{opt} + P_{elec} + P_{bath} = \frac{dE}{dt}. \tag{4.1}$$

Performing a Taylor series expansion, subtracting off steady-state terms, and moving to the Fourier domain leaves us with the small-signal power balance equation:

$$\delta P_{opt} - \frac{P_{elec,0}}{R_0}\delta R = (i\omega C + G)\delta T. \tag{4.2}$$

To see that ETF stabilizes the TES, let's look at how the electrical power changes in response to a change in optical power. To do so, I'll substitute the two expressions below into Eq. 4.2:

$$\alpha = \frac{T_0}{R_0}\frac{\delta R}{\delta T} \tag{4.3}$$

and

$$\delta R = \frac{-R}{P_{elec,0}}\delta P_{elec}. \tag{4.4}$$

Table 4.1: Table of TES parameters

Category	Description	Symbol	Definition
Resistance	Operating resistance	R	
	Normal resistance	R_n	
Temperature	TES temperature	T	
	Critical temperature	T_c	
	Bath temperature	T_{bath}	
Power	Saturation power	P_{sat}	
	Joule power	P_{elec}	
	Optical power	P_{opt}	
	Power flowing to TES from bath	P_{bath}	
	Power at turnaround of IV curve	P_{turn}	
Thermal conductance	Thermal conductivity of legs	k	$k_0 T^n$
	Thermal conductivity coefficient	k_0	
	Thermal conductivity index	n	
	Average thermal conductance	g	$P_{sat}/(T_c - T_{bath})$
Small-signal	Logarithmic slope of transition	α	$(T_0/R_0)(\frac{dR}{dT})\|_{T=T_0}$
	Differential heat capacity	C	dE/dT
	Differential thermal conductance	G	dP_{bath}/dT
	Power-to-current responsivity	S_I	dI/dP_{opt}
	Natural time constant	τ_0	C/G
	Electrothermal feedback enhanced time constant	τ	
	Loop gain	$\mathcal{L}$	$(\alpha P_{elec})/(GT)$

Eq. 4.3 is the first order term of the Taylor series expansion of $R = R(T)$ and Eq. 4.4 is the first order term of the Taylor series expansion of $P_{elec} = \frac{V^2}{R}$. After these substitutions, we get this relation

$$\delta P_{elec} = -\delta P_{opt} \frac{\mathcal{L}}{\mathcal{L} + 1 + i\omega\tau_0}. \tag{4.5}$$

In the limit of high loop gain, a change in optical power is exactly compensated by a change in electrical power to keep the total incident power on the TES constant.

To look at TES linearity, we want to know the change in current caused by the change in optical power. To do this, I'll start with Eq. 4.2 and make two substitutions. The first substitution is Eq. 4.3 and the second is

$$\frac{\delta R}{R_0} = -\frac{\delta I}{I_0}, \tag{4.6}$$

which is the first order term of the Taylor series expansion of Ohm's law. Doing so leads the the TES responsivity, given by

$$S_I \equiv \frac{\delta I}{\delta P_{opt}} = -\frac{1}{V} \frac{\mathcal{L}}{\mathcal{L} + 1 + i\omega\tau_0} \tag{4.7}$$

At high loop gain, S_I is a constant and the TES response is linear. The responsivity has the form of a single pole low-pass filter with a time constant given by

$$\tau = \frac{\tau_0}{\mathcal{L} + 1}. \tag{4.8}$$

As the loop gain increases, the TES response time decreases.

An additional benefit of high loop gain is that it makes it easier to operate a large array of TES bolometers. At high loop gain, the TES responsivity asymptotically approaches

$$S_I = \frac{-1}{V}. \tag{4.9}$$

An array of TES bolometers acts uniformly, with their response depending only on the voltage

bias applied to them and not on the characteristics of the individual TESs.

4.1.3 TES Noise

TESs are subject to four noise terms known as thermal carrier noise, Johnson noise, photon noise, and readout noise. The first two are fundamental to the detector and the latter two are due to things external to the detector.

TES noise is often described by its a noise equivalent power (NEP) on the TES. NEP is defined as the signal power required in a half-second of integration time to achieve a signal-to-noise ratio of 1. It is also common to refer TES noise to the temperature of the CMB sky in units of noise equivalent temperature (NET). The relation between NET and NEP is given by

$$NET = \frac{1}{\sqrt{2}} \frac{NEP}{dP/dT}. \tag{4.10}$$

The denominator in Eq. 4.10 tells you how much the optical power on the TES changes with a small change in the CMB temperature and is dependent on the efficiency of the telescope and receiver optics.

Thermal carrier noise is caused by the random thermal motions of thermal carriers transmitting power between the TES and the thermal bath. Its noise equivalent power is given by [34]:

$$NEP_g = \sqrt{4k_b P_{sat} T_{bath}} \sqrt{\frac{(n+1)^2}{2n+3} \frac{T_c}{T_b} \frac{1-(T_b/T_c)^{2n+3}}{(1-(T_b/T_c)^{n+1})^2}}. \tag{4.11}$$

The optimal choice of T_c/T_b given a particular n will result in the the second term on the right hand side of Eq. 4.11 being minimized to of order 1.

Johnson noise is created by the random thermal motion of electrons in the TES electrical circuit. The noise equivalent power in Johnson noise is given by

$$NEP_{Johnson} = \frac{\mathcal{L}+1}{\mathcal{L}^2} \sqrt{4k_b T_c P_{elec}}. \tag{4.12}$$

Since $P_{elec} \sim P_{sat}$ and the second term in $NEP_g \sim 1$, Johnson noise is suppressed relative to thermal carrier noise by a factor of $(\mathcal{L}+1)/\mathcal{L}^2$. At high loop gain, Johnson noise becomes subdominant to thermal carrier noise and isn't an important contribution to TES noise.

Photon noise is the result of the random arrival rate of photons. It is generated by every emissive element in the beam of the detectors. This includes the optical elements of the telescope and receiver as well as the atmosphere and the CMB. For ground based telescopes, even in the best observing sites in the world, the optical loading has a significant contribution from the atmosphere. For a narrow band detector with integrated bandwidth $\Delta\nu$ and band center ν_0 with optical power P_{opt}, the photon NEP is approximated by [34, 35]

$$NEP_\gamma = \sqrt{2}\sqrt{h\nu_0 P_{opt} + \frac{P_{opt}^2}{\Delta\nu}}. \tag{4.13}$$

The term proportional to $\sqrt{P_{opt}}$ is due to Poisson statistics and the term proportional to P_{opt} is due to photon bunching. At the observing frequencies relevant for CMB observations, both terms are important.

Readout noise is associated with biasing and measuring the TES. It is not directly caused by the TES but is unavoidable if you want to know the signal from the TES. We will discuss readout noise in more detail for the Simons Array (SA) readout system 4.2.6. Readout noise is often quoted as a current noise referred to the Superconducting Quantum Interference Device (SQUID) input coil, $NEI_{readout}$. To compare this to the other TES noise terms, we need to refer it to power at the TES using the TES responsivity. Doing so yields

$$NEP_{readout} = \frac{1}{|S_I|} NEI_{readout}. \tag{4.14}$$

The TES responsivity suppresses readout noise so that at high responsivity, the readout noise is negligible.

Arraying many TES detectors can result in a decrease in NEP relative to a single detector. The NEP for an array of N detectors with equal uncorrelated white noise, $NEP_{detector}$ is given by:

$$NEP_{array} = \frac{NEP_{detector}}{\sqrt{N}}. \tag{4.15}$$

In practice the noise will be somewhat correlated between detectors, so 4.15 represents the best possible reduction in noise for an array of detectors.

4.2 Digital Frequency-Division Multiplexing

Multiplexing is an important technology for modern CMB experiments. It allows for the operation of many TES bolometers without the overwhelming cost and wiring complexity that would come with individual bolometer readout chains. Multiplexing also allows for reduced thermal loading on the detector cryogenic stage, which relaxes constraints on the cryogenic design of other parts of the experiment, and reduced power consumption, which is particularly important for space-based applications where power is extremely limited.

4.2.1 Principle of Operation

PB-2 uses Digital Frequency Multiplexing (DfMux) to bias and read out sets of forty detector channels with a single set of readout electronics and a single cryogenic cable between the 4 K SQUID array and 250 mK detector stage (Fig. 4.2). Each detector is placed in series with a resonant LC filter and biased with an alternating voltage of a unique frequency. Optical signals modulate the resistance of the TESs and the resulting amplitude modulation of the bias current is measured by a SQUID. The output voltage of the SQUID is digitized and demodulated to recover the signals from each readout channel. An integral control loop injects a nulling signal into the SQUID to linearize it and reduce its input impedance. Hereafter, one set of multiplexed detectors

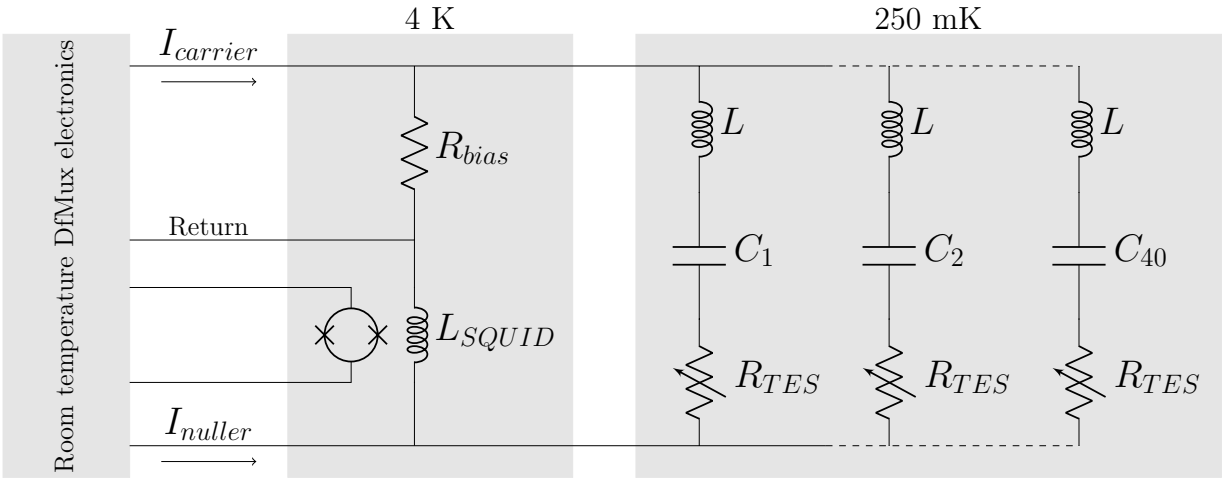

Figure 4.2: A schematic of the DfMux cryogenic circuit is shown. Each TES is placed in series with a resonant LC filter and the parallel configuration of many TESs is biased with an AC voltage. The resonant frequencies are in the range of 1.5-4.5 MHz. The current created by the voltage bias is modulated by optical signals and the current signal is measured by a SQUID.

will be referred to as a comb.

Some important parameters to optimize in the cryogenic DfMux circuit are the values of the detector normal resistances, inductances, and capacitances as well as the bias resistance and the SQUID input inductance.

The TES normal resistance is set by requiring that the readout can deliver a stiff voltage bias. The bias resistor and stray impedances act as a voltage divider with the TES. Typical values of the stray impedance are 0.15-0.5 Ω for PB-2a and 0.15-.3 Ω for PB-2b and PB-2c. We have chosen a TES resistance of 1 Ω and a bias resistance of 30 mΩ.

The inductance of the the resonators is set by a TES stability requirement. The electrical time constant of an RLC resonator is given by the inverse of the half width at half maximum of the resonance:

$$\tau_{elec} = \frac{2L}{R}. \tag{4.16}$$

In order to achieve stable TES operation, the TES time constant, τ, must be at least 5.8 times

larger than the electrical time constant [46]:

$$\tau \geq 5.8\tau_{elec}. \tag{4.17}$$

We use a single value of $L = 60\ \mu$H for each resonator so that τ_{elec} will be approximately constant for every resonator, with variations caused by variations in R from detector to detector. This results in an electrical time constant of 0.15 ms for a TES operating at 0.8 Ω, allowing for a minimum detector time constant of 0.9 ms.

To manipulate the resonant frequencies, we change the capacitance value of each resonator [42]. The maximum capacitance (lowest resonant frequency) is set by constraints on the physical size of the LC chip. Frequency spacing is chosen to keep crosstalk low and constant across an entire multiplexed set of detectors (more on crosstalk in Sec. 4.2.3). The frequency schedule chosen is logarithmic in the frequency range of 1.6-4.5 MHz, corresponding to capacitances in the range of 20-155 pF.

The SQUID input coil inductance is a source of readout noise amplification [44]. In order to minimize this, we chose a low-inductance SQUID.

The current signals are summed and inductively coupled to a Superconducting Quantum Interference Device (SQUID) amplifier. SQUIDs are extremely sensitive devices for measuring current signals, but they are also highly nonlinear and they present a large input impedance to the TES. To solve both of these problems, a nulling current is supplied to the SQUID input coil. The nulling current is chosen to be perfectly out of phase with the bias current of each detector, resulting in zero bias current going through the input coil. This effectively zeroes the input impedance of the SQUID and dramatically increases its dynamic range.

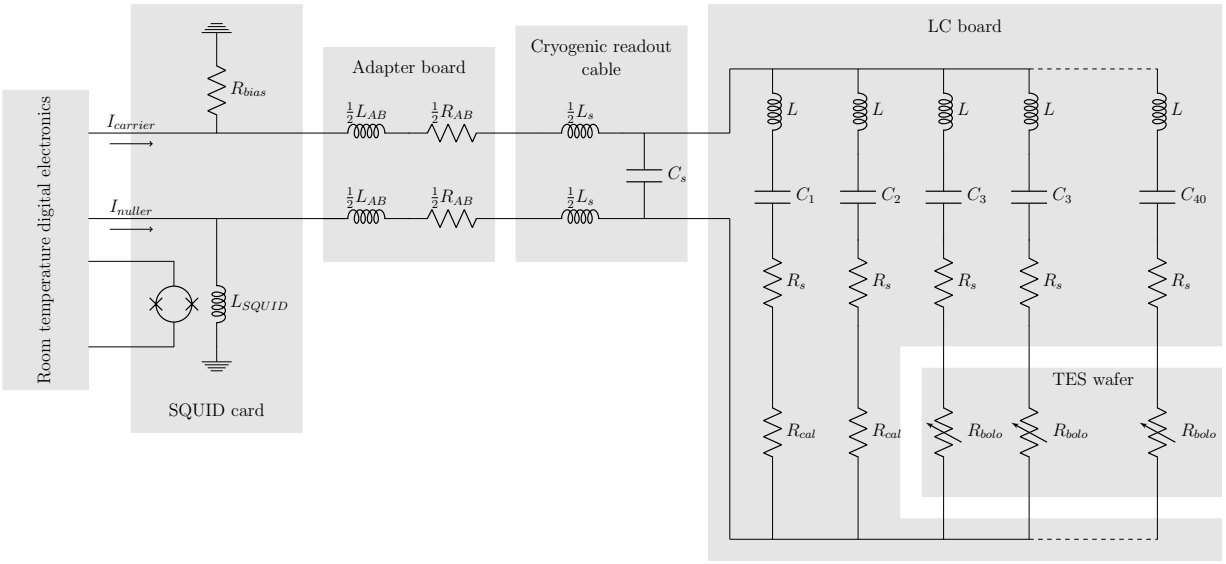

Figure 4.3: The DfMux cryogenic circuit has a number of known sources of stray impedances, shown here. The stray impedances are (from left to right): a bias inductance, L_{bias}; an inductance between the bias element and the LC board and, separately, an inductance between the SQUID and the LC board, each contributing, $\frac{1}{2}L_s$; a resistance between the bias element and the LC board and, separately, a resistance between the SQUID and the LC board, each contributing, $\frac{1}{2}R_s$; a stripline capacitance, C_s; a resistance in each leg of the comb, $R_{s,i}$ for the i-th leg.

4.2.2 Stray Impedance

DfMux has stray impedances in the cryogenic circuit that have important effects of the performance of this multiplexing technology. Stray impedances are created by wiring inductance and capacitance, dielectric loss in capacitors, and contact resistance of connectors [47, 40, 41, 42, 43] (see Fig. 4.3 for a non-exhaustive schematic of stray impedances). Stray impedance contributes to crosstalk [47], affects TES performance, and obcures TES parameters [48].

4.2.3 Crosstalk

There are three primary mechanisms for crosstalk in the DfMux architecture: inductor cross-coupling, bias carrier current leakage, and voltage division caused by stray impedance [47].

Inductor cross-coupling refers to the coupling of the inductors in two LC resonators. A current driven through inductor i will create a voltage across inductor j, which will drive a current through TES j. When the current of TES i is modulated by a sky signal, the cross-coupling current will also be modulated in TES j. This effect is suppressed by the off-resonance impedance of channel j and the physical distance between resonators i and j. This is a subdominant crosstalk mechanism in DfMux systems due to careful layout of the resonator chips that put neighboring frequency resonances far from each other physically.

Current leakage refers to the the bias voltage from channel i driving a current through the $i \pm 1$ resonators due to their finite off-resonance impedance. This current is modulated by optical signals in the $i \pm 1$-th TES, but is attributed to the i-th TES when the signal is demodulated. The ratio of the leakage current signal to the on-resonance current signal is given by:

$$\left| \frac{R^2}{(2\Delta\omega L)^2} \right|. \tag{4.18}$$

Stray inductance in the wiring between the bias element and the comb and the squid and the comb can also create crosstalk by forming a voltage divider with the TESs. The bias voltage at resonant frequency ω_i is set by a voltage divider between the stray impedance and the TES. When the TES resistance changes, the voltage bias changes slightly, which drives slightly more or less current leakage through channels $i \pm 1$. This causes Joule heating in channels $i \pm 1$, modulating the current at frequency $\omega_{i\pm1}$. The ratio of the power in channel i to the power in channel $i \pm 1$ is given by:

$$\frac{dP_i}{dP_{i\pm1}} \approx \frac{I_{i\pm1}}{I_i} \frac{\omega_i}{\Delta\omega} \frac{L_s}{L} \tag{4.19}$$

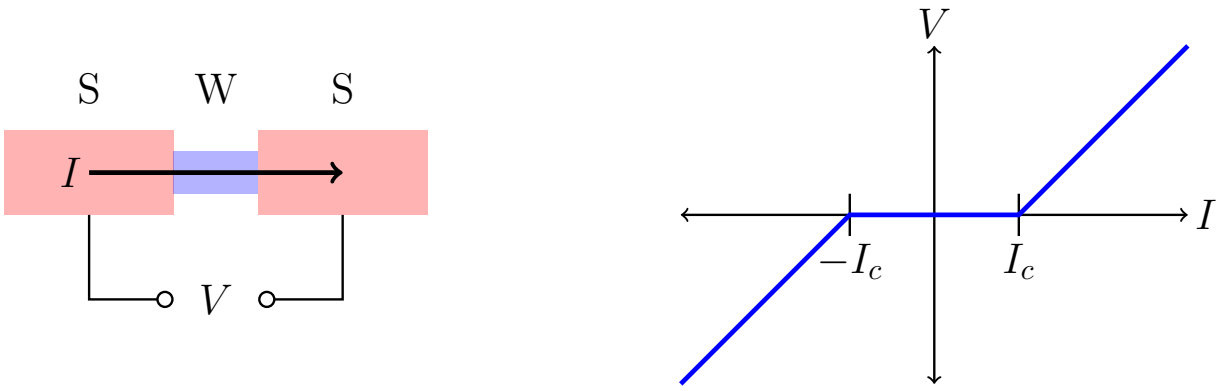

Figure 4.4: Schematic of a Josephson junction and its current-voltage relation. *Left:* Josephson junction, in which two superconducting leads labeled "S" are separated by a weak link labeled "W." A current, I, is flowing through the junction. *Right*: The voltage across the junction is plotted as a function of the I. Below I_c, current flows across the junction with zero resistance. Above I_c, a voltage develops, indicating that the junction has a resistance.

4.2.4 Cryogenic Components

DC SQUIDs

In order to measure the very small fluctuations in current generated by sky signals on the TES, we need a low noise, low input impedance ammeter. For this purpose, we use a DC SQUID array (hereafter SQUID) coupled inductively to the TES current. SQUIDs are one of the most sensitive magnetometers available [49] and, when inductively coupled to TES currents, provide excellent amplification of small current signals. SQUIDs rely on two quantum mechanical phenomena to transduce small changes in magnetic field to measurable voltage signals: the Josephson effect and the quantization of flux in a superconducting loop.

The Josephson effect describes the flow of current across an junction (either a normal metal or an insulator) in a superconducting material. At temperatures below the critical temperature of the superconductor, a supercurrent can flow across the junction up to a maximum value of current called the critical current. Beyond I_c, a voltage develops across the junction. This is shown schematically in Fig. 4.4. These junctions are called Josephson junctions and the phenomenon is called the Josephson effect.

The second phenomenon is that the magnetic flux through a superconducting loop is quantized in units of $\phi_0 = h/2e$, referred to as a flux quantum. ϕ_0 does not depend on material properties and is a constant of nature. The total flux through a superconducting loop is given by the sum of any external flux applied and the flux created by the screening current flowing around the loop, ϕ_{screen}:

$$\phi_{total} = \phi_{external} + \phi_{screen} \tag{4.20}$$

Flux quantization requires that $\phi_{total} = n\phi_0$ where n is any integer. Therefore, if an external magnetic flux is applied to the superconducting loop, a screening current will develop to satisfy Eq. 4.20.

Combining these two effects into a single device leaves us with the DC SQUID, shown inductively coupled to a current in its input coil, I_{in}, in Fig. 4.5. To put the SQUID into a responsive state, the Josephson junctions must be driven beyond their critical current. This is done by applying a bias current, I_{bias}, such that $I_{bias} > 2I_c$. Any additional current flow due to ϕ_{screen} will induce a change of voltage across the junctions. However, in the absence of an external magnetic flux, the linear response of the SQUID to small changes in the current signal will be zero. In order to maximize the SQUID response and linearity, an external flux is applied with the current I_{in}. When I_{in} creates a flux of about $\frac{n}{2}\phi_0$ (shown in Fig. 4.7 by a vertical line), then the SQUID is maximally responsive to changes in the current through I_{in}.

One can use a SQUID to amplify a current signal by directing the signal through the SQUID input coil. As is evident from the $V - \phi$ curves in Fig. 4.5, the SQUID response is highly non-linear. In order to linearize the SQUID response, we apply a nulling flux to the SQUID that attempts to exactly cancel the flux due to the signal current. This nulling flux is created by driving a current, I_{null} through an input coil inductively coupled to the SQUID. The DfMux architecture uses a single input coil (see Fig. 4.8), but it is also possible to use a separate input coil exclusively for SQUID linearization. In the former configuration, $I_{null} = -I_{signal}$ and $I_{in} = I_{fb}$. Since I_{in} is constant, the SQUID remains at a fixed location in its $V - \phi$ curve and its response is linearized.

To measure the signal current, we need only know the nulling current required to null the SQUID.

Digital Active Nulling (DAN) is the form of SQUID nulling that is used in PB-2. Rather than using a broadband negative feedback loop as was used in earlier iterations of DfMux, DAN is used to null the SQUID in narrow bands around the detector bias frequencies. Because DAN is not a broadband nulling technique, the constraints on the wiring impedance between the SQUID and feedback electronics are relaxed significantly, allowing the use of higher frequency bias tones. This was one of the important technological developments that allowed for the increase in PB-2's multiplexing factor.

In PB-2, eight SQUIDs are mounted to a printed circuit board called a SQUID card. The SQUID card has electrical connections to apply the necessary biases and nulling signal to the SQUIDs from the room temperature readout electronics. In addition, each SQUID is paired with a bias resistor that is used to form the voltage bias for a comb of TESs.

Because SQUIDs are so sensitive to external magnetic fields, great care must be taken to shield them from unwanted magnetic flux (e.g. from the Earth's magnetic field). Each SQUID is mounted on the SQUID card with a superconducting niobium ground plane beneath it and the entire SQUID card is surrounded by a high-permeability cryoperm shield [50].

To address noise created by the SQUID, many SQUIDs are often arrayed in series to form what is called a SQUID series array. When N SQUIDs are arrayed in series, the output signal of the SQUID is multiplied by N and the uncorrelated noise is increased by $\sqrt{N}$, leading to an overall increase in signal to noise of $\sqrt{N}$. The PB-2 SQUIDs are series array SQUIDs.

LC Resonators

Channel frequencies are defined by superconducting, lithographed LC resonators. The electrical bandwidth of the bias circuit is set by the inductance of each channel along with the TES resistance. The required electrical bandwidth is approximately constant for every channel, so the inductance is held constant and the capacitance is varied in order to create forty unique

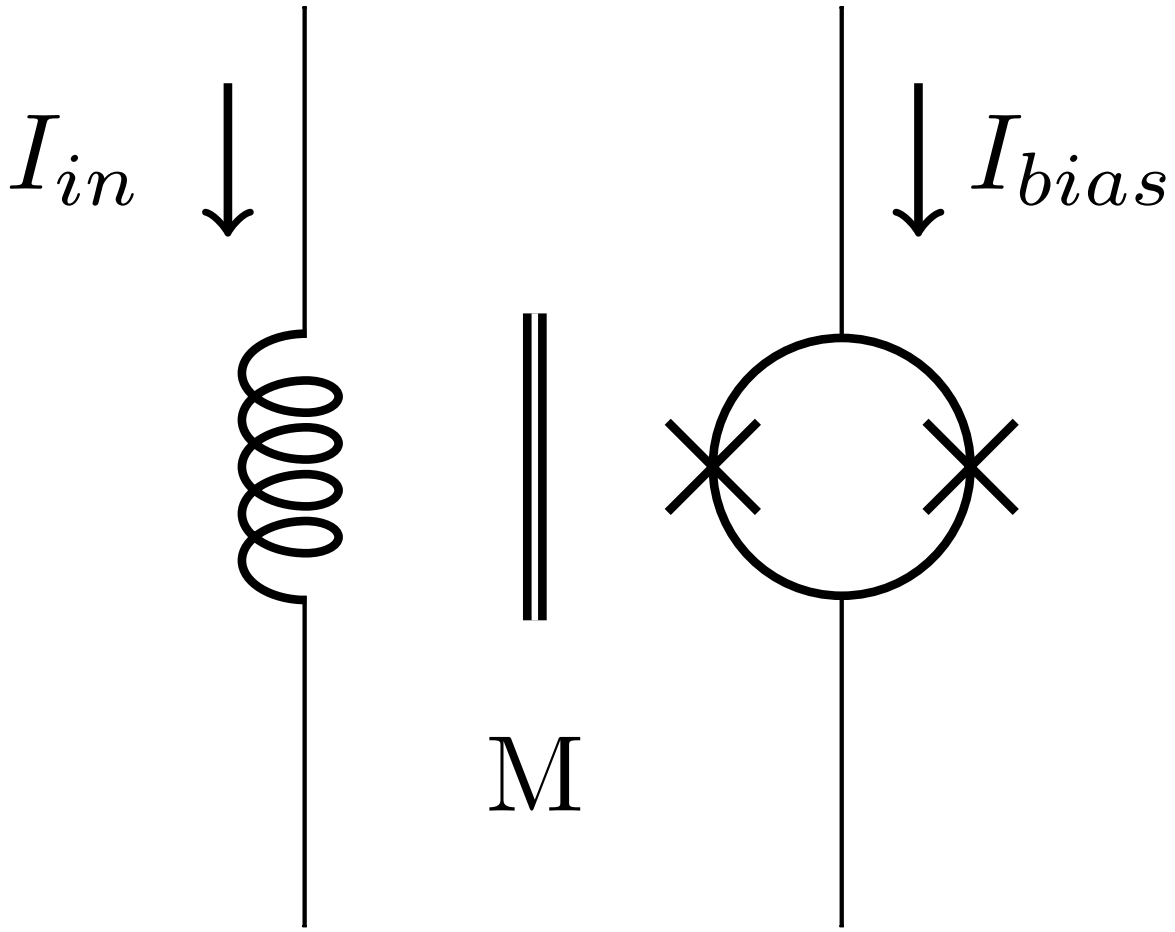

Figure 4.5: DC SQUID schematic. A current bias, I_{bias} is applied to the SQUID in order to put the Josephson junctions into a responsive state. The SQUID is inductively couple to an input coil with mutual inductance M. A current driven through the input coil, I_{in}, creates a magnetic flux in the SQUID, which drives a screening current.

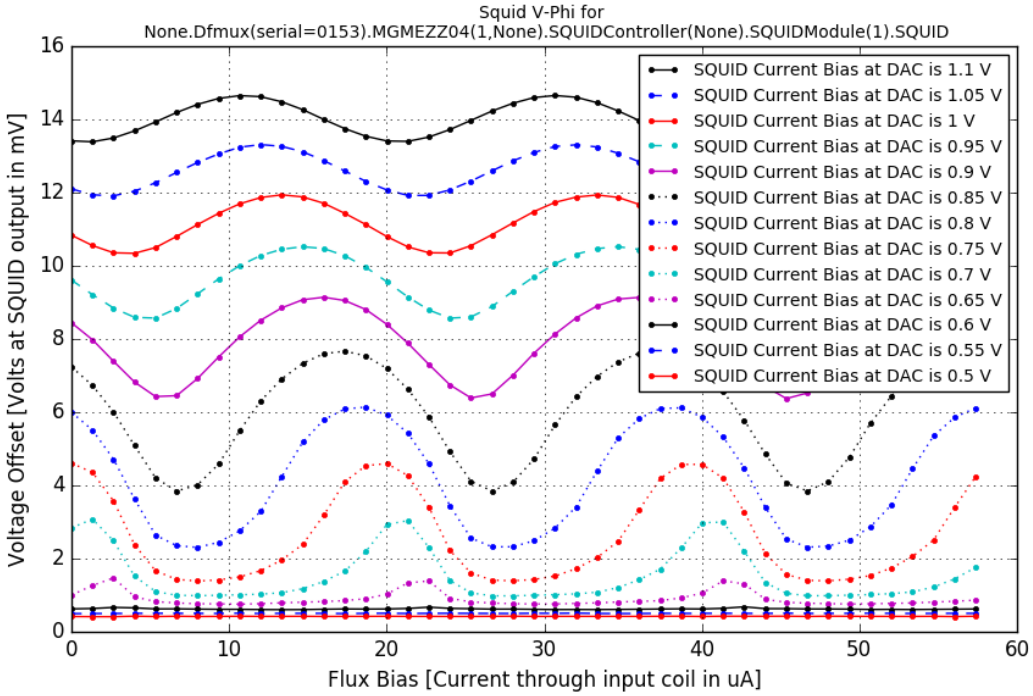

Figure 4.6: The response curve of a SQUID is shown for varying values of I_{bias} and I_{in}. Each colored line is a sweep of I_{in} while holding I_{bias} constant.

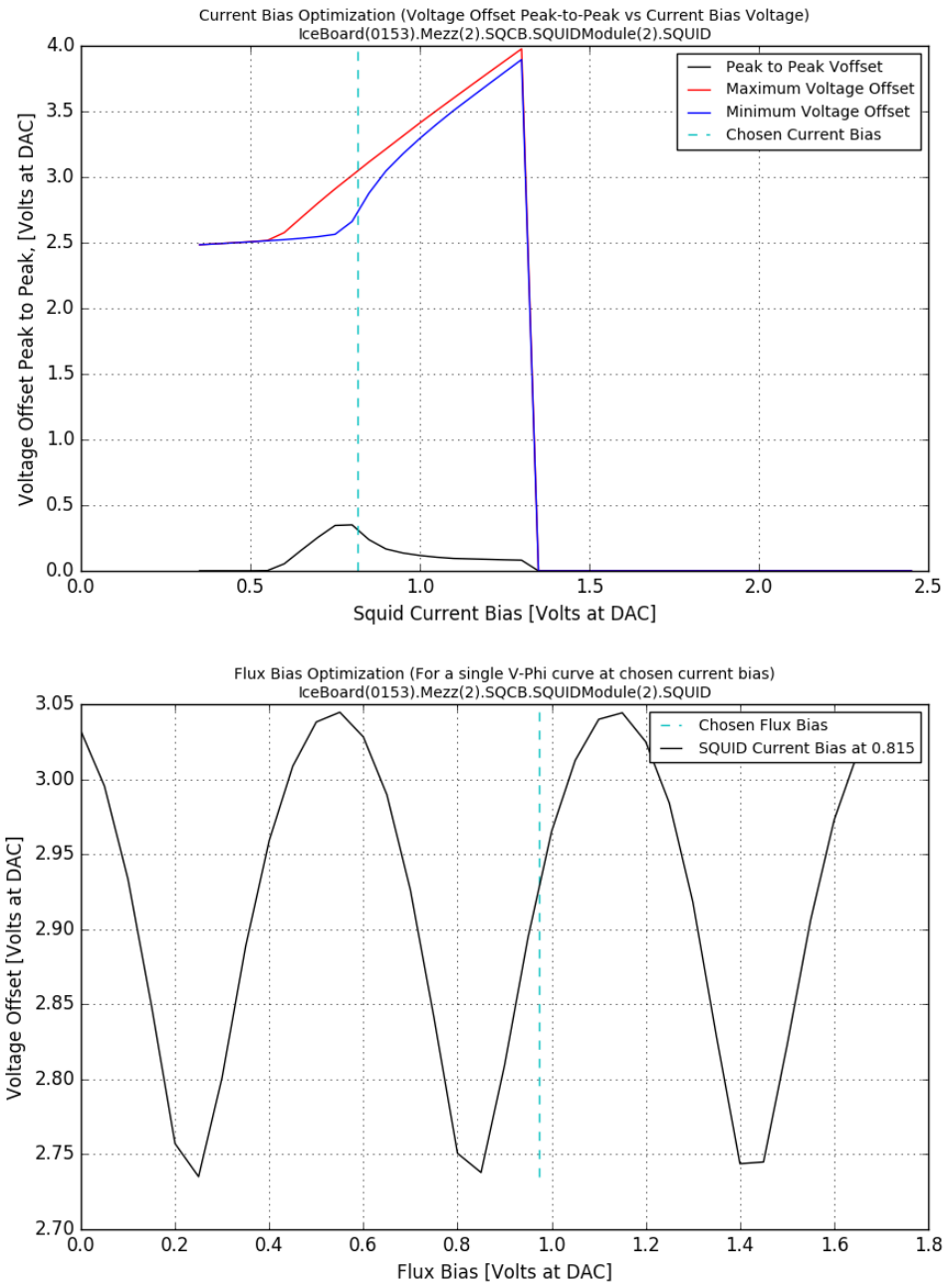

Figure 4.7: *Top:* The voltage across the SQUID is plotted as a function of bias current for flux biases that maximize (red) and minimize (blue) the screening current. The horizontal and vertical axes show values measured at the digital-to-analog converters rather than at the SQUID.

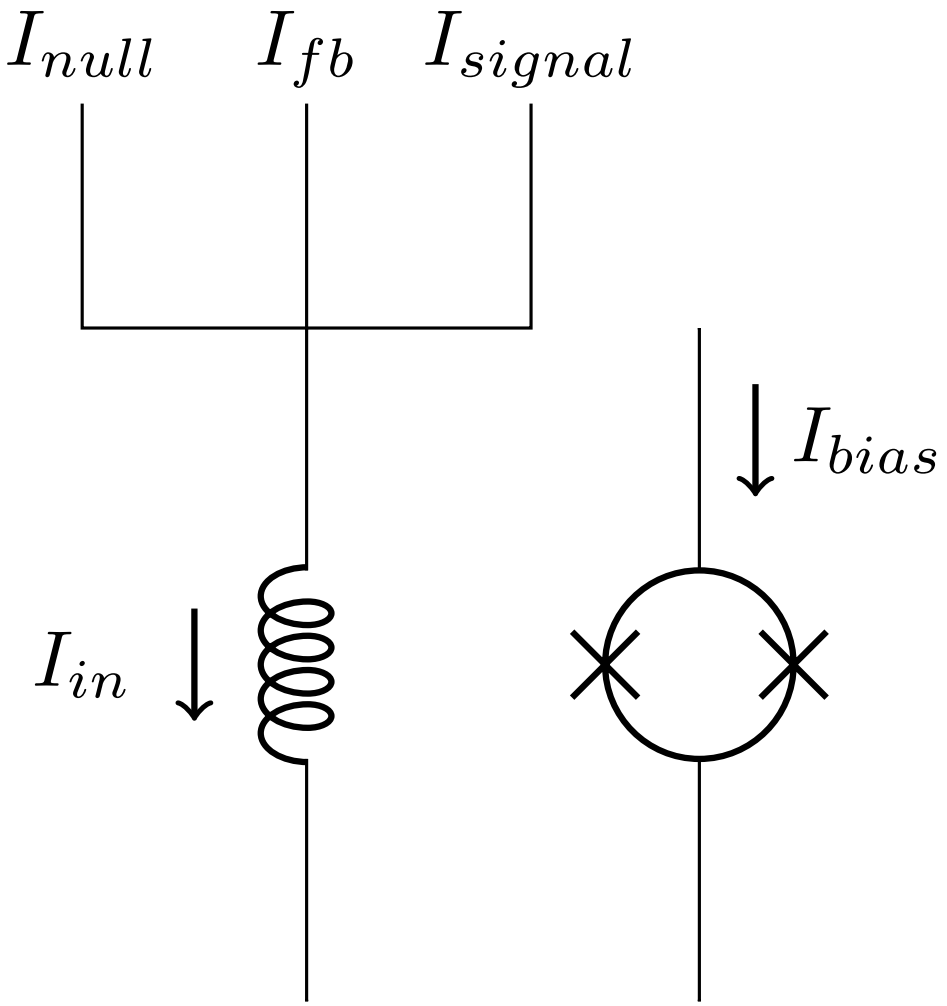

Figure 4.8: The SQUID input coil has three currents driven through it. The flux bias, fb is a constant DC current. The signal current, I_{signal}, is a AC current from the TES. The nulling current, I_{null} attempts to null the current from I_{signal} so that $I_{in} = I_{fb}$.

resonant frequencies.

Losses in the LC resonators constitute a stray impedance that creates crosstalk and affects detector performance. Dielectric loss in capacitors is difficult to avoid, but it has been mitigated with the design of lithographed spiral inductors and interdigitated capacitors [42]. To avoid Ohmic loss in conductors, a superconductor is used to create the LC circuits. PB-2a uses aluminum while PB-2b and PB-2c use niobium. There is no expectation that either will perform significantly differently during TES operations, but each have advantages outside of this. Aluminum is much easier to wirebond, making the assembly simpler. Niobium superconducts at a much higher temperature, meaning that the resonant frequencies are less susceptible to kinetic inductance changes over the few hundred milli-kelvin changes during cycling of the sub-Kelvin refrigerator. Each LC chip is surrounded by a superconducting shield to prevent inductive coupling to other chips and to prevent Eddy losses in nearby normal metals.

Striplines

This subsection is about the cryogenic readout cables that carry the TES bias from the bias element to the LC filters and back to the SQUID input coil. We usually call these cables striplines, but it is worth noting that each cable is actually composed of two broadside-coupled striplines and each cable is used to bias and read out two combs of TES detectors. There are two lengths of striplines used in the PB-2 receivers: 60 cm and 75 cm. Because of the large size of the focal plane, the shorter length striplines do not suffice to reach the TES wafers furthest from the SQUID cards. There are 15 striplines used per wafer and seven wafers per receiver for a total of 210 striplines used per receiver. Striplines are a significant contributor to stray impedance in the DfMux cryogenic circuit and thermal loading on the bolometer stage, so their design had to be carefully optimized.

Because the striplines create a thermal path between the 4 K SQUID card and 0.3 K bolometer stage, it is important that they have low thermal conductivity. They are designed to

meet this requirement by using niobium-titanium conductors and polyimide sheathing. NbTi superconducts at 9 K and its thermal conductivity is very small below that temperature. The expected thermal loading from a single stripline connected directly from a SQUID card to the bolometer stage is about 20 nW [43], which corresponds to about 2 μW for a fully populated focal plane of striplines. This should be looked at as an upper limit on the loading because the striplines are actually thermally intercepted at 1 K and 0.4 K before the reach the bolometer stage. The thermal intercept points allow for some fraction of the power to be shunted to the higher temperature and higher cooling power stages of the sub-Kelvin cooler. Note that this consideration becomes less important as the length of the stripline is increased until the stripline loading becomes subdominant to the other sources of loading. The sub-Kelvin coolers used in the PB-2 receivers have cooling powers of a few μW at the bolometer stage.

The other constraint on the stripline design is that their impedance is one of the dominant sources of stray impedance in the cryogenic DfMux circuit. Because the conductors are made from NbTi, their resistance should be negligible. The inductance of the cable, however, is important when working with bias frequencies of a few MHz. Some of the inductance of the stripline is "tuned out" by shifting the resonant frequencies of the LC filters, but not all of it. A small fraction of the inductance is converted into a real impedance that acts as a voltage divider with the comb. This creates crosstalk and poor detector performance. The measured stripline inductance for a 60 cm stripline is 21 nH [43]. This has been demonstrated to achieve acceptable crosstalk performance [43, 51].

4.2.5 Assembly of DfMux Readout Circuit

The PB-2 cryogenic readout circuit consists of five pieces of hardware, listed in the first column of Tab. 4.2. In order to facilitate permutations of detectors and readout hardware, we have developed three modular assemblies called the SQUID (Superconducting Quantum Interference Device) card, the TES wafer, and the readout quantum. Each SA receiver needs seven TES wafers,

Table 4.2: The components required to bias and read out a TES wafer are shown. The five hardware components required to bias a TES wafer are listed in the first column. The LC board, cryogenic readout cable, and SQUID card have sub-components that are listed in the second column. Each LC board houses two LC chips, each of which have the forty inductors and capacitors. The cryogenic readout cable has two NbTi broadside-coupled striplines. Each SQUID card can house up to eight SQUIDs and eight bias resistors.

Component	**Sub-component**	**Quantity**
TES Wafer	—	1
Adapter board	—	4
LC Board		15
	LC chip	30
Cryogenic readout cable		15
	Broadside-coupled stripline	30
SQUID card		4
	SQUID chip	30
	Bias resistor	30

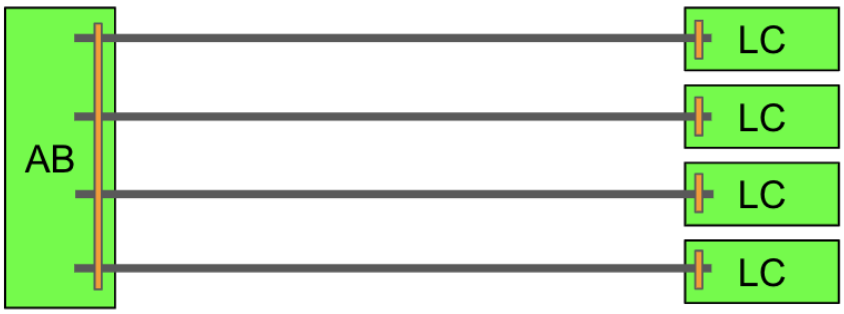

Figure 4.9: A readout quantum consists of an adapter board (AB) connected to LC boards (LC) with cryogenic readout cables.

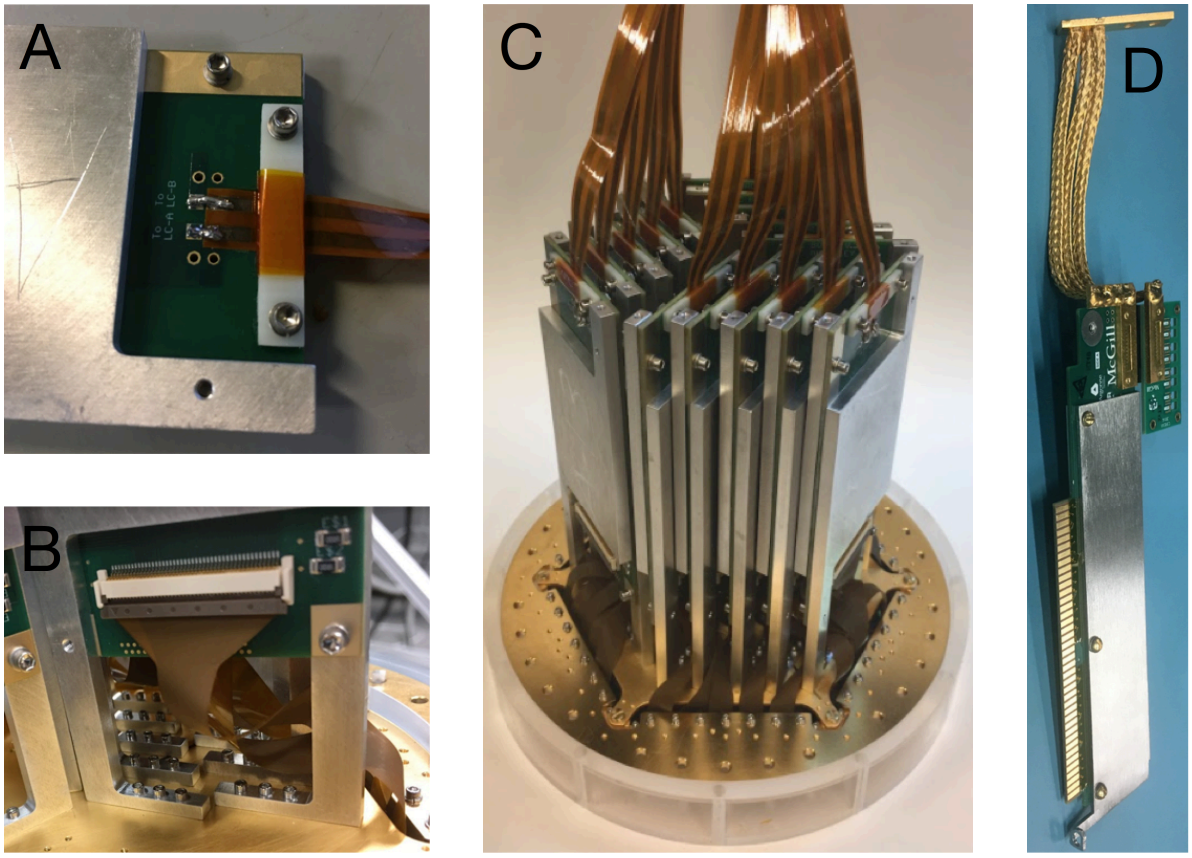

Figure 4.10: Photos of the assembly of a TES wafer and cryogenic DfMux circuit. *Top left:* A cryogenic readout cable is soldered to an LC board and secured with a G-10 clamp. *Bottom left:* The electrical interface between the LC boards and the TES wafer is made with low resistance ZIF connectors. *Middle:* Fifteen LC boards are installed on a TES wafer. Each LC board has a cryogenic readout cable attached. *Right:* A gold-plated OFHC copper heat strap is attached to a SQUID card and an adapter board. The adapter board does not yet have readout cables attached.

28 readout quanta, and 28 SQUID cards, so it is crucial that the assembly of these modules is repeatable. The assemblies undergo shipping, handling, and thermal cycling, so they need to be robust to vibrations and stress. We focus here on the assembly of the readout quantum and the SQUID card and the interfaces between the three modular assemblies.

A readout quantum consists of three or four LC boards, an equal number of cryogenic readout cables, and one adapter board. A readout quantum with four (three) LC boards is called a large (small) readout quantum. Each TES wafer requires fifteen LC boards, so we use three large readout quanta and one small readout quantum per wafer. Each LC board is soldered to

a single cryogenic readout cable and all of the readout cables are soldered to a single adapter board. Tin-lead solder alone does not adhere to NbTi, so we use a combination of ultrasonic solder and tin-lead eutectic solder. Fig. 4.10 shows the solder and strain relief on an LC board. A G-10 clamp provides strain relief to the cryogenic cables. The strain relief clamp does not protect against the stress imposed by differential thermal contraction or vibrations during shipping, so we vet each solder connection by brushing it vigorously with a stiff brush. This has been an effective method to identify mechanically weak connections, which we preemptively repair in order to avoid failures during testing or CMB observations. Repair typically entails either reapplying solder or replacing the cryogenic readout cable.

LC boards are mounted to the back of the TES wafer and connected electrically with low-resistance Zero Insertion Force connectors ($\sim$ 15 mΩ contact resistance) (Fig. 4.10). Each TES wafer requires fifteen LC boards, so we use three large readout quanta and one small readout quantum per wafer. After LC installation, we install a low-emissivity, gold-plated oxygen-free high conductivity (OFHC) copper can that surrounds the LC boards and provides radiative shielding and mechanical support.

Mating low-impedance micro-D connectors are used to connect the adapter board and SQUID card. These connectors have contact resistance of 26 mΩ and inductance of 20 nH. A gold-plated OFHC copper strap is used to provide a thermal path between the 4 K cryostat walls, the SQUID card, and the adapter board (shown in Fig. 4.10).

4.2.6 Readout noise

When observing the CMB, the readout noise level can be calibrated to a sky temperature by observing a source with known brightness. In the lab, this is not possible and the noise is often referred to a current noise at the input of the SQUID.

There are several known sources of readout noise in the DfMux system [47, 52, 44]: amplifier noise, noise in the digital-to-analog converters (DAC), quantization noise in the analog-

to-digital conversion, Johnson noise, and SQUID noise. These noise sources are referred to the input of the SQUID depending on whether they are in the carrier, nuller, or demodulator chain. Carrier noise is expected to act as a voltage noise across the comb, so its resulting current noise is suppressed by the impedance of the comb. This current noise is negligible away from LC resonances and significant near LC resonances. Nuller chain noise is broadband current noise injected into the SQUID through the nuller path. Demodulator chain noise results from the measurement of the SQUID output voltage and demodulation to determine the appropriate nulling current. Demodulator noise depends on the SQUID transimpedance and may also be affected by the SQUID output impedance and parasitic impedances of the SQUID.

Additionally, there is a source of noise amplification that results from a nuance of the SQUID nulling scheme [44]. DAN enforces that the output of the demodulator is zero, rather than that the output of the SQUID is zero. Because of this, any noise that is picked up between the SQUID and the demodulator gets fed back to the SQUID through the nuller. The strength of this effect is approximately proportional to the SQUID input coil impedance, so it is more important at the highest bias frequencies. SA has chosen low inductance SQUIDs that make this noise source unimportant to the total readout noise level.

4.3 Acknowledgments

Sec. 4.2.5 is a reprint of material as it appears in T. Elleflot, Y. Akiba, K. Arnold, J. Avva, D. Barron, A. N. Bender, A. Cukierman, T. deHaan, M. Dobbs, J. Groh, M. Hasegawa, M. Hazumi, W. Holzapfel, L. Howe, G. Jaehnig, B. Keating, A. Kusaka, A. T. Lee, L. Lowry, J. Montgomery, H. Nishino, C. Raum, K. M. Rotermund, M. Silva-Feaver, A. Suzuki, B. Westbrook, and N. Whitehorn, "Detector and readout assembly and characterization for the simons array," Journal of Low Temperature Physics, vol. 193, pp. 1094–1102, Dec 2018. The dissertation author was the primary author of this work.

Chapter 5

Detector and Readout Characterization for Simons Array

This chapter describes the detector and readout characterization performed by the author for the Simons Array (SA). Detector characterization was necessary to provide feedback on detector fabrication and to choose which detector wafers to deploy with each receiver. Accurate detector characterization relies on a model of the stray impedance in the detector bias circuit. A stray impedance model and its implications on detector characterization and performance are described in Sec. 5.1. The methods and results of detector characterization for several PB-2a and PB-2b detector wafers are described in Sec. 5.2. The effects of stray impedance on detector performance are shown in Secs. 5.2.5 and 5.3.3.

5.1 Stray Impedance Model

In order to understand the effects of stray impedance on Transition Edge Sensor (TES) characterization and performance for POLARBEAR-2, I have developed a model of the TES bias circuit shown in Fig. 5.1. The approach developed here differs from previous works [53, 54] in

that the model parameters for each detector were measured in-situ during TES characterization, corrections were applied to all measured TES parameters, and the corrections applied were based on the measured values of the model parameters rather than average values or templates. Additionally, implications of this model on the small-signal response of the TES are studied in and compared to data in Sec. 5.2.5 and 5.3.3.

In this model, each TES with resistance R is placed in series with a stray resistance R_s. The series combination of R_s and the TES are biased with a voltage, V, which is formed by driving an alternating current, I_{in}, at frequency f_{bias} through a bias resistor, R_{bias}, and an associated stray bias inductance, L_{bias}. The resulting current driven through the TES is I. V, I, and R are defined below as the sum of a steady-state value, labeled with a subscript 0, and a small, time-dependent value, labeled with a prefix δ, below.

$$V = (V_0 + \delta V(t))\cos(2\pi f_{bias} t) \tag{5.1}$$

$$I = (I_0 + \delta I(t))\cos(2\pi f_{bias} t) \tag{5.2}$$

$$R = R_0 + \delta R(t) \tag{5.3}$$

This model is agnostic to the source of R_s aside from assuming that it has the effect of a real series resistance. The bias inductance is likely sourced by a combination of the stray inductance of the surface mount bias resistor and the inductance of the traces on PCB.

The implications of this model are twofold. First, the voltage across the TES is different than the raw voltage reported by our readout software. This is caused by both the bias inductance and stray series resistance. We need to calibrate our data in order to accurately characterize detectors. Second, the voltage across the TES is not stiff, but depends on the TES resistance. This effects electrothermal feedback and must be accounted for.

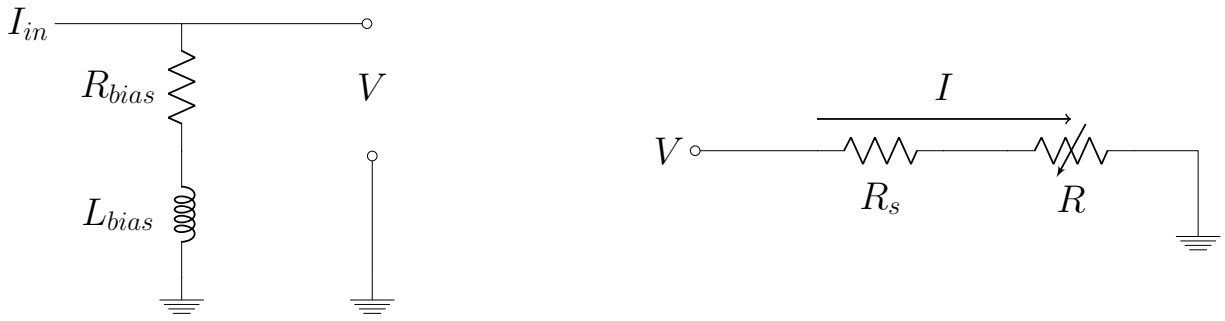

Figure 5.1: The stray impedance model used to measure detector properties is shown. *Left:* The voltage bias is formed by driving a current, I_c, through the series combination of the 30 mΩ bias resistor, R_{bias}, and and associated stray bias inductance, L_{bias}. *Right:* The TES, R, is in series with a series stray resistance, R_s. The voltage bias is applied to both, driving a current, I.

5.1.1 Calibrating Raw Data

This section describes how to calibrate the raw voltage bias reported by the Digital Frequency Multiplexing (DfMux) control software, V^{raw}, in order to retrieve the actual voltage bias, V, and voltage on the TES, V_{TES}. These values are different for two reasons. First, V^{raw} is calculated under the assumption that $L_{bias} = 0$, which leads to an underestimate of the actual voltage bias applied. Second, stray impedance in the cryogenic circuit forms a voltage divider with the TES, so only a fraction of the voltage bias is applied to the TES, so $V_{TES} < V$.

A priori, we have do not know the value of the bias inductance. And even if we have measured it, it may change due to variations in electrical components, hardware design, or assembly variability. It is thus a natural choice to start by assuming that L_{bias} is negligible. This is what is done in the DfMux control software. The voltage reported by the software is V^{raw} and it is calculated as follows:

$$V^{raw} = I_{in} R_{bias}. \tag{5.4}$$

The actual voltage bias created is

$$V = I_{in} Z_{bias} \tag{5.5}$$

$$= V^{raw} \frac{Z_{bias}}{R_{bias}}. \tag{5.6}$$

In Eq. 5.5, Z_{bias} is the total impedance of the bias resistor and stray bias inductance,

$$Z_{bias} = R_{bias} + 2\pi i f_{bias} L_{bias}. \tag{5.7}$$

When L_{bias} is nonzero, $|V| > |V^{raw}|$ and the ratio of $|V|$ to $|V^{raw}|$ grows with frequency. The challenge then is to determine whether or not L_{bias} is big enough to matter and, if so, to measure L_{bias}. A method of measuring L_{bias} in-situ during TES characterization is described in Sec. 5.2.4. The result of those measurements indicated that $L_{bias} \approx 1$ nH. If left uncalibrated (i.e. if we assume that $V = V^{raw}$), we will underestimate the voltage bias and values derived from it by 5-30% across the bias frequency range of 1.5-4.5 MHz.

The stray series resistance acts as a voltage divider with the TES. The voltage across the TES is given by:

$$V_{TES} = V - IR_s \tag{5.8}$$

$$= V \frac{R}{R + R_s}. \tag{5.9}$$

Similarly to the bias inductance, we must determine whether R_s is large enough to affect TES characterization and, if so, measure it and remove its effect. A method of measuring R_s in-situ is described in Sec. 5.2. Typical values of R_s are 0.15-0.5 Ω.

The measured values of current do not need to be calibrated for either of the stray impedance terms.

5.1.2 Small-Signal Analysis

Stray series resistance reduces the stiffness of the voltage bias on the TES, changing its behvaior under electrothermal feedback. It is instructive to investigate the effect of the stray series resistance on the TES small-signal response. The proceeding follows the derivation of the responsivity of a DC-biased TES with a series resistance in [46] and the derivation of the responsivity of an AC-biased TES in [47].

It is worth noting that the electrical bandwidth of the circuit in Fig. 5.1 is infinite because there is no reactive element in the circuit. This is a justifiable approximation of the actual DfMux cryogenic circuit because the its bandwidth is much larger than the bandwidth of a PB-2 TES. The electrical bandwidth of the actual DfMux cryogenic circuit depends on the resistance of the TES and the inductance of the resonator. For an inductance of 60 nH and TES resistance of 1 (0.5) Ω, the electrical bandwidth is 1.6 (0.8) kHz. The lowest time constants measured for PB-2 TESs is about 2 ms, corresponding to 80 Hz of bandwidth. Even in the case that the electrical bandwidth is at its minimum and the TES bandwidth is at its maximum, they are different by a factor of ten. During most of the TES transition, the ratio of bandwidths will be larger than ten.

Conservation of energy requires that the total power flowing to the TES is equal to its time rate of change of energy:

$$P_{opt} + P_{bath} + P_{elec} = \frac{dE}{dt}. \tag{5.10}$$

Using Eqs. 5.2 and 5.3, P_{elec} can be expressed as

$$\begin{aligned} P_{elec} &= \langle I^2 R \rangle \\ &= P_{elec,0}\Big(1 + 2\frac{\delta I}{I_0} + \frac{\delta R}{R_0}\Big). \end{aligned} \tag{5.11}$$

In Eq. 5.11, $\langle\ \rangle$ denotes a time average of one period of the current oscillation and $P_{elec,0}$ is the

steady state Joule power:

$$P_{elec,0} = \frac{1}{2} I_0^2 R_0 \tag{5.12}$$

The remaining terms can be written as

$$P_{opt} = P_{opt,0} + \delta P_{opt}, \tag{5.13}$$

$$P_{bath} = P_{bath,0} - G\delta T, \tag{5.14}$$

and

$$E = E_0 + C\delta T, \tag{5.15}$$

where steady-state values are denoted with subscripts 0, time-varying terms are denoted with prefixes δ, G is the differential thermal conductance $G \equiv dP_{bath}/dT$, and C is the differential heat capacity $C \equiv dE/dT$. Substituting Eqs. 5.11, 5.13, 5.14, and 5.15 in Eq. 5.10 and performing a Fourier transform leaves us with the small-signal equation for a TES in the bias circuit of Fig. 5.1:

$$\delta P_{opt} - G\delta T + P_{elec,0}\Big(2\frac{\delta I}{I_0} + \frac{\delta R}{R_0}\Big) = i\omega C\delta T. \tag{5.16}$$

Eq. 5.16 will be more useful if it is written in terms of variables that we can control or measure, i.e. voltage, current, and optical power. To that end, I will substitute the equations below in 5.16.

$$\frac{\delta R}{R_0} = \Big(\frac{R_0 + R_s}{R_0}\Big)\Big(\frac{\delta V}{V_0} - \frac{\delta I}{I_0}\Big) \tag{5.17}$$

$$\delta T = \frac{T_0}{\alpha}\frac{\delta R}{R_0} \tag{5.18}$$

Eq. 5.17 is from Ohm's law and Eq. 5.18 is a Taylor series expansion on $R = R(T)$ with α defined as

$$\alpha = \left.\frac{d\ln(\frac{\delta R}{R})}{d\ln(\frac{\delta T}{T})}\right|_{T=T_0}. \tag{5.19}$$

Additionally, I will substitute the loop gain, $\mathcal{L}$, in Eq. 5.16, defined as

$$\mathcal{L} = \frac{\alpha P_{elec,0}}{G T_0}. \tag{5.20}$$

After these substitutions, Eq. 5.16 can be rewritten as

$$\frac{\delta P_{opt}}{P_{elec}} = \frac{-1}{\mathcal{L}} \left(\frac{R_0 + R_s}{R_0 - R_s} \right) \left[\left(\mathcal{L} - 1 - i\omega\tau_0 \right) \frac{\delta V}{V} + \left(\mathcal{L} \frac{R_0 - R_s}{R_0 + R_s} + 1 + i\omega\tau_0 \right) \frac{\delta I}{I} \right] \tag{5.21}$$

Eq. 5.21 is the equation for the small-signal response of a TES in the bias circuit of Fig. 5.1. I will now evaluate two special cases of Eq. 5.21. The first is representative of the conditions under which Cosmic Microwave Background (CMB) observations are performed and the second of the conditions under which dark detector characterization is performed.

Constant Voltage

During CMB observations, the voltage bias is held constant, which means $\delta V = 0$. Note that this does *not* mean that the voltage across the TES is held constant. The voltage across the TES is given by

$$V_{TES} = V \frac{R}{R + R_s} \tag{5.22}$$

$$= (V_0 + \delta V) \frac{R_0 + \delta R}{R_0 + \delta R + R_s}. \tag{5.23}$$

By setting δV to zero, we are eliminating only one of the two time-dependent quantities from Eq. 5.23. The fact that V_{TES} depends on δR produces interesting changes in the behavior of the TES relative to the ideal case with a stiff voltage bias across the TES, such as increased responsivity and time constant and a new stability criterion.

When we substitute $\delta V = 0$, Eq. 5.21 reduces to:

$$\frac{\delta P_{opt}}{P_{elec}} = \frac{-1}{\mathcal{L}}\left(\frac{R_0+R_s}{R_0-R_s}\right)\left(\mathcal{L}\frac{R_0-R_s}{R_0+R_s}+1+i\omega\tau_0\right)\frac{\delta I}{I} \tag{5.24}$$

We can rearrange Eq 5.24 to retrieve the small-signal responsivity, $S_I \equiv \delta I/\delta P_{opt}$:

$$S_I = \frac{\delta I}{\delta P_{opt}} = -\frac{2}{V_0}\frac{\mathcal{L}}{\mathcal{L}\frac{R_0-R_s}{R_0+R_s}+1+i\omega\tau_0} \tag{5.25}$$

This is the equation of a single pole low-pass filter with time constant given by:

$$\tau = \frac{\tau_0}{\mathcal{L}\frac{R_0-R_s}{R_0+R_s}+1} \tag{5.26}$$

If we further simplify by setting R_s to zero, then we recover the well-known AC-biased responsivity and time constant in [47, 46]:

$$S_I = \frac{\delta I}{\delta P_{opt}} = -\frac{2}{V_0}\frac{\mathcal{L}}{\mathcal{L}+1+i\omega\tau_0} \tag{5.27}$$

and

$$\tau = \frac{\tau_0}{\mathcal{L}+1}. \tag{5.28}$$

We can see the effect of stray impedance on the small-signal responsivity by comparing Eqs. 5.25 and 5.27. The high loop gain limit of Eq. 5.27 is achieved when $\mathcal{L} >> 1$ and results in a responsivity that asymptotically approaches $-2/V_0$. To achieve the same asymptotic behavior of the responsivity in Eq. 5.25, $\mathcal{L} >> 1$ is necessary but not sufficient. This is because the coefficient of $\mathcal{L}$ in the denominator of Eq. 5.25 can be much less than one. The high loop gain condition for Eq. 5.25 is achieved when

$$\mathcal{L}\left(\frac{R_0-R_s}{R_0+R_s}\right) >> 1. \tag{5.29}$$

Note that as the detector resistance decreases, the loop gain may increase but the term in parentheses will decrease. There will likely be a range of detector resistance values, bounded above and below, in which the high loop gain limit is met.

In the high loop gain limit, Eq. 5.25 is given by:

$$S_I = -\frac{2}{V_0}\left(\frac{R_0 + R_s}{R_0 - R_s}\right). \tag{5.30}$$

When $R_0 > R_s$, the term in parentheses in Eq. 5.30 is greater than one, so the high loop gain responsivity is enhanced by R_s. Typical values of R_0 and R_s for a PB-2 detector in operation are R_0=0.7 Ω and R_s = 0.25 Ω. For these values, the high loop gain limit is achieved when $\mathcal{L} >> 2$. The responsivity enhancement associated with these values of R_0 and R_s in the high loop gain limit is a factor of about 1.8. If $R_0 < R_s$, the high loop gain responsivity in Eq. 5.30 changes sign and the TES becomes unstable. A plot of responsivity as a function of $\mathcal{L}$ and R_s is shown in Fig. 5.2.

Similarly, we can see the effect of R_s on the detector time constant by comparing Eqs. 5.26 and 5.28. The time constant of a TES without a stray resistance is always positive and gets smaller as the loop gain grows. In the presence of a stray resistance, Eq. 5.26 shows that the time constant is affected not just by the loop gain but also by the relative value of the stray resistance to the detector resistance. A stability criterion is that the time constant be positive [46]. When the time constant is negative, the TES experiences thermal runaway. This stability criterion is given by:

$$R_0 > R_s\left(\frac{\mathcal{L} - 1}{\mathcal{L} + 1}\right). \tag{5.31}$$

The stability criterion stated earlier in the section that is caused by the change in sign of the high loop gain responsivity is a special case of Eq. 5.31. if $0 \leq \mathcal{L} < 1$, then the right hand side of Eq. 5.31 is negative and the TES cannot be made unstable by this mechanism. For any finite value of $\mathcal{L}$, a TES should be able to operate stably with $R_0 < R_s$. However, in PB-2 detectors, we have

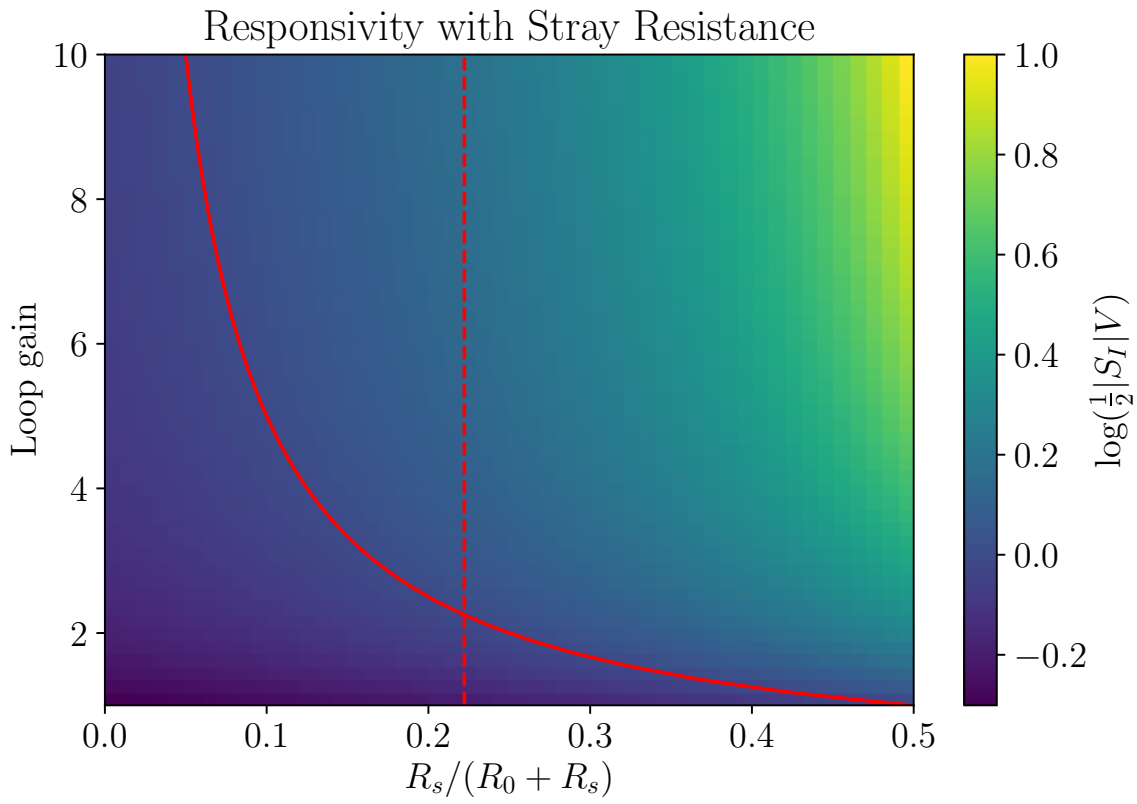

Figure 5.2: Heat map of $\log(\frac{1}{2}|S_I|V)$ as a function of loop gain and $R_s/(R_0+R_s)$. In the absence of stray impedance, this quantity asymptotically approaches zero as the loop gain is increased. The solid red line indicates the contour of $\log(\frac{1}{2}|S_I|V) = 0$. The dashed red line is plotted for R_s=0.2 Ω and R_0= 0.7 Ω, which approximates the detector and stray resistance in POLARBEAR-2. The intersection of the solid and dashed red lines indicate that the PB-2 TES responsivity should reach $|S_I| = 2/V$ at a loop gain of about $\mathcal{L} = 2$.

not observed stable operation at $R_0 < R_s$. This is likely due to the finite step sizes taken during IV curves. The effect of stray impedances on the TES time constant is shown for a TES with constant loop gain and varying stray resistance in Fig. 5.3.

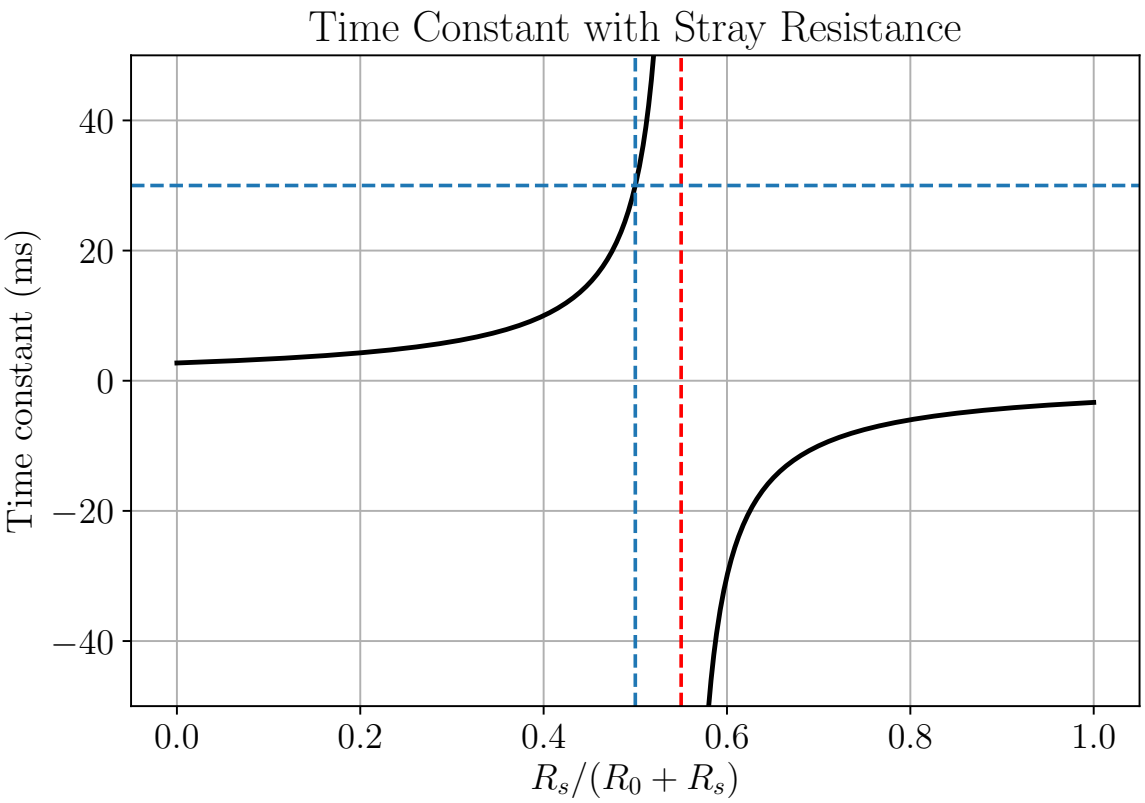

Figure 5.3: This is a plot of the TES time constant, τ, as a function of $R_s/(R_0+R_s)$ for a constant loopgain of $\mathcal{L}=10$ and natural time constant $\tau_0=30$ ms. At low values of $R_s/(R_0+R_s)$, the stray series resistance is unimportant and the time constant is small. As $R_s/(R_0+R_s)$ increases, so does τ. At $R_s/(R_0+R_s)=0.5$, τ has increased to τ_0 (indicated by dashed blue lines). As $R_s/(R_0+R_s)$ increases further, τ grows without bound until reaching the instability point indicated with a dashed red line. Beyond the instability, τ is negative and the TES is unstable.

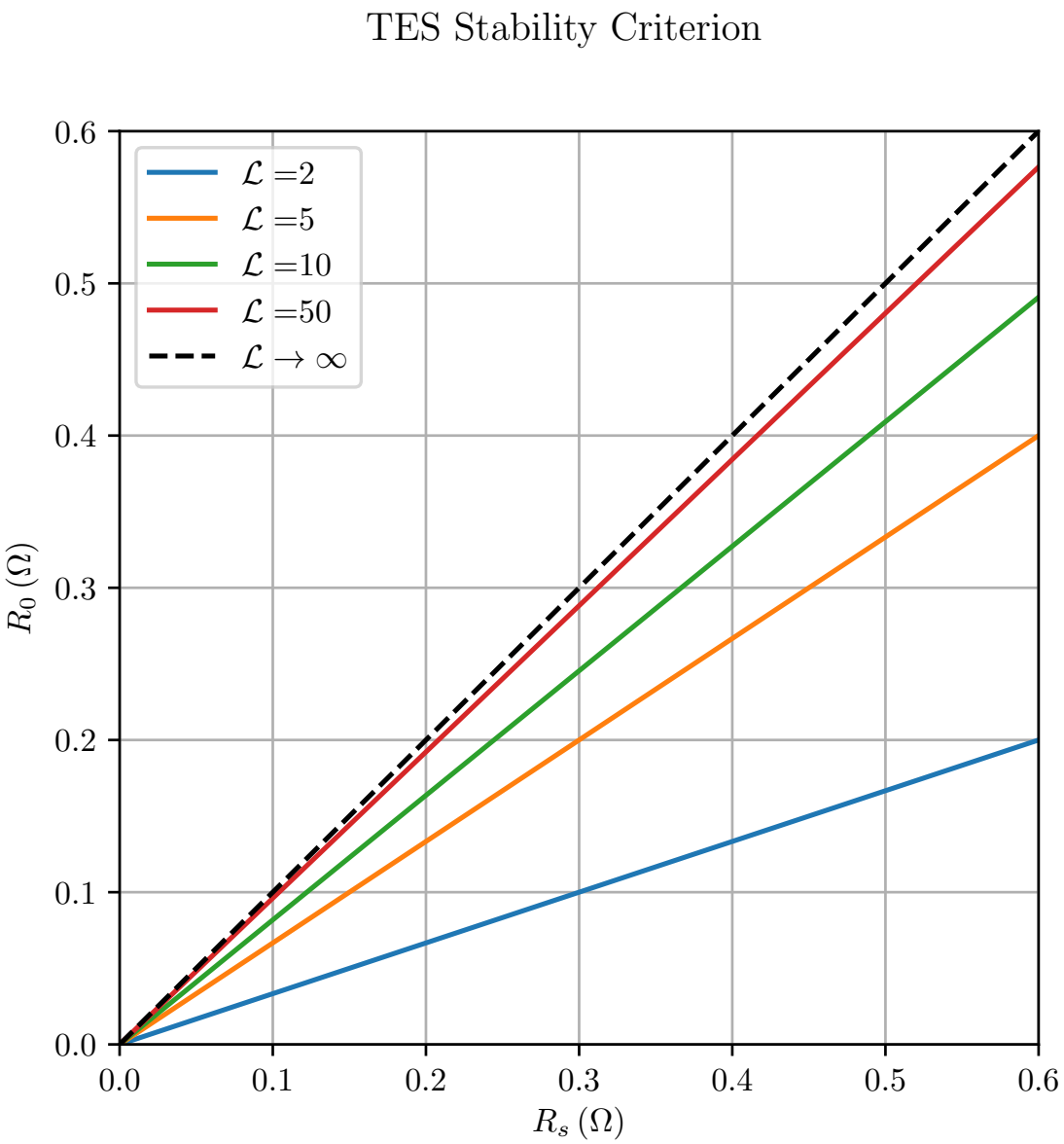

Figure 5.4: The TES stability criterion of Eq. 5.31 is plotted for a few values of loop gain. The region above each curve represents the stable operating region for a TES with the corresponding loop gain. As the loop gain is increased, the stable region becomes smaller. The high loop gain limit of the stability criterion is given by $R_0 > R_s$ and is plotted with a dashed black line.

Constant Optical Power

During dark detector characterization, the optical power on the detector is negligible and unchanging. In that case, we can simplify Eq. 5.21 by setting δP_{opt} to zero:

$$\frac{\delta I}{\delta V} = \left(\frac{1}{R_0 + R_s}\right) \frac{1 - \mathcal{L} + i\omega\tau_0}{\mathcal{L}\left(\frac{R_0 - R_s}{R_0 + R_s}\right) + 1 + i\omega\tau_0}. \tag{5.32}$$

To study the behavior of a TES during an IV curve measurement, we note that the duration of time between voltage steps is much larger than the TES time constant, so it is essentially a steady-stat measurement allowing us to set ω to zero. Doing so yields

$$\frac{\delta I}{\delta V} = \left(\frac{-1}{R_0 + R_s}\right) \frac{\mathcal{L} - 1}{\mathcal{L}\left(\frac{R_0 - R_s}{R_0 + R_s}\right) + 1}. \tag{5.33}$$

Eq. 5.33 gives the slope of an IV curve as a function of loop gain, TES resistance, and series stray resistance. It is instructive to examine the behavior of Eq. 5.33 in a few specific cases.

- When the TES is normal, the loop gain is zero and the slope of the IV curves is $(R_n + R_s)^{-1}$.
- At the turnaround of an IV curve, the slope of the curve is zero and the loop gain is unity.
- At high lop gain, the slope of the IV curve is $(R_0 - R_s)^{-1}$. Note that when $R_0 = R_s$, the slope of the IV curve is infinite and the TES is unstable.
- Finally, when the TES is superconducting, the loop gain is zero and the slope of the IV curve is R_s^{-1}.

We have seen that the TES will be unstable when the loop gain is high and $R_0 = R_s$. This is a specific case of a more general stability criterion. The TES is unstable when the slope of the IV curve is not finite, so a criterion for stability is

$$R_0 > R_s\left(\frac{\mathcal{L} - 1}{\mathcal{L} + 1}\right). \tag{5.34}$$

This is the same criterion for stability that was found by requiring that the time constant is positive in Sec. 5.1.2.

Finally, we can rearrange Eq. 5.33 to solve for the loop gain:

$$\mathcal{L} = \frac{1 - (R_0 + R_s)\frac{\delta I}{\delta V}}{1 + (R_0 - R_s)\frac{\delta I}{\delta V}}. \tag{5.35}$$

5.2 Dark Detector Characterization

In order for Simons Array (SA) to meet its target sensitivity, it is necessary that the instantaneous noise levels of the instruments are not dominated by detector noise and that the detectors are capable of observing in a large fraction of the observation period. These conditions can be met with careful selection of detector parameters. We have chosen a set of target detector parameters to satisfy these conditions.

Dark characterization is the process of measuring TES parameters in the absence of optical power. In this configuration, the only source of power incident on the TES is from the applied voltage bias. This simplifies the interpretation of the collected data because one does not need to measure or otherwise estimate the optical power. It is still necessary, however, to calibrate measured data to account for effects of stray impedances in the DfMux cryogenic circuit. A model for the effects of stray impedances on TES characterization is decribed in Sec. 5.1.

The measurements described in this chapter were performed between 2016 and mid-2019. One of the wafers described here is deployed in PB-2a and 5 will be deployed in PB-2b. The measurements in the Sec. 5.2.4 sec are listed in chronological order.

5.2.1 Detector Targets

The TES parameters measured in dark testing for PB-2 are: critical temperature, T_c; turnaround power, P_{turn}; and normal resistance, R_n. The target parameters for PB-2a and PB-2b

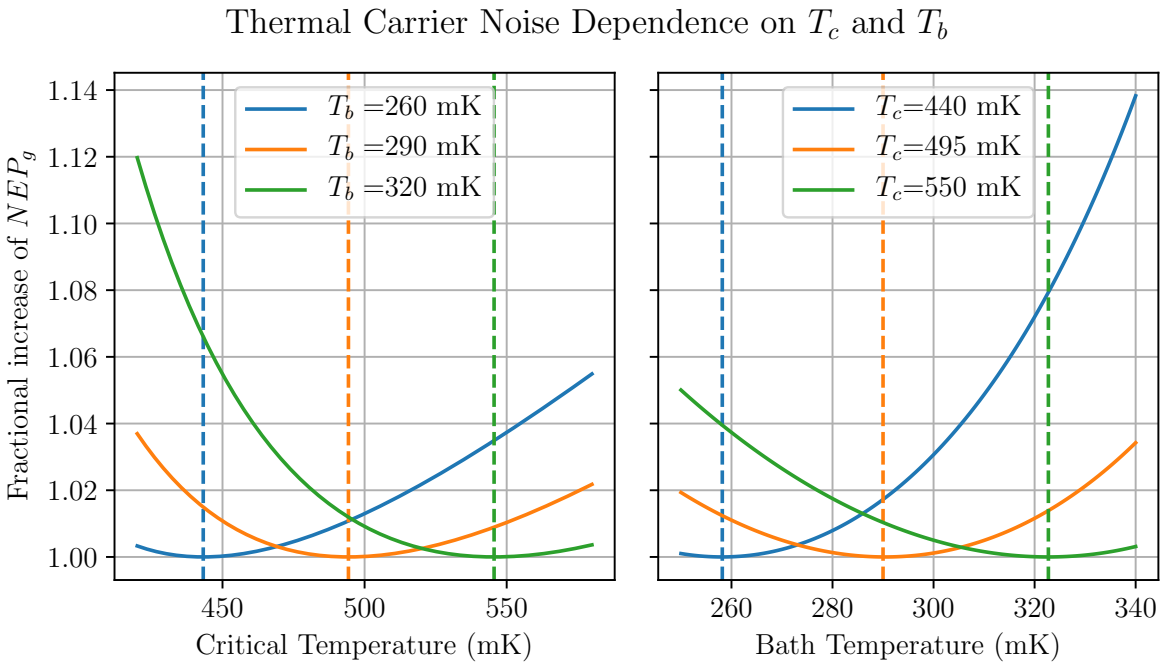

Figure 5.5: NEP_g increase as a function of T_c and T_b relative to optimal values while holding P_{sat} constant and assuming $n = 3$. *Left:* Varying T_c while holding T_b constant for a few values of T_b. *Right:* Varying T_b while holding T_c constant for a few values of T_c.

are listed in Table 5.1.

The optimal critical temperature is set by minimizing the thermal carrier noise assuming a specific value of the bath temperature, T_{bath}, and thermal carrier index, n. The PB-2 bath temperature varies between receivers and is in the range of 260-320 mK, corresponding to an optimal critical temperature in the range of 440-550 mK assuming $n = 3$. The fractional change of thermal carrier noise as a function of T_b and T_c for fixed n and P_{sat} is shown in Fig. 5.5. For the range of T_b and T_c values in the PB-2 receivers, we expect an increase in NEP_g of a few percent relative to the optimal value.

The TES saturation power is important from the perspective of both instantaneous sensitivity and observing efficiency. The thermal carrier noise and readout noise scale with the square root of the saturation power, motivating a small saturation power. However, the smaller the saturation power, the smaller the fraction of time the detector can be used to observe. Total

expected optical power and expected optical power variations on the detector due to changing weather and atmospheric conditions play an important role in determining the target saturation power value. The sky brightness and optical efficiency of the instrument vary with frequency, leading to different expected optical powers for the 90 and 150 GHz bands.

All that being said, the saturation power is an ill-defined quantity that is meant as shorthand for the total power on the detector when it is operating in its superconducting transition. The well-defined quantity that we measure in a dark test is the turnaround power, P_{turn}, defined as the Joule power on the TES when the slope of the IV curve is zero. In the absence of optical power, P_{turn} is approximately 5-10% higher than P_{sat} for PB-2 detectors.

The P_{sat} targets are slightly different for PB-2a and PB-2b because of the difference in temperature of their half-wave plate. Since the PB-2a HWP is at ambient temperature and the PB-2b HWP is cryogenic, we expect more optical loading on the PB-2a detectors. This makes the target saturation powers for PB-2a slightly higher than for PB-2b.

Finally, the normal resistance is chosen such that it is much larger than the stray impedance in the bias circuit. This is required in order to apply a stiff voltage bias to the detector. The stray impedance in the PB-2 DfMux cryogenic circuit is approximately 0.15-0.5 Ω, depending on bias frequency. The primary disadvantage to increasing R_n is that the TES responsivity decreases roughly as the square root of it. However, increasing responsivity has diminishing returns beyond the level needed to suppress readout noise. We chose to set a detector normal resistance target of $1.2 \pm 0.3\ \Omega$ [7].

5.2.2 Dark Test Cryostat

Many of the measurements described in this chapter were performed in a dark test cryostat at UCSD. The cryostat consists of three concentric cylinders, the outermost being a vacuum vessel, the middle a 50 K buffer stage, and the innermost the working area. The working area is a cylinder of about 1 min diameter and 60 cm tall. It is cooled with a combination of a pulse tube

Table 5.1: Target TES parameters for PB-2a and PB-2b. The target values for PB-2a are from [7] and for PB-2b are from the internal POLARBEAR wiki. The motivation for having multiple P_{sat} targets is in the text.

Parameter	Receiver	Target	
		90 GHz	150 GHz
P_{sat}	PB-2a$_x$	7-9 pW	17-24 pW
	PB-2b	7-9 pW	17-21 pW
T_c		420-470 mK	
R_n		0.9-1.5 Ω	

cryocooler (PTC) and a ^{4}He/^{3}He sub-Kelvin refrigerator. The PTC provides a 50 K buffer stage and a 4 K working stage to the cryostat. The sub-Kelvin refrigerator provides two cold heads that reach base temperatures of about 350 mK and 250 mK. The cryostat does not have a window and the 4 K working stage is sealed on all sides to mitigate optical power leaks from the 50 K buffer stage.

The temperature of the sub-Kelvin refrigerator can be manipulated by applying power to heaters on its charcoal pumps and gas-gap heat switches. A standard procedure to cool the refrigerator to its base temperature is provided by the manufacturer of the fridge. In addition, I developed and implemented a proportional control algorithm that allowed me to manipulate the temperature of the cold heads between their base temperature and about 800 mK. This control is necessary during TES testing.

I designed two sub-kelvin stages for this cryostat, each cooled by one of the sub-Kelvin refrigerator cold heads. The 350 mK stage is referred to as the intercooler (IC) stage and the 250 mK stage is the ultracooler (UC) stage. The IC stage is made of a U-shaped copper bar suspended above the 4 K stage with thermal isolation supports [55] in order to reduce the thermal loading on the sub-kelvin fridge. The IC stage is also used as a thermal intercept for wiring that is routed between 4 K and the UC stage (i.e. striplines and thermometry wires). The UC stage is

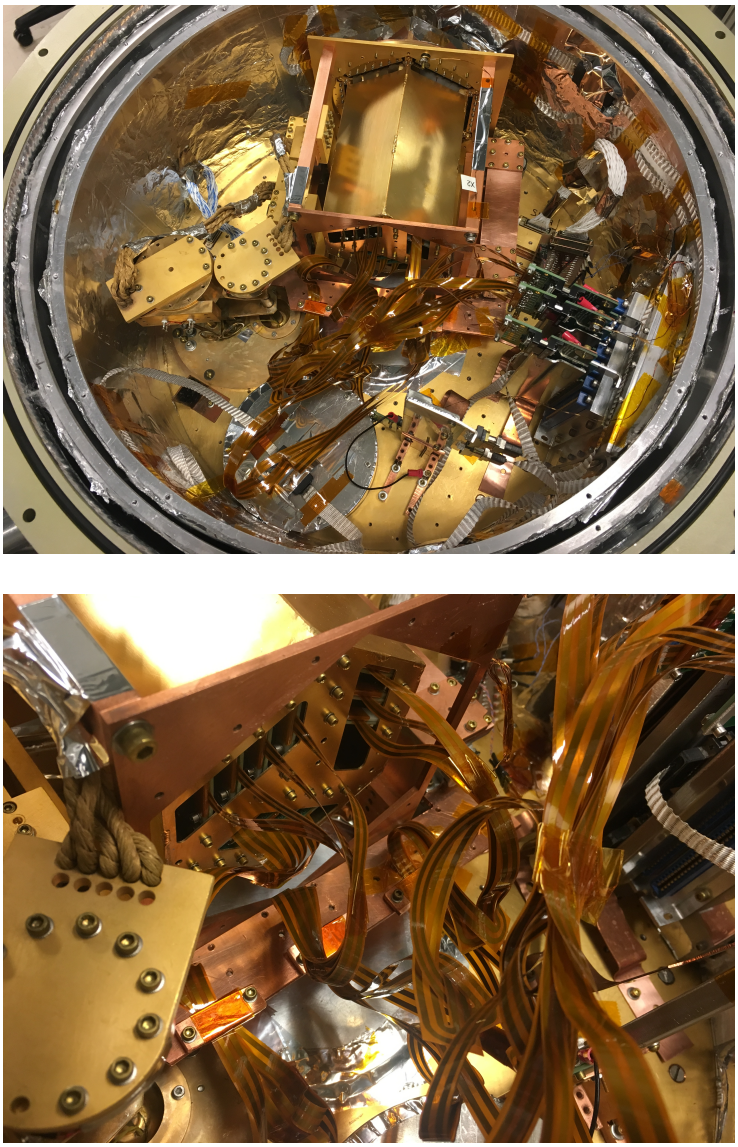

Figure 5.6: A PB-2a wafer is installed in the UCSD test cryostat. *Top:* This is a top-down view of the test cryostat with the PB-2a wafer toward the top of the photo. *Bottom:* The striplines are thermally intercepted at the IC stage in order to reduce the thermal load on the UC stage.

a cubic structure of approximately 30 cm on a side that is used to hold PB-2 TES wafers and the associated sub-kelvin readout electronics. The UC stage is suspended above the IC stage with identical thermal isolation supports. In order to reduce the optical power on the TES wafer, I designed and fabricated a blackened wafer cover that was cooled to 250 mK.

The cryostat is outfitted with multiple wiring harnesses that provide electrical connections between the 300 K shell and the 4 K working area. These wiring harnesses are used to carry the TES bias and readout signals, SQUID biases, thermometry signals, and heater power.

Two photographs of the cryostat are shown in Fig. 5.6.

5.2.3 Measurement Techniques

The suite of measurements used to perform dark characterization of PB-2 wafers is described here.

Network Analysis

The purpose of a network analysis is to determine the resonant frequencies of the cryogenic circuit. These are the frequencies that will be used to bias a comb of detectors. The frequency scatter within an LC chip is small, but still larger than the bandwidth of the resonators, so we must perform this measurement before we are able to bias the detectors. This measurement is usually performed once at the base temperature of the cryostat and once at a temperature above the superconducting temperature of the detectors but below the superconducting temperature of the resonators. The first measurement provides us with the TES bias frequencies and the second with a qualitative look at the normal resistance of the comb of detectors. We assume that the resonant frequencies of the cryogenic circuit don't change over time during a single cooldown. This assumption is confirmed by our ability to successfully operate detectors over months-long cooldowns without the need to change bias frequencies.

A network analysis is done in two parts. First a set of probe tones is driven into the

cryogenic circuit through the carrier path and the resulting voltage across the SQUID is measured. Note that this is performed without any form of SQUID nulling, so the probe tones need to be small enough to not drive the SQUID into nonlinear behavior. Second, a similar measurement is performed, this time with the probe tones injected into the nuller path.

The ratio of the SQUID voltages of the two measurements is independent of the SQUID impedance and is given by the following:

$$\frac{V_{SQUID,car}}{V_{SQUID,nul}} \propto \left| \frac{Z_{bias}}{Z_{bias} + Z_{comb}} \right| \approx \left| \frac{Z_{bias}}{Z_{comb}} \right|, \tag{5.36}$$

where $V_{SQUID,car}$ and $V_{SQUID,nul}$ are the voltage across the SQUID as the result of a current injected through the carrier and nuller path, respectively, and Z_{bias} and Z_{comb} are the impedance of the bias resistor and the impedance of the LC comb, TESs, striplines, and associated stray impedance (defined in Fig. 5.7). This ratio is referred to as a "DAN network analysis" because it mimics the impedance of the circuit when the SQUID is being nulled using DAN. We take the maxima of Eq. 5.36 as the TES bias frequencies. An example of a DAN network analysis measured during a PB-2a dark wafer test is shown in Fig. 5.7.

Detector Biasing

Once we have determined the resonant frequencies, we can bias the combs of detectors. First, the bolometer stage must be heated above the critical temperature of the detectors so that a voltage bias can be applied to them. Next a voltage is applied to the comb at each resonant frequency and DAN is enabled at those same frequencies.

The desired amplitude of the voltage bias applied depends on the measurement that one is planning to perform with the detectors, and is usually one of two extremes. When preparing for an IV curve measurement or to tune the detectors, one needs to apply a large voltage such that Joule heating keeps the detector temperature above T_c as the bolometer stage is cooled. Following

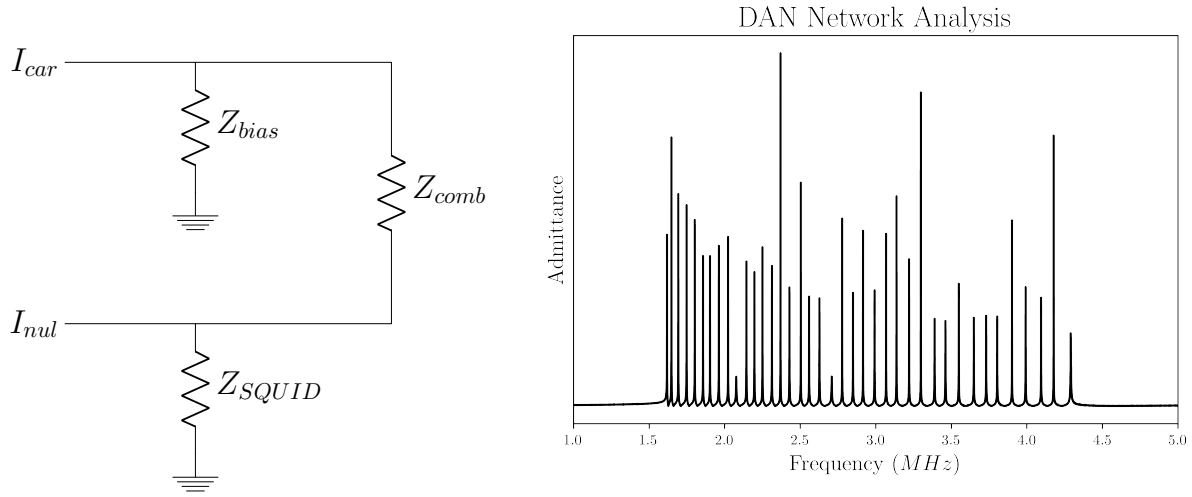

Figure 5.7: *Left*: A schematic of the DfMux cryogenic circuit, simplified to help understand a network analysis. Z_{comb} is the combination of all detetors, LC filters, the cryogenic readout cable, and associated stray impedances. *Right*: An example network analysis with admittance plotted against frequency. Resonances are visible as peaks in addmittance at specific frequencies. The two short peaks at 2.1 and 2.6 MHz are calibration resistors that have higher resistance than the detectors.

this, the bolometer stage is cooled to its base temperature. If, however, one is preparing for an RT measurement, one would apply a small voltage bias, such that the Joule heating does not significantly affect the temperature of the detectors.

IV Curves

An IV curve is a method of probing the transition shape and electrothermal response of a TES. For PB-2 wafer characterization, I used IV curves to measure the detectors' R_n and P_{turn} as well as the parasitic impedance for each channel.

To take an IV curve, one first heats the bolometer stage, biases the TES with a large voltage, and cools the stage, as discussed in Sec. 5.2.3. When the stage has cooled and stabilized at its base temperature, the measurement can begin. The large voltage bias should have kept the detectors heated above T_c. To measure an IV curve, we incrementally decrease the voltage bias on all detectors simultaneously while recording the nulling currents.

As the voltage biases are decreased, the temperatures of the TESs also decrease and the TES cools through its transition. This is evident by a change in the slope of the IV curve. At high voltage, the slope is positive and constant. As the detector starts to transition, the slope approaches zero indicating that the loop gain of the detector is unity. The turnaround power is defined as the power on the TES at this point in the transition. As the detector continues to cool, the slope of the IV curve becomes more and more negative until the detector becomes unstable and falls into its superconducting state. This is evident by a discontinuity in the IV curve followed by an approximately Ohmic, low-resistance curve.

There two notable sources of instability that can cause a TES to latch during an IV curve measurement. The first is the requirement that the electrical bandwidth be at least 5.8 times larger than the TES bandwidth [46]. As the TES transitions, its bandwidth increases and the electrical bandwidth decreases. If the ratio of the two becomes less than about 5.8, the detector will begin to exhibit growing oscillations and fall into its superconducting state. The second cause of instability is that the stray impedance in the bias circuit forms a voltage divider with the TES, weakening the voltage bias. As the TES resistance approaches the Thevenin equivalent series impedance, R_s, the TES transitions from being voltage biased to current biased. A TES with finite loop gain should be stable even with a slight current bias (i.e. even when $R_{TES} < R_s$), but in practice, the PB-2 TESs seems to be limited to the regime $R_{TES} > R_s$.

Detector Tuning

Detector tuning is the operation of putting the detectors into a responsive state. This is done before most optical testing (and before observing the CMB). To tune the combs of detectors, one needs to first bias the combs and then cool the bolometer stage in the same way that one would in preparation for an IV curve measurement. After the stage has reached its base temperature, the voltage biases are incrementally decreased until the desired tuning point has been reached. The

tuning point is usually parameterized by the fractional resistance

$$R_{frac} = (R + R_s)/(R_n + R_s). \tag{5.37}$$

A typical tuning point is R_{frac} = 0.7-0.8.

RT

In order to measure the detectors' critical temperature and normal resistance, I performed measurements of the resistance of the detectors as a function of temperature. To do this measurement, one needs to first heat the bolometer stage and bias the combs of detectors with a small voltage. This bias voltage is intended to provide a probe of the TES resistance without applying a significant amount of Joule power.

After the bias has been applied, the bolometer stage temperature is manipulated while its temperature is recorded with a thermometer and while the nulling currents are recorded. It is important that the temperature of the bolometer stage does not change very quickly in order for the measured temperature to be indicative of the TES temperature. One can check for this effect by measuring an R(T) curve twice, once with the bolometer stage temperature decreasing and once with the temperature increasing. If the temperature change is too fast, the transitions for a single detector will be shifted relative to each other.

5.2.4 Detector Parameter Measurements

Wafer PB20.08.03

In December 2016 through January 2017, candidate PB-2a wafer PB20.08.03 was characterized by the author using the dark test cryostat. The wafer was outfitted with a full set of deployment PB-2a LC boards, striplines, and adapter boards. This was the first time a PB-2 wafer had been characterized with the full set of readout installed. The base temperature reached during

this cooldown was 270 mK. After measuring IV curves and R(T) curves for this wafer, it was deemed unacceptable for observation due to high and variable normal resistance, highly variable turnaround power, and highly variable superconducting transition shapes.

RT curves from one multiplexed set of detectors are shown in Fig. 5.8. The width of the superconducting transition is highly variable. The slope of the transition is directly related to the strength of electrothermal feedback, so we require uniform transition shapes. The low-temperature resistance is assumed to be caused by a stray series resistance, as described in Sec. 5.1.1.

IV curves along with derived RV,and RP curves for one comb of detectors on this wafer are shown in Fig. 5.9. It is clear from these plots that the normal resistance and turn around power is highly variable.

Analysis of the RT and IV measurements indicate that the normal resistance values are high and bimodal and that the turnaround power values are highly variable. These conclusions are true both before and after the stray series resistance calibration was applied. The critical temperatures are 440 ± 10 mK. No correlation was found between critical temperature and turnaround, indicating that the variability in turnaround power was not caused by variability in critical temperature. There was also no correlation between normal resistance and turnaround power. Normally, we would not expect these values to be correlated, but this is an odd situation in which the normal resistance distribution is bimodal. The only other parameter that is expected to be bimodal is the turnaround power, so it is interesting to note that they do not seem to be correlated. The results of these analyses are shown in Fig. 5.10.

Wafer PB20.13.10

Candidate PB-2a wafer PB20.13.10 was characterized by the author in the UCSD test cryostat in December 2017-January 2018. This wafer was deemed acceptable for observations and was deployed with the PB-2a receiver.

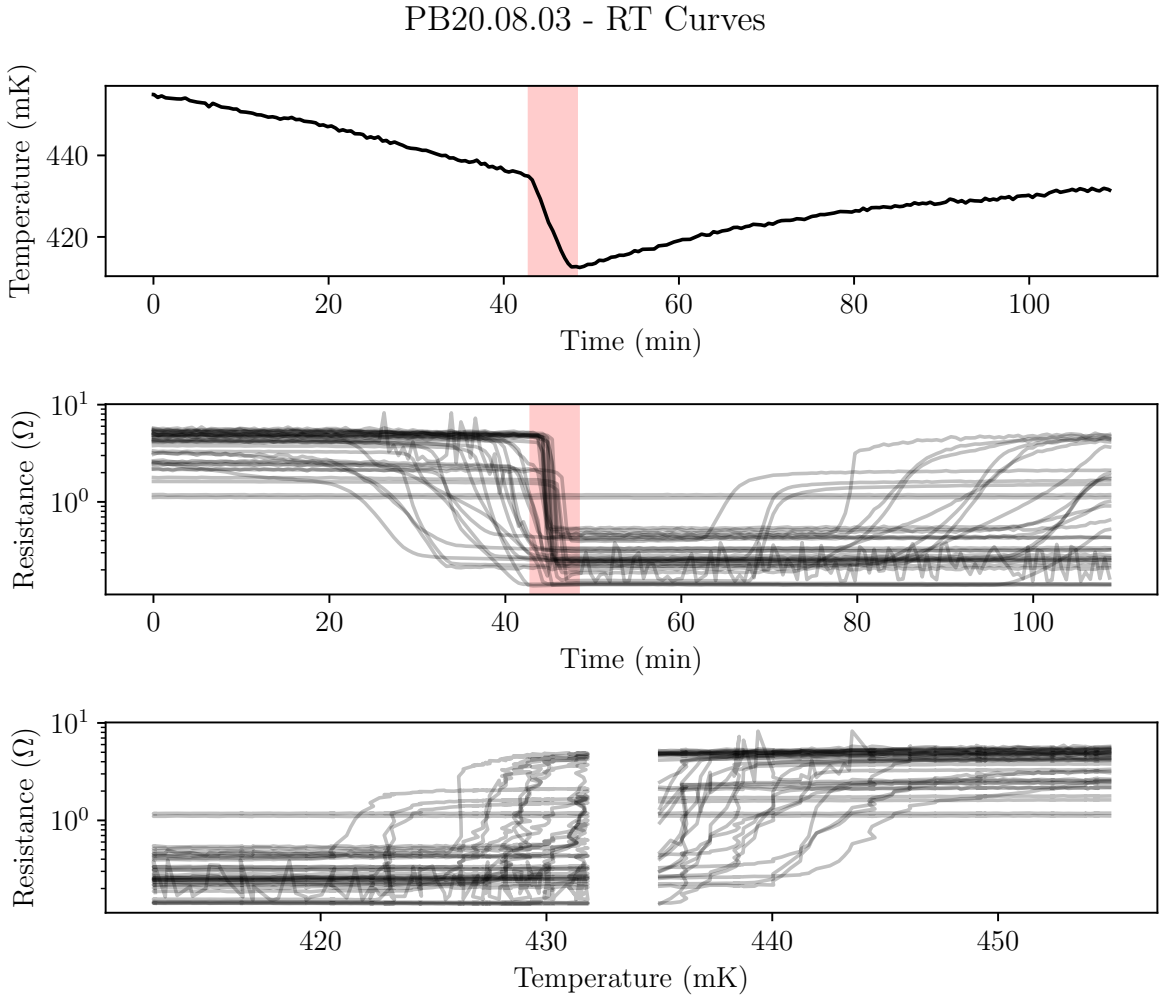

Figure 5.8: Data from an RT measurement of one multiplexed set of detectors from wafer PB20.08.03 are shown. *Top:* The temperature of the bolometer stage is plotted as a function of time. The red region was cut from analysis due to the rapid change in temperature. *Middle:* The resistance of a multiplexed set of detectors is plotted as a function of time. The red region corresponds to the same data cut. *Bottom:* The resistance of a set of multiplexed detectors is plotted as a function of the temperature of the bolometer stage. Data between 432-435 mK was cut for aforementioned reasons. The two detectors that appear to have constant resistance of about 1 Ω are actually non-superconducting calibration resistors. All of the detectors have a superconducting transition and there is high variability in the width of the transition and the transition temperature. Additionally, there is a residual resistance below the superconducting transition.

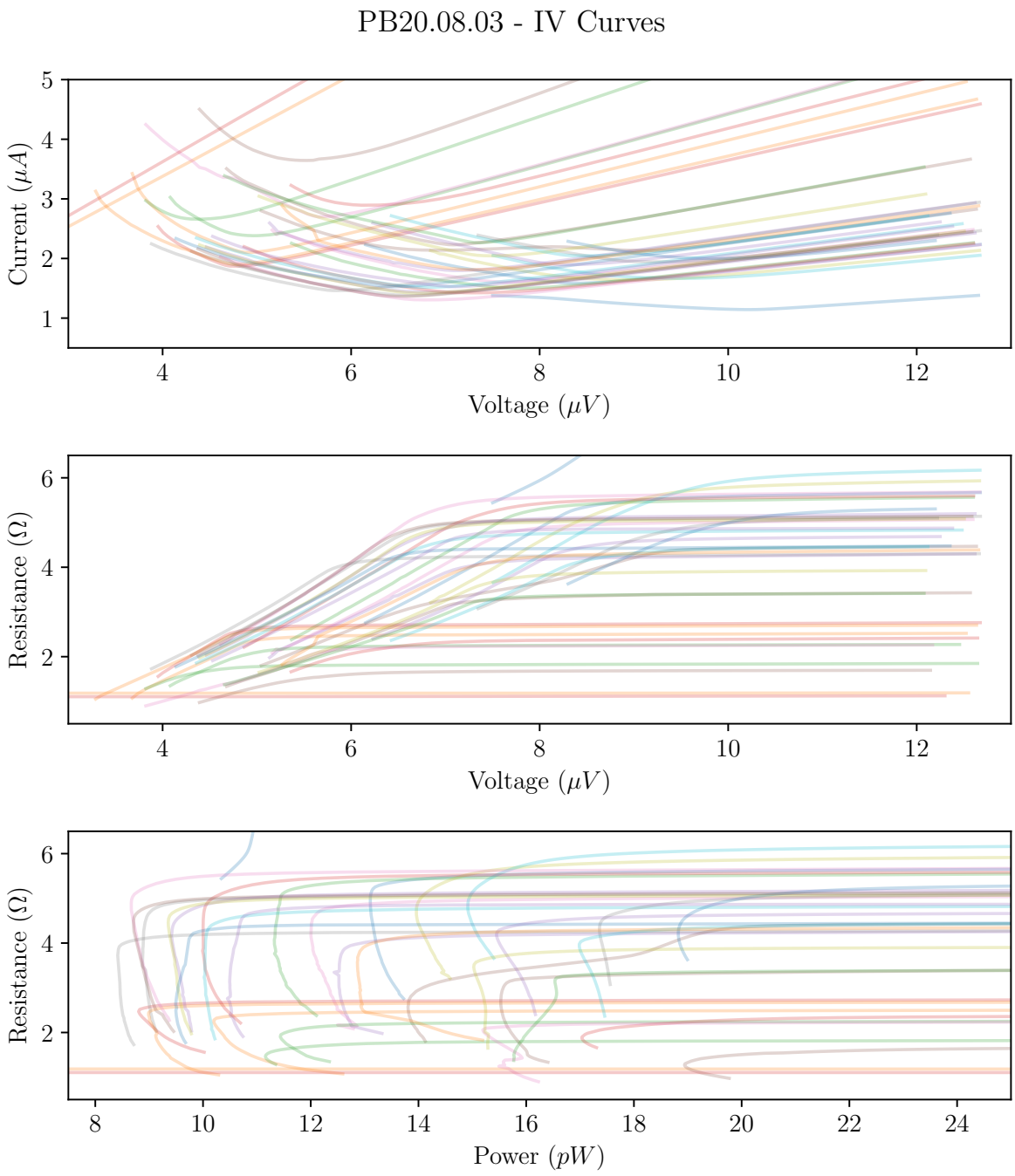

Figure 5.9: Data from an IV measurement of one multiplexed set of detectors from wafer PB20.08.03 are shown. All voltage and current values shown are RMS. The plots shown are: *top*, IV curves; *middle*, RV curves; *bottom*, RP curves. The two detectors in each plot that appear to have a constant resistance of about 1 Ω are actually non-superconducting calibration resistors.

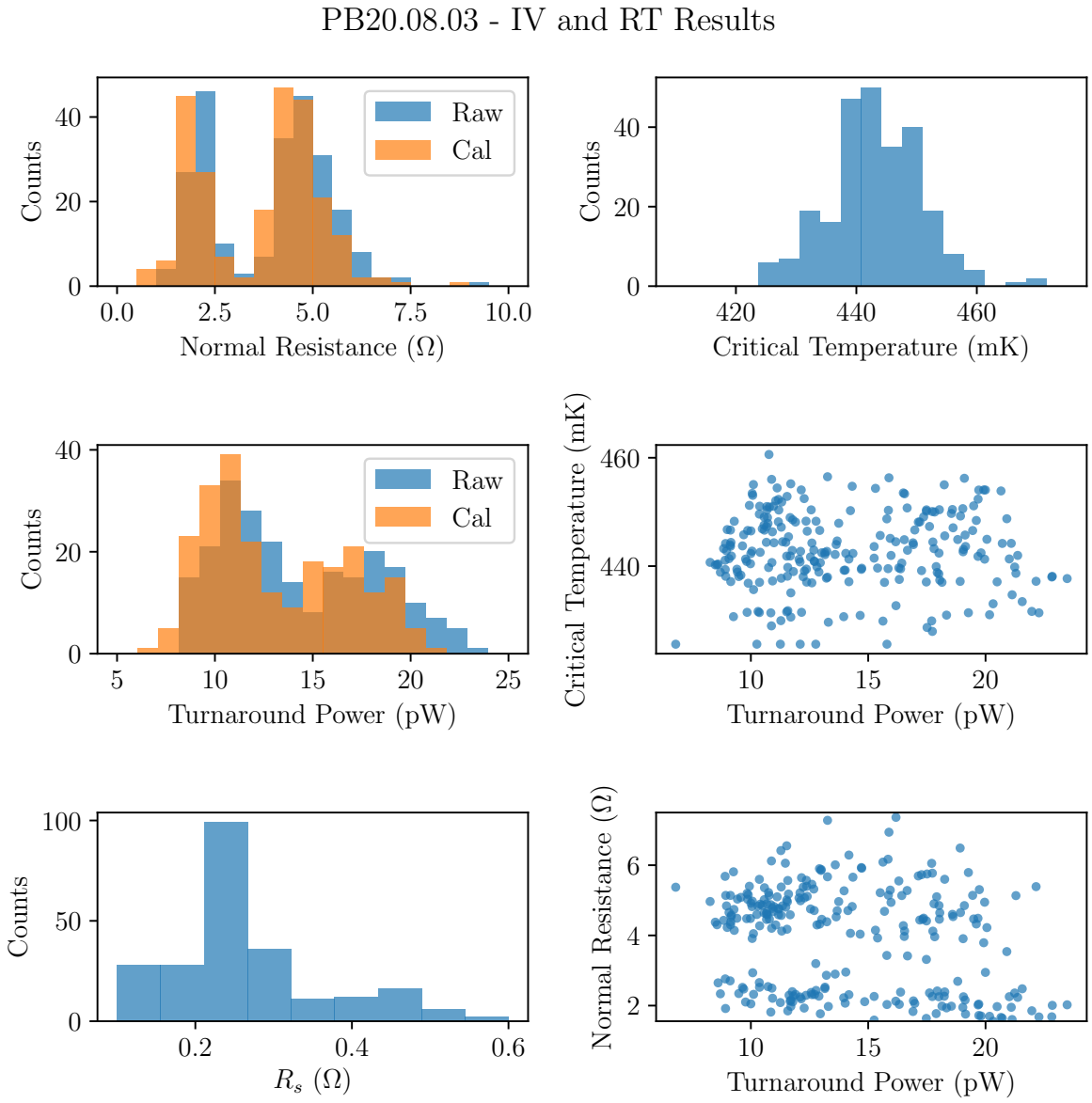

Figure 5.10: Analysis of RT and IV curves from wafer PB20.08.03 are shown. *Top left*: Histograms of the detector normal resistances both before calibration for stray resistance ("Raw") and after ("Cal"). *Middle left*: Histograms of the detector turnaround powers both before calibration for stray resistance ("Raw") and after ("Cal"). *Bottom left*: A histogram of the stray series resistance values measured. *Top right*: A histogram of the detector critical temperature values. *Middle right*: A scatter plot of critical temperature and turnaround power. No correlation is apparent. *Bottom right*: A scatter plot of normal resistance and turnaround power. No correlation is apparent.

Table 5.2: TES parameters measured for wafers in Run 18b. All values shown here have been calibrated for R_s and L_{bias} and represent my best estimate of the actual TES values.

Wafer	R_n (Ω)	P_{turn} (pW)		Pass/Fail
		90 GHz	150 GHz	
PB20.13.27	1.02 ± 0.05	8 ± 1	19 ± 1	Pass
PB20.13.33	1.03 ± 0.07	9 ± 1	22 ± 2	Pass
PB20.13.35	1.0 ± 0.2	10 ± 2	22 ± 3	Pass
PB20.13.36	0.9 ± 0.1	10 ± 1	23 ± 2	Pass
PB20.13.39	1.05 ± 0.06	9 ± 1	21 ± 2	Pass
PB20.13.43	1.0 ± 0.1	8 ± 2	17 ± 5	Fail
PB20.13.44	1.02 ± 0.08	12 ± 1	28 ± 3	Fail

IV, RV, and RP curves from a comb of detectors on this wafer are shown in Fig. 5.11. The resistance at low voltage was taken to be caused by a stray series resistance, R_s. The measured values of R_s for each detector were used to calibrate the results of the IV measurement, as described in Sec. 5.1.1. Histograms of raw and calibrated detector parameters and stray resistance values are shown in Fig. 5.11. The results of the measurement and calibration are: $R_n = 1.3 \pm 0.2$ Ω, 90 GHz $P_{turn} = 10 \pm 1$ pW, and 150 GHz $P_{turn} = 21 \pm 2$ pW. These values are within our specifications. The 90 GHz P_{turn} value is slightly higher than the 90 GHz P_{sat} target, but as discussed in Sec. 5.2.1, P_{sat} is typically 5-10% smaller than P_{turn} so we expect that P_{sat} is within our target range.

Run 18b Wafers

Run 18b was the final commissioning cooldown of the PB-2b receiver in the lab at UCSD before its deployment to Chile. The dark detector characterization performed by the author during this cooldown is described here.

IV curves were measured with all seven wafers in PB-2b. Four wafers (PB20.13.35,

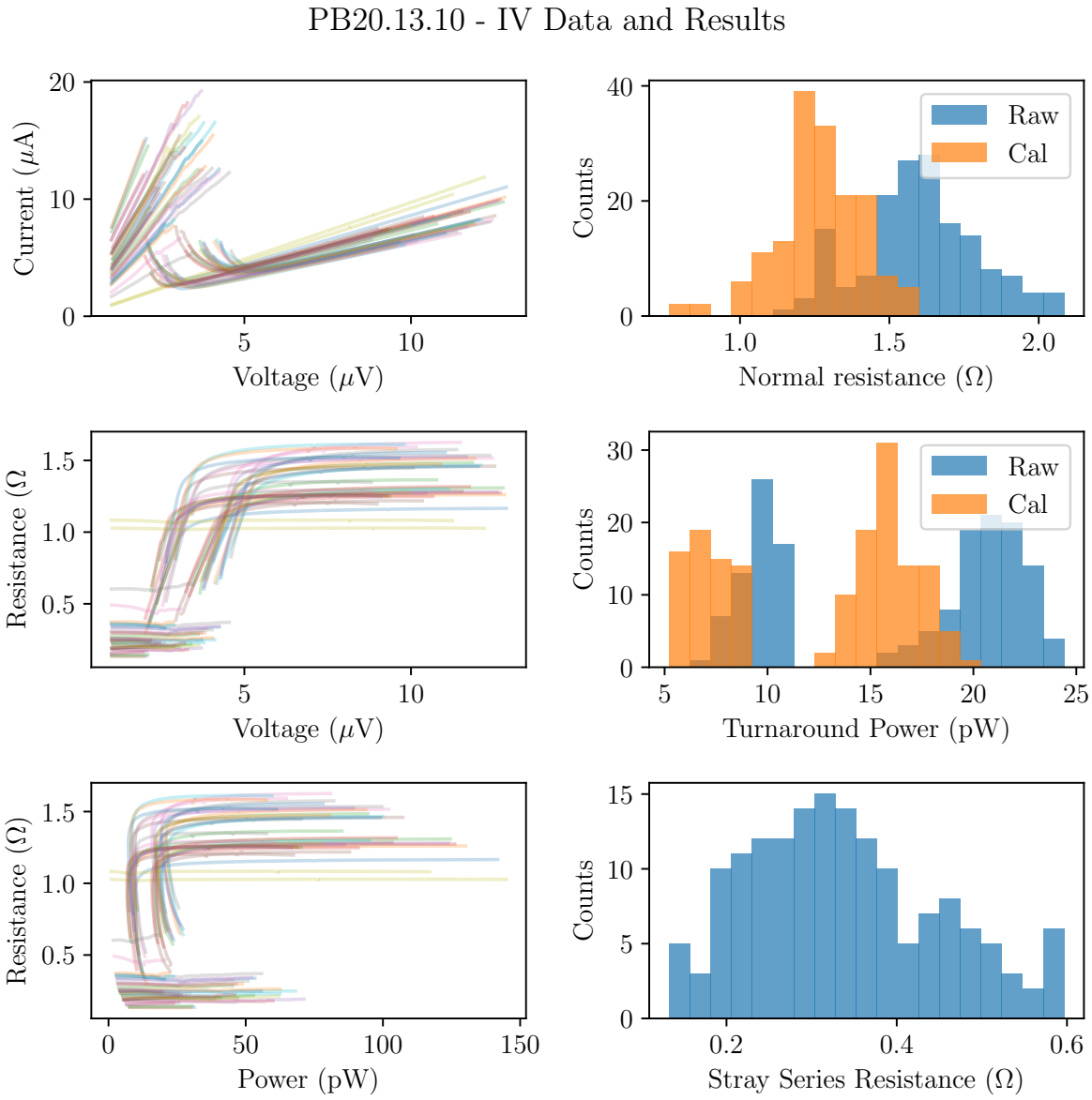

Figure 5.11: IV data and analysis from wafer PB20.13.10 are shown. All voltage and current values shown are RMS. *Left column*: IV curves, RV curves, and RP curves, respectively, for one multiplexed set of detectors. The two detectors in each plot that appear to have a constant resistance of about 1 Ω are actually non-superconducting calibration resistors. *Top right*: A histogram of the normal resistance values, both uncalibrated ("Raw") and calibrated for a stray series resistance ("Cal"). *Top middle*: A histogram of the turnaround power values, both uncalibrated ("Raw") and calibrated for a stray series resistance ("Cal"). *Bottom right*: A histogram of the stray series resistance values.

PB20.13.36, PB20.13.43, PB20.13.44) had sub-kelvin covers on them to reduce the optical power incident on the detectors. The other three wafers (PB20.13.27, PB20.13.33, PB20.13.39) had neutral density filters (NDFs) in front of them to reduce the optical load but allow for optical characterization. The NDFs are so strongly attenuating that these three wafers have negligible incident optical power during these measurements. The base temperature of the bolometer stage during this run was 250 mK. Five of the seven wafers have measured dark parameters that meet our target detector parameters and will be deployed with PB-2b.

IV curves along with derived RV and RP curves are shown in Figs. 5.12-5.18. The residual resistance at low voltage (i.e. when the detectors were superconducting) was assumed to be caused by a stray series resistance, R_s. The measured values of R_s for each detector were used to calibrate the results of the IV measurement, as described in Sec. 5.1.1.

After calibrating for R_s, the detectors' normal resistances showed a strong correlation with bias frequency. This correlation is not expected to be caused by an actual variation in detector resistances and was assumed to be caused by a stray bias inductance, L_{bias}. L_{bias} was measured by asserting that the normal resistance values for detectors on a given wafer were normally distributed about a mean value, $R_{n,mean}$, and that the apparent correlation with bias frequency was due completely to L_{bias}. Under this assertion, we expect to measure a normal resistance $R_{n,measured}$ that varies with bias frequency:

$$R_{n,measured} = R_{n,mean} \frac{R_b}{\sqrt{(R_b)^2 + (2\pi f_{bias} L_b)^2}}. \tag{5.38}$$

We fit the model to our data in order to retrieve $R_{n,mean}$ and L_{bias}. For each detector wafer, we fit for a single value of $R_{n,mean}$ and up to thirty values of L_{bias} (one for each multiplexed set of detectors). The $R_{n,mean}$ value is not used for calibrating data. The best-fit values of L_{bias} are used to calibrate the raw data as described in Sec. 5.1.1. The results of this calibration are shown for a single multiplexed set of detectors in Fig. 5.19 and for entire detector wafers in Figs. 5.12-5.18.

The typical stray bias inductance value is 1.1 nH, which has a significant contribution to the total impedance of the bias element, Z_{bias}:

$$|Z_{bias}| = \sqrt{R_{bias}^2 + (2\pi i f_{bias} L_{bias})^2} \tag{5.39}$$

$$= \sqrt{(0.030\ \text{m}\Omega)^2 + \left[6.5\text{m}\Omega\left(\frac{f_{bias}}{1\ \text{MHz}}\right)\left(\frac{L_{bias}}{1.1\ \text{nH}}\right)\right]^2} \tag{5.40}$$

For a typical value of $L_{bias} = 1.1$ nH, the ratio of $|Z_{bias}|$ to R_{bias} is 1.1-1.4 across the readout bandwidth of 1.5-4.5 MHz.

5.2.5 Effects of Stray Impedance on Small-Signal Response

The expected small-signal behavior of a TES with a series stray resistance under constant optical power was derived in Sec. 5.1.2. In this section, we will compare to data measured in the PB-2b receiver during dark detector characterization.

Note that the measurements described in this section were performed with negligible optical power. Because the loop gain depends on the electrical bias power on the detector, we should expect the loop gain to decrease by a factor of about half when these detectors are observing in Chile.

The slope of an IV curve for a single PB-2b detector is plotted as a function of the total measured resistance, $R_{tot} \equiv R_0 + R_s$, in Fig. 5.20. Consider first the case where the stray series resistance is negligible and the TES resistance, R_0, is equal to R_{tot}. The slope of the IV curve in the high loop gain limit is calculated by using Eq. 5.33 and setting $R_s = 0$ and $\mathcal{L} >> 1$. The slope is given by $-1/R_0$. The curve of $\mathcal{L} = -1/R_0$ is shown in Fig. 5.20. The data do not respect this bound, implying that this is not the correct model to describe these data.

Next consider the case in which the stray series resistance is nonzero. In this case, the high loop gain limit is defined by $\mathcal{L} >> (R_0 + R_s)/(R_0 - R_s)$. The slope of the IV curve under these conditions is given by $-(R_{tot} - 2R_s)^{-1}$. The curve of $\mathcal{L} = -(R_{tot} - 2R_s)^{-1}$ is also shown

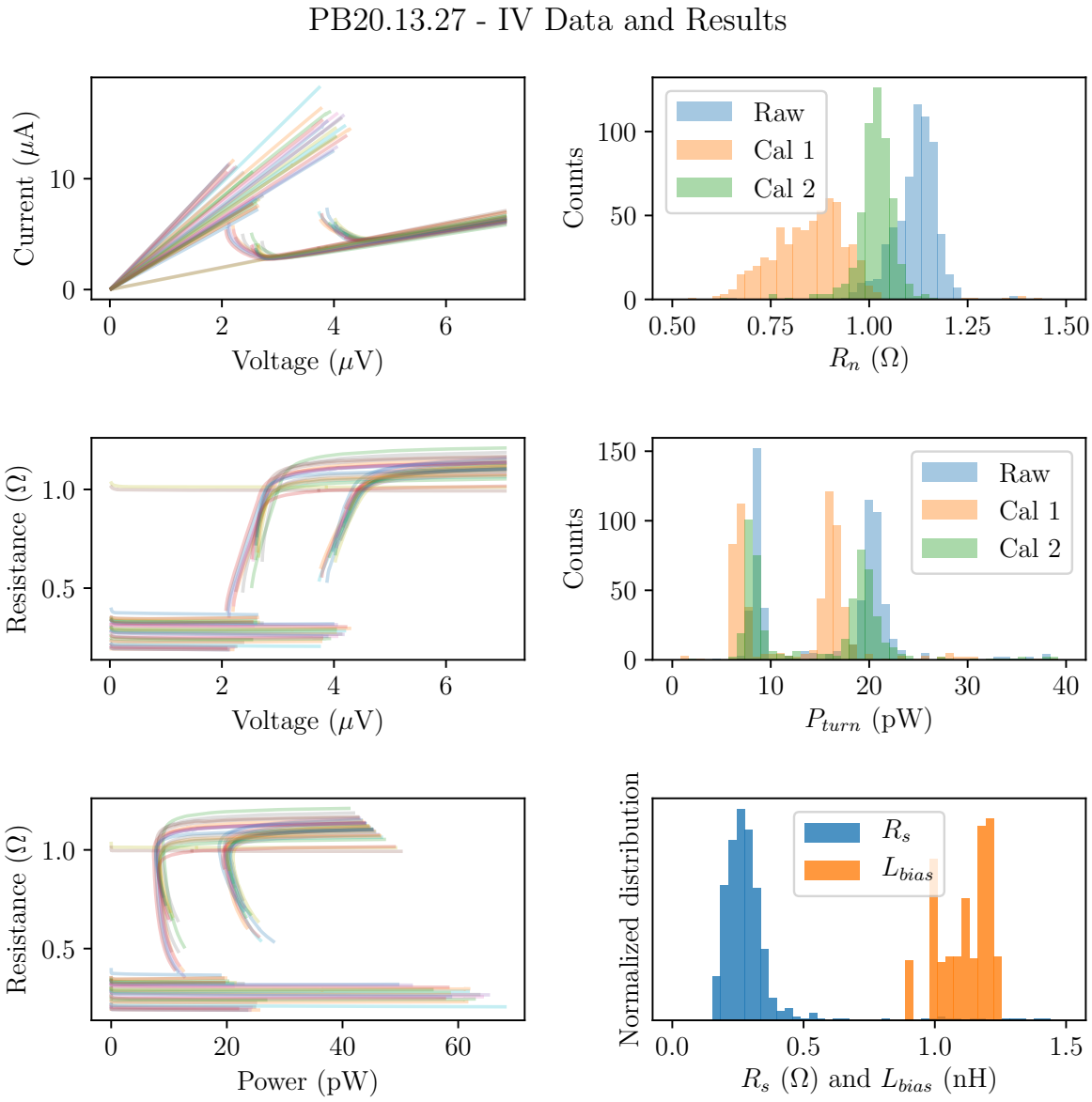

Figure 5.12: IV data and analysis from wafer PB20.13.27 are shown. *Left column*: IV curves, RV curves, and RP curves, respectively, for one multiplexed set of detectors. All voltage and current values shown are RMS. The two detectors in each plot that appear to have a constant resistance of about 1 Ω are actually non-superconducting calibration resistors. *Top right and middle right*: Histogram of the normal resistance and turnaround power values: uncalibrated ("Raw"), calibrated for a stray series resistance ("Cal 1"), and calibrated for a stray series resistance and stray bias inductance ("Cal 2"). *Bottom right*: A histogram of the measured stray series resistance and bias inductance values.

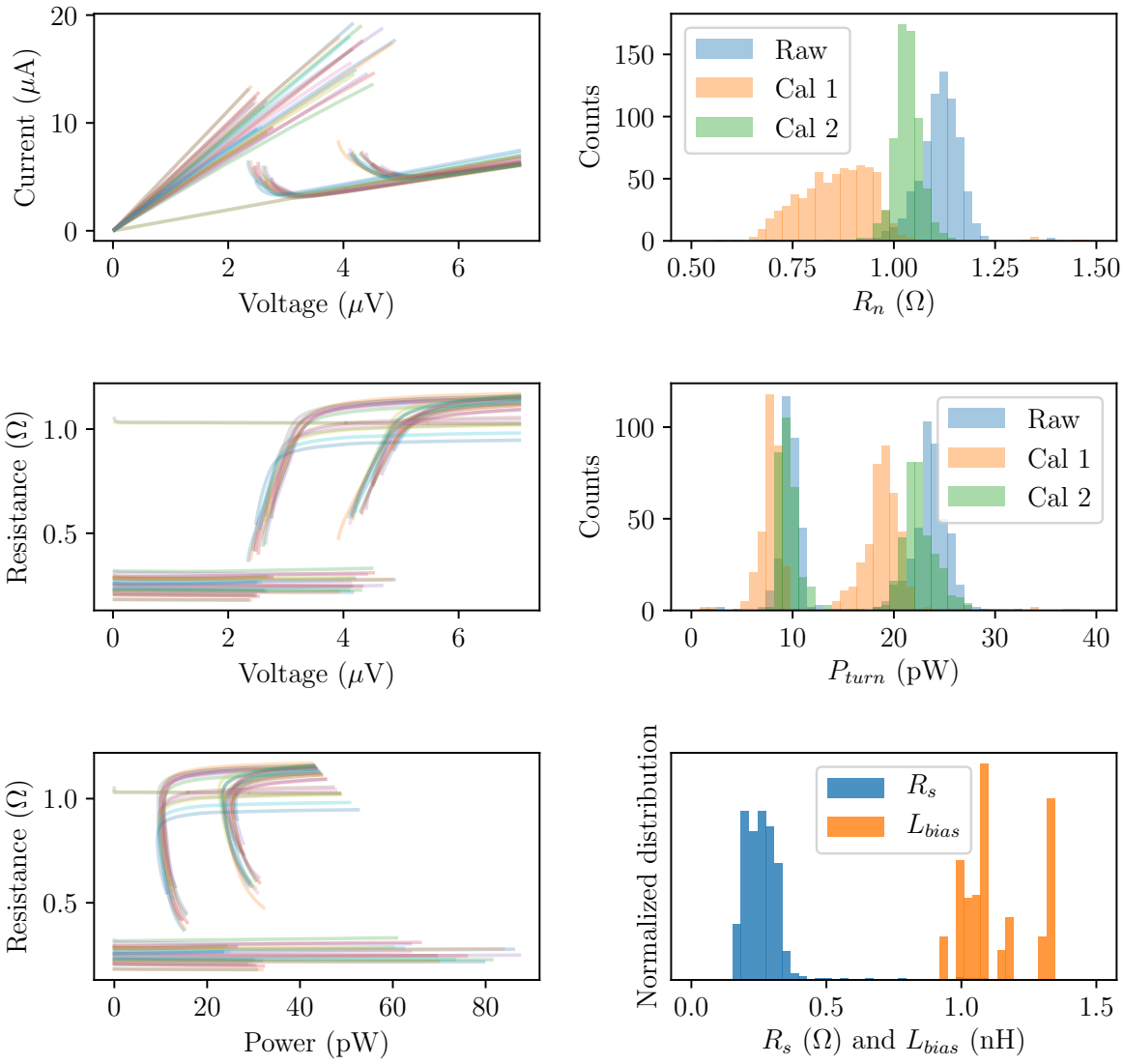

Figure 5.13: IV data and analysis from wafer PB20.13.33 are shown. *Left column*: IV curves, RV curves, and RP curves, respectively, for one multiplexed set of detectors. All voltage and current values shown are RMS. The two detectors in each plot that appear to have a constant resistance of about 1 Ω are actually non-superconducting calibration resistors. *Top right and middle right*: Histogram of the normal resistance and turnaround power values: uncalibrated ("Raw"), calibrated for a stray series resistance ("Cal 1"), and calibrated for a stray series resistance and stray bias inductance ("Cal 2"). *Bottom right*: A histogram of the measured stray series resistance and bias inductance values.

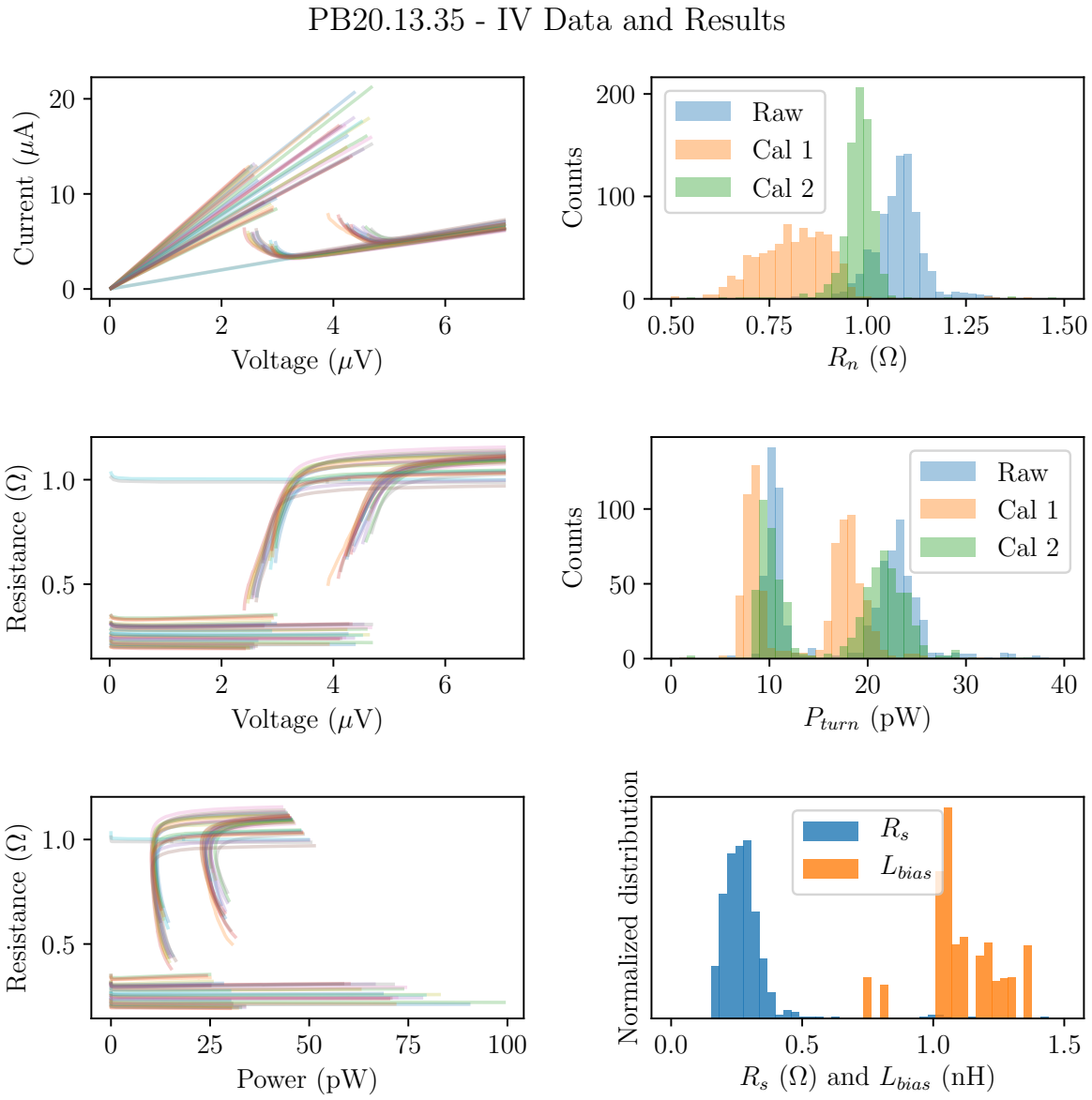

Figure 5.14: IV data and analysis from wafer PB20.13.35 are shown. *Left column*: IV curves, RV curves, and RP curves, respectively, for one multiplexed set of detectors. All voltage and current values shown are RMS. The two detectors in each plot that appear to have a constant resistance of about 1 Ω are actually non-superconducting calibration resistors. *Top right and middle right*: Histogram of the normal resistance and turnaround power values: uncalibrated ("Raw"), calibrated for a stray series resistance ("Cal 1"), and calibrated for a stray series resistance and stray bias inductance ("Cal 2"). *Bottom right*: A histogram of the measured stray series resistance and bias inductance values.

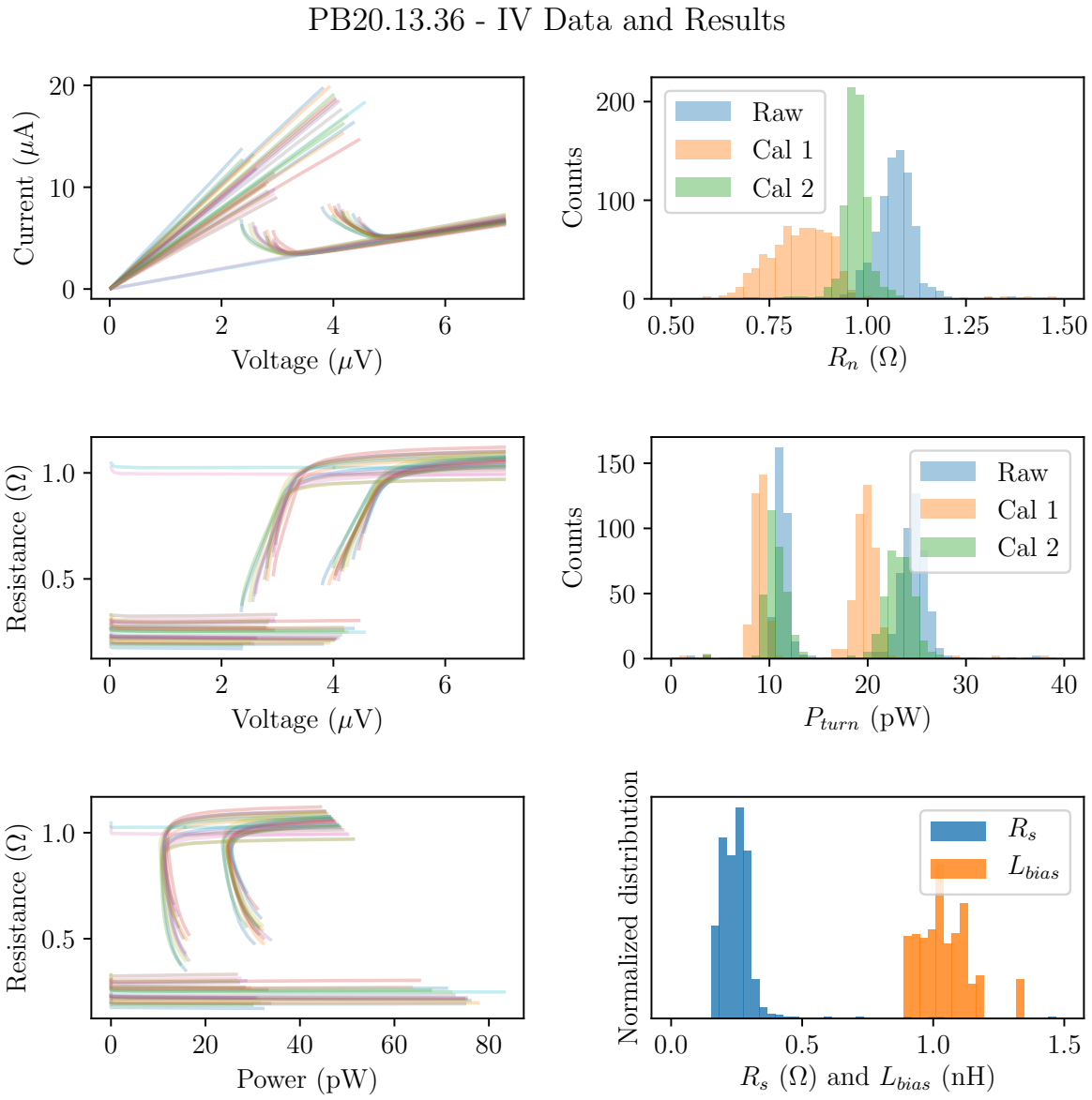

Figure 5.15: IV data and analysis from wafer PB20.13.36 are shown. *Left column*: IV curves, RV curves, and RP curves, respectively, for one multiplexed set of detectors. All voltage and current values shown are RMS. The two detectors in each plot that appear to have a constant resistance of about 1 Ω are actually non-superconducting calibration resistors. *Top right and middle right*: Histogram of the normal resistance and turnaround power values: uncalibrated ("Raw"), calibrated for a stray series resistance ("Cal 1"), and calibrated for a stray series resistance and stray bias inductance ("Cal 2"). *Bottom right*: A histogram of the measured stray series resistance and bias inductance values.

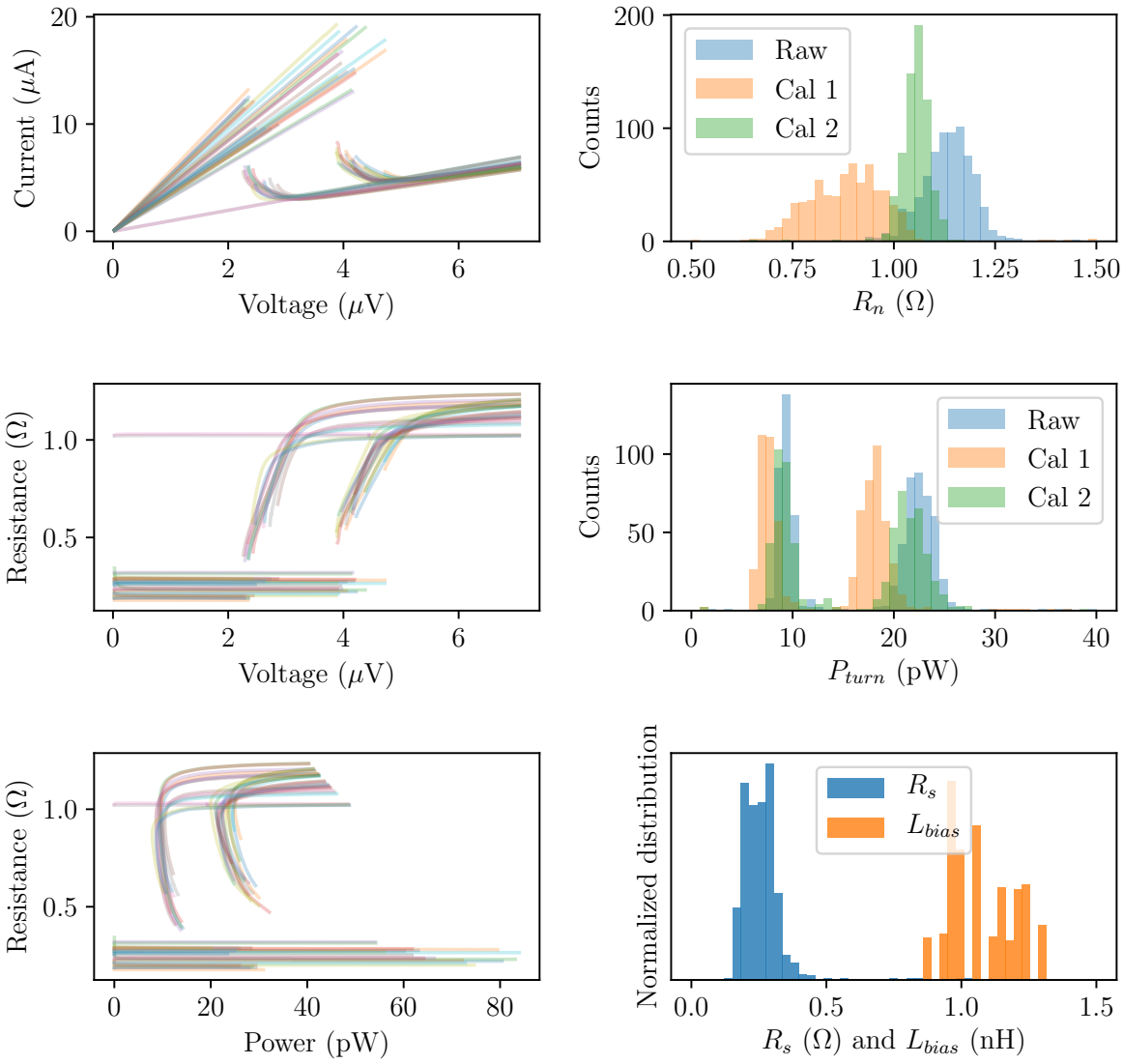

Figure 5.16: IV data and analysis from wafer PB20.13.39 are shown. *Left column*: IV curves, RV curves, and RP curves, respectively, for one multiplexed set of detectors. All voltage and current values shown are RMS. The two detectors in each plot that appear to have a constant resistance of about 1 Ω are actually non-superconducting calibration resistors. *Top right and middle right*: Histogram of the normal resistance and turnaround power values: uncalibrated ("Raw"), calibrated for a stray series resistance ("Cal 1"), and calibrated for a stray series resistance and stray bias inductance ("Cal 2"). *Bottom right*: A histogram of the measured stray series resistance and bias inductance values.

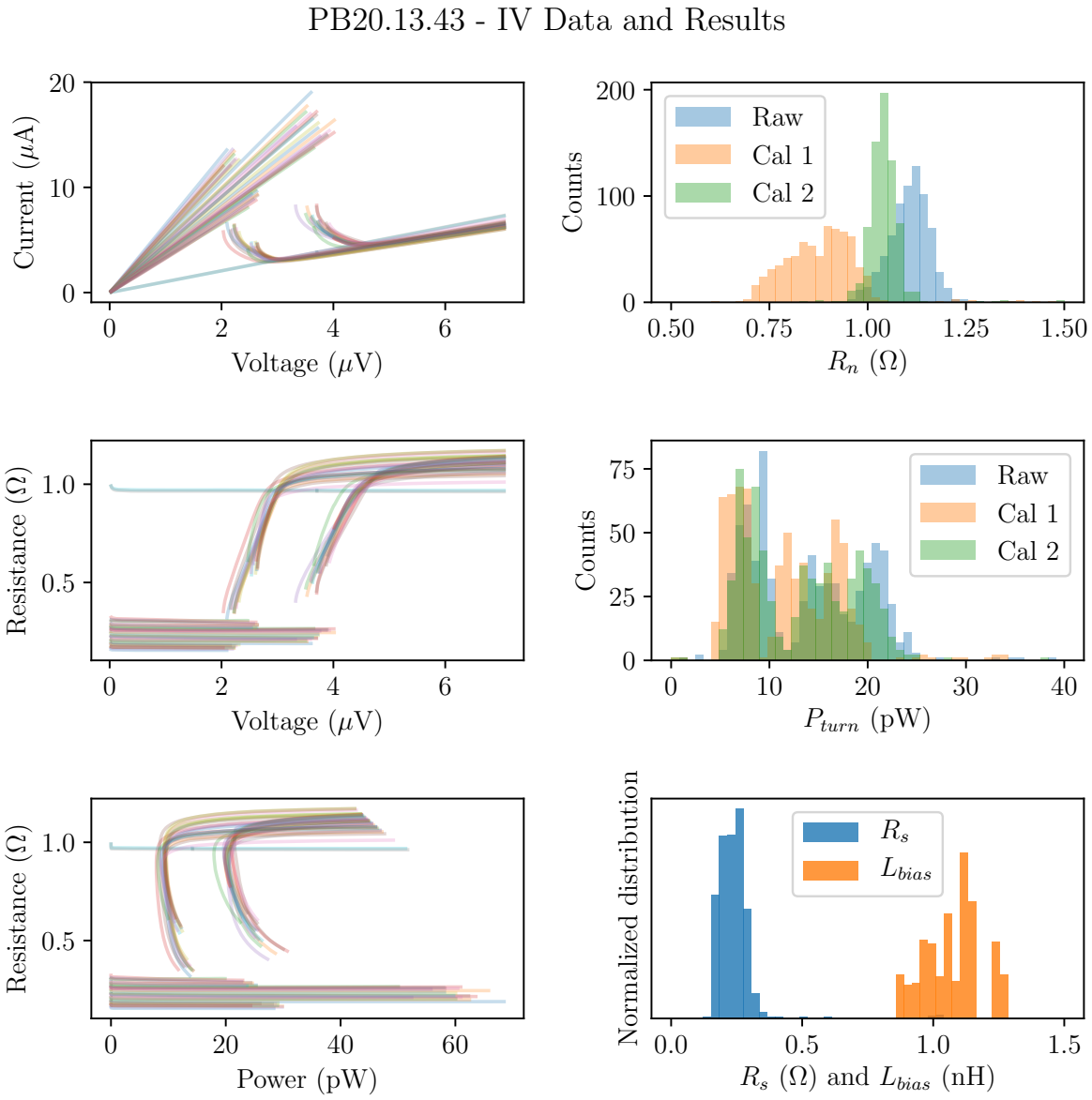

Figure 5.17: IV data and analysis from wafer PB20.13.43 are shown. *Left column*: IV curves, RV curves, and RP curves, respectively, for one multiplexed set of detectors. All voltage and current values shown are RMS. The two detectors in each plot that appear to have a constant resistance of about 1 Ω are actually non-superconducting calibration resistors. *Top right and middle right*: Histogram of the normal resistance and turnaround power values: uncalibrated ("Raw"), calibrated for a stray series resistance ("Cal 1"), and calibrated for a stray series resistance and stray bias inductance ("Cal 2"). *Bottom right*: A histogram of the measured stray series resistance and bias inductance values.

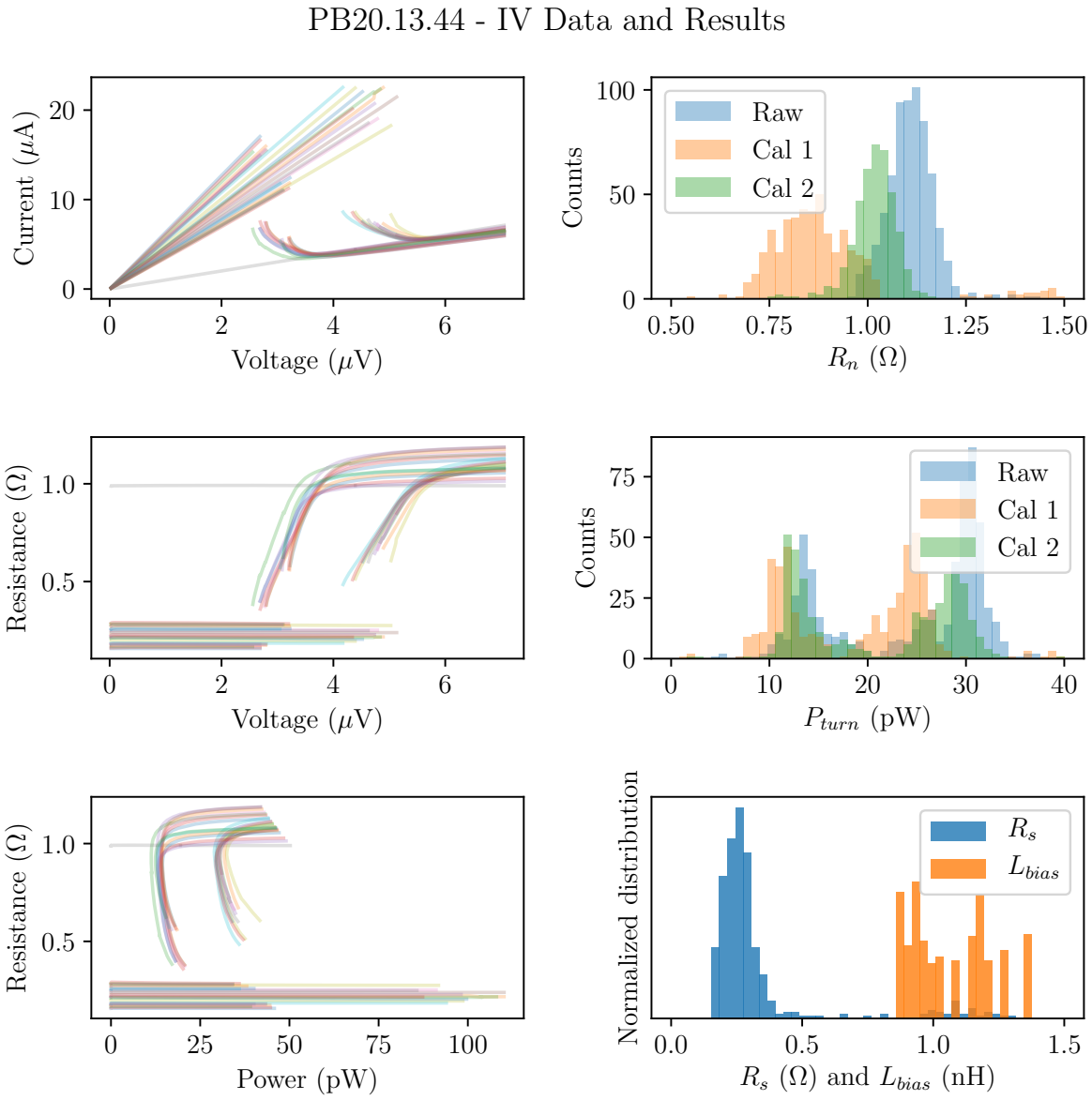

Figure 5.18: IV data and analysis from wafer PB20.13.44 are shown. *Left column*: IV curves, RV curves, and RP curves, respectively, for one multiplexed set of detectors. All voltage and current values shown are RMS. The two detectors in each plot that appear to have a constant resistance of about 1 Ω are actually non-superconducting calibration resistors. *Top right and middle right*: Histogram of the normal resistance and turnaround power values: uncalibrated ("Raw"), calibrated for a stray series resistance ("Cal 1"), and calibrated for a stray series resistance and stray bias inductance ("Cal 2"). *Bottom right*: A histogram of the measured stray series resistance and bias inductance values.

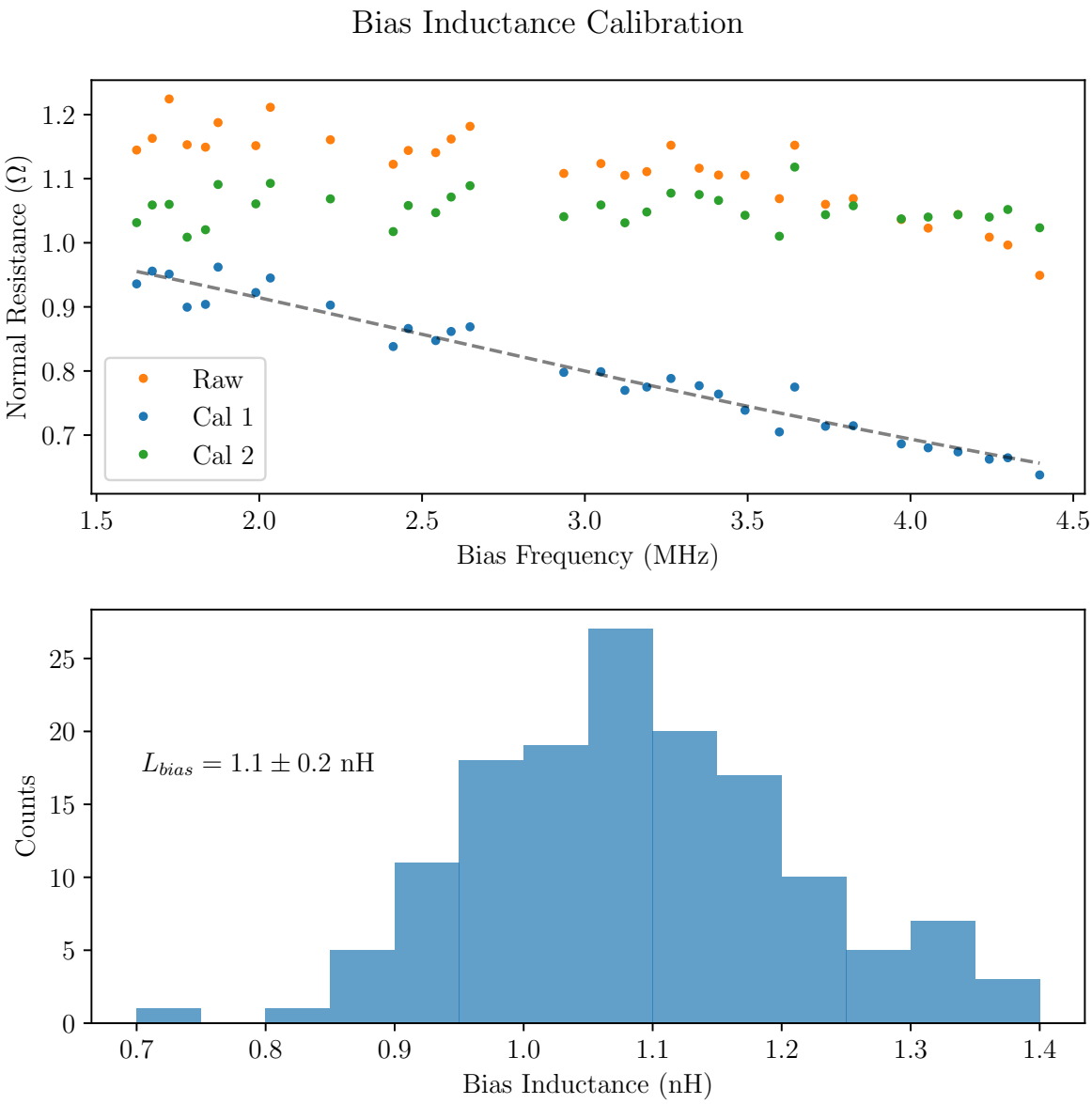

Figure 5.19: Stray bias inductance calibrations. *Top:* The normal resistance values of one multiplexed set of detectors is plotted against bias frequency. The data labeled "Raw" have no calibration applied to account for stray impedance. The "Cal 1" data are calibrated for a stray series resistance and show a strong trend with bias frequency. The dashed line is the best-fit model of Eq. 5.38 with fit parameters $L_{bias} = 1.4$ nH and $R_{n,mean} = 1.1$ Ω. The "Cal 2" data are calibrated for both the stray series resistance and the stray bias inductance. The "Cal 2" data no longer exhibit a trend with bias frequency. *Bottom:* A histogram of 144 L_{bias} values measured on five separate TES wafers is shown. The mean value is 1.1 nH and the standard deviation is 0.2 nH.

in Fig. 5.20 and the data do respect this bound. The data do not contradict this prediction of the stray impedance model.

Additionally, the loop gain can be obtained from an IV curve using Eq. 5.35. The loopgain for a single detector is plotted in Fig. 5.20 as a function of R_{tot} for a few values of R_s. The loop gain has a strong dependence on R_s, even in the small range shown. Assuming $R_s = 0$ causes the loop gain to diverge (not shown).

Also shown in Fig. 5.20 is the curve $\mathcal{L} = 10(R_0 + R_s)/(R_0 - R_s)$. The TES is in the high loop gain limit when its loop gain is substantially above this curve and also much greater than unity. In the range R_{tot}=0.6-0.8 Ω, the measured loop gain is above this curve and the detector is operating in the high loop gain limit.

5.3 Optical Detector Characterization

The goal of the optical characterization described here is to understand how the TES responsivity changes as a function of detector tuning and drive frequency.

In the two responsivity models discussed so far, there is one independent variable to describe the frequency of the drivings signal (ω) and up to four independent variables to describe the TES and bias circuit ($\mathcal{L}$, V_0, R_0, R_s). This picture is simplified when considering a single, specific detector in a specific optical configuration (i.e. a specific value of steady-state optical power, $P_{opt,0}$). The reasons for this are: R_s becomes a parameter rather than an independent variable, and $\mathcal{L}$, V_0, and R_0 are all functions of the detector tuning point. We can express the responsivity as a function of two independent variables, ω and R_{frac}, and a single parameter, R_s:

$$S_I = S_I(R_{frac}, \omega; R_s) \tag{5.41}$$

The measurements described in this section were performed with negligible optical power. Because the loop gain depends on the electrical bias power on the detector, we should expect the

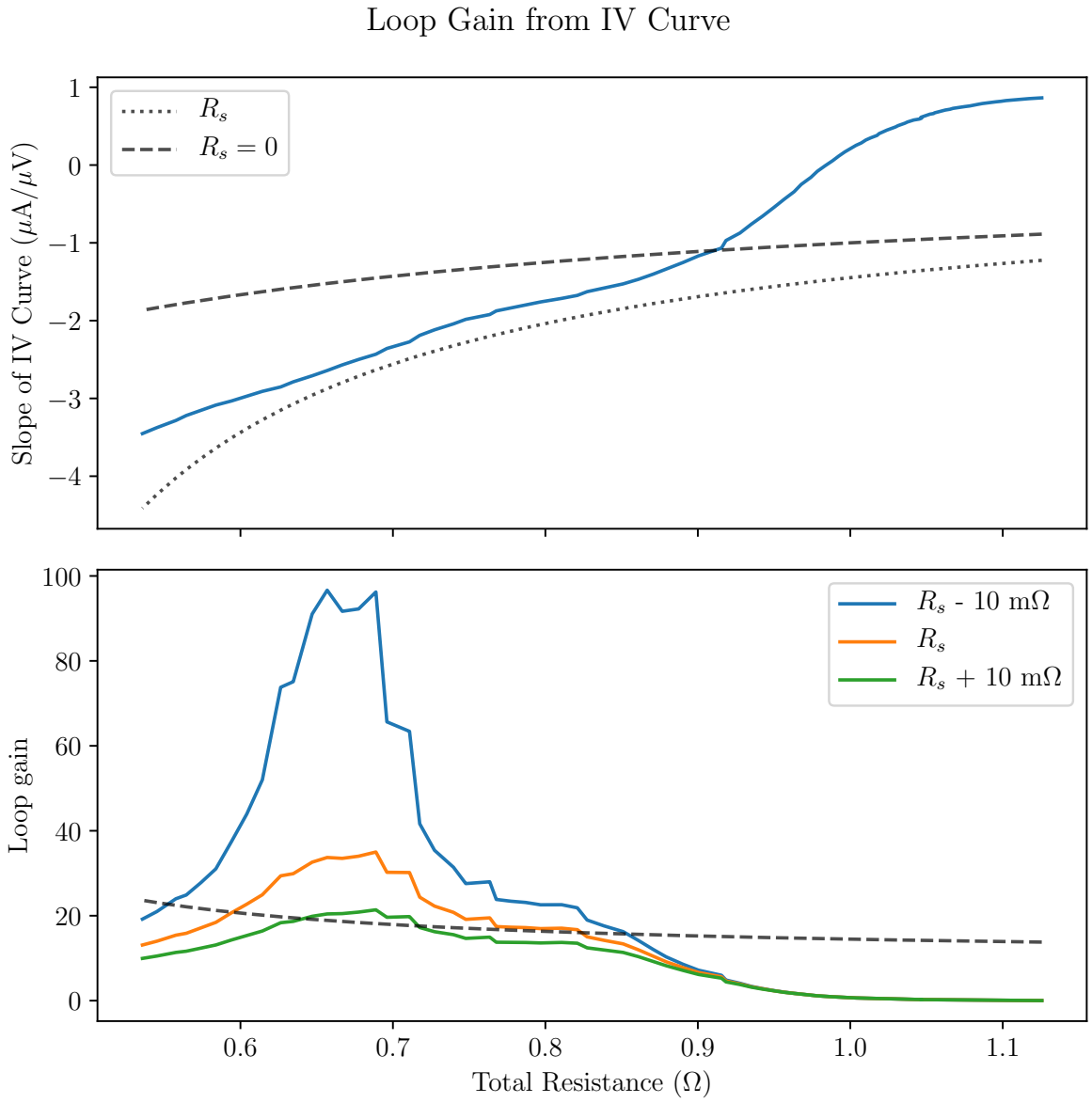

Figure 5.20: The slope of an IV curve and the derived loop gain are shown for a single PB-2b detector measured in a dark condition. *Top:* The slope of an IV curve is plotted against the total resistance. The dashed and dotted lines are the high loop gain limits of the slope in the absence of a stray series resistance and with the measured stray series impedance, respectively. *Bottom:* The loop gain derived from the IV curve of this detector is shown for the measured R_s and the measured value plus and minus 10 mΩ. The derived loop gain depends strongly on the value of R_s used in the calculation. The dashed line represents the high loop gain limit in the presence of a series stray resistance. The curve is given by $\mathcal{L} = 10(R_0 + R_s)/(R_0 - R_s)$. The loop gain of the TES, assuming R_s is correct as measured, is in the high loop gain limit in the range $R_{tot} \approx$ 0.6 Ω - 0.8 Ω.

loop gain to decrease by a factor of about half when these detectors are observing in Chile.

5.3.1 Measurement Technique

A chopped optical source produces a square wave signal of angular frequency ω_c:

$$P_{opt}(t) = p\sum_n \frac{1}{2n+1}\sin((2n+1)\omega_c t), \tag{5.42}$$

where p is the amplitude of the optical power signal. The amplitude and phase of the TES current response is determined by its responsivity:

$$I = p\sum_{n=0}^{n_{max}} \frac{1}{2n+1} S_I(R_{frac}, \omega_c; R_s)\sin((2n+1)\omega_c t), \tag{5.43}$$

I'll use the notation I_{ω_c} to refer to the coefficient of the $n = 0$ component of $|I|$, i.e.

$$I_{\omega_c} = p|S_I(R_{frac}, \omega_c; R_s)| \tag{5.44}$$

The responsivity is expected to take the form of a single-pole low-pass filter (see Fig. 5.21), so Eq. 5.44 can be written as:

$$I_{\omega_c} \propto \frac{1}{\sqrt{1+(\omega_c\tau)^2}}. \tag{5.45}$$

We can determine the TES time constant by measuring I_{ω_c} for several values of ω_c and finding the frequency at which the response is decreased by 3 dB.

Repeated the aforementioned measurement at several values of R_{frac} will trace out the R_{frac} dependence of S_I.

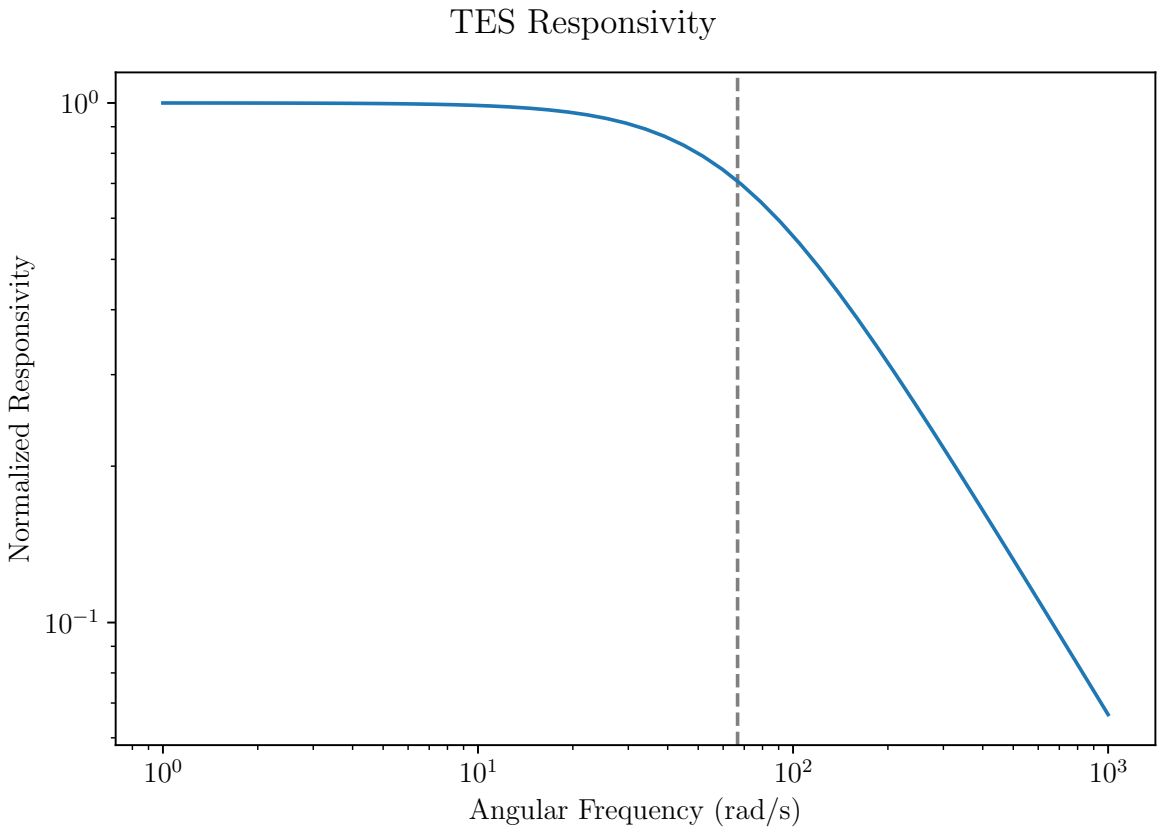

Figure 5.21: A schematic representation of the normalized responsivity of a TES as a function of ω is shown. The responsivity is constant at low frequencies and rolls off at high frequencies. The inverse of the angular frequency at which the responsivity has decreased by 3 dB is the TES time constant. The vertical dashed line is plotted at the 3 dB frequency of $(15\text{ ms})^{-1}$.

5.3.2 Responsivity and Time Constant of PB-2b Detectors

The author performed measurements of the current response of three wafers in the PB-2b receiver to chopped optical signals at multiple chop frequencies and tuning points. The measurements and analysis are described below.

The current response of a detector at a constant tuning point of $R_{frac} = 0.45$ observing a source chopped at several frequencies is shown is Fig. 5.22. The model of Eq. 5.43 was fit to the data, keeping only the first term of the series. The response amplitude decreases as the chop frequency is increased as expected.

The results of many measurements of the same detector are shown in Fig. 5.23. The detector response increases and time constant decreases as R_{frac} is lowered. These are both expected behaviors.

The current response and time constants for 85 detectors are shown in Fig. 5.24. We observe similar behavior in most detectors. As the fractional resistance decreases, the response tends to increase and the time constant tends to decrease. There is a large range of resistance values in which the detector have a time constant within our target range. The response amplitude increases by a factor of 10-100 over the range of fractional resistances shown.

5.3.3 Effects of Stray Impedance on TES Time Constants

The measurements in this section were performed using wafer PB20.13.17 during Run 17b in the PB-2b receiver on March 5, 2019. PB20.13.17 is a wafer with known TES degradation that causes R_n to increase over time and non-uniformly across the wafer. For this reason, PB20.13.17 was not a candidate wafer for PB-2b. However, previous dark characterization of this wafer indicated that the TESs were not otherwise negatively affected by the increase in R_n. The goal of the characterization described in this section was to measure the time constant of the TESs on wafer PB20.13.17 at multiple points in their transition and to compare the measurement to the

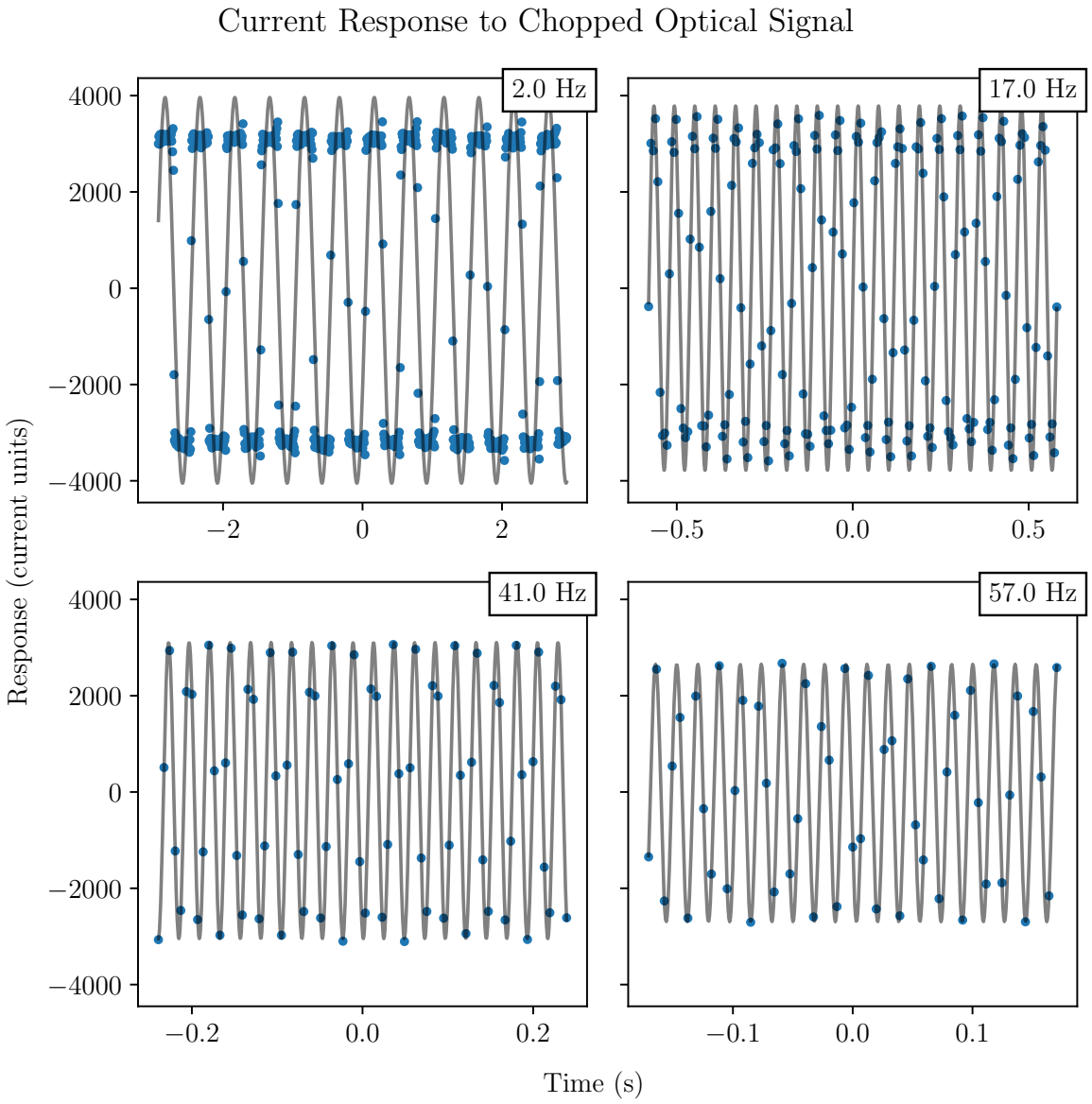

Figure 5.22: Plots of the current response of a TES as a function of chop frequency. The chop frequency is indicated in the top right corner of each plot. The amplitude of the current response decreases as the chop frequency is increased. The gray curve in each plot is the best-fit sinuosoid.

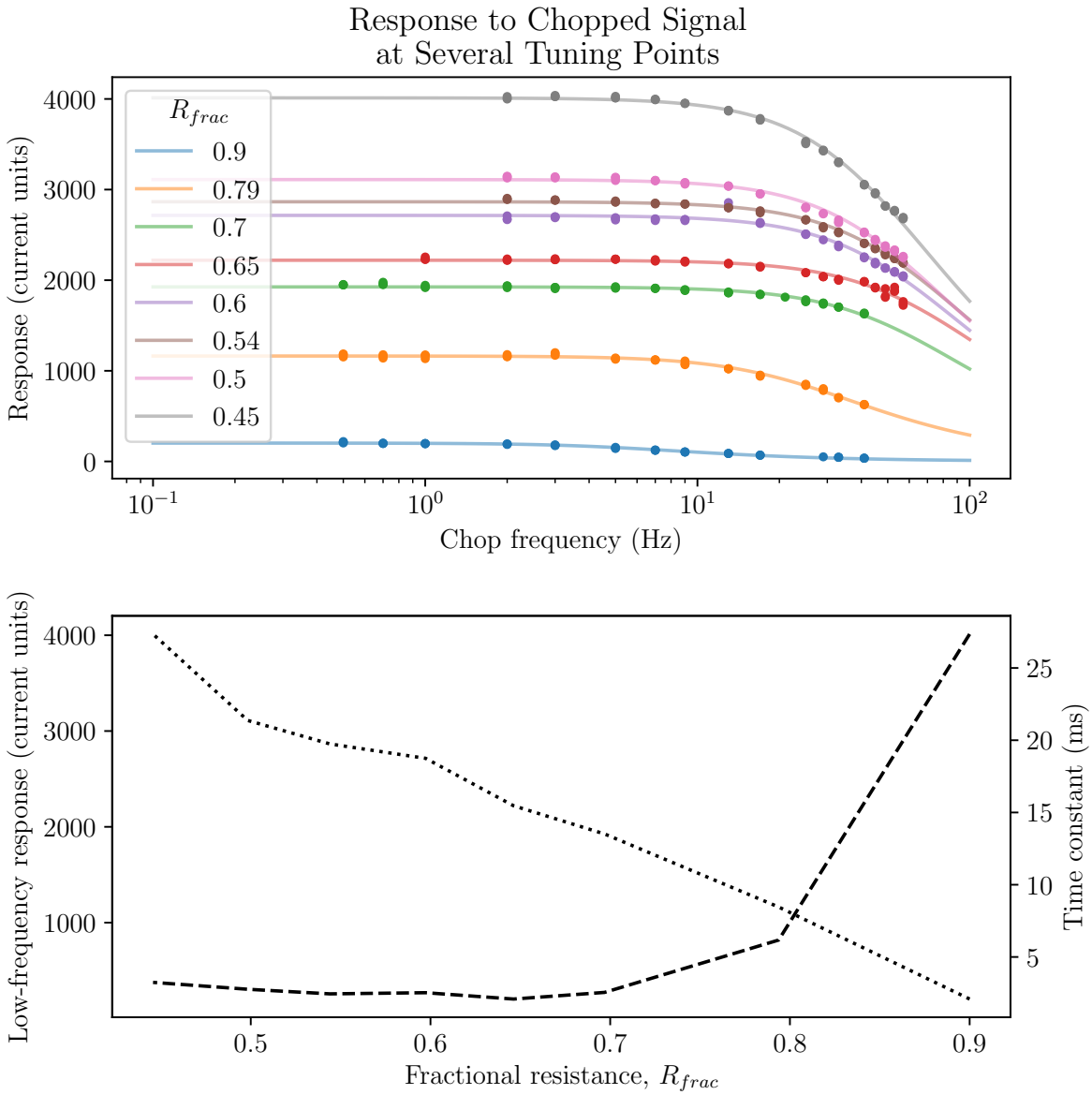

Figure 5.23: The response of a single detector to a chopped optical signal is shown. *Top*: Plot of the response to a chopped optical signal is shown for several values of fractional resistance and chop frequency. Each color corresponds to a single value of R_{frac}. The dots are individual measurements and the solid lines are fits to the data. The low-frequency amplitude of the data at each resistance value increases as the resistance decreases. This is because the responsivity of the detector is increasing. *Bottom*: The low-frequency response (dotted line) and time constant (dashed lines) are plotted as a function of fractional resistance. The low-frequency response and time constant have the expected trends with fractional resistance.

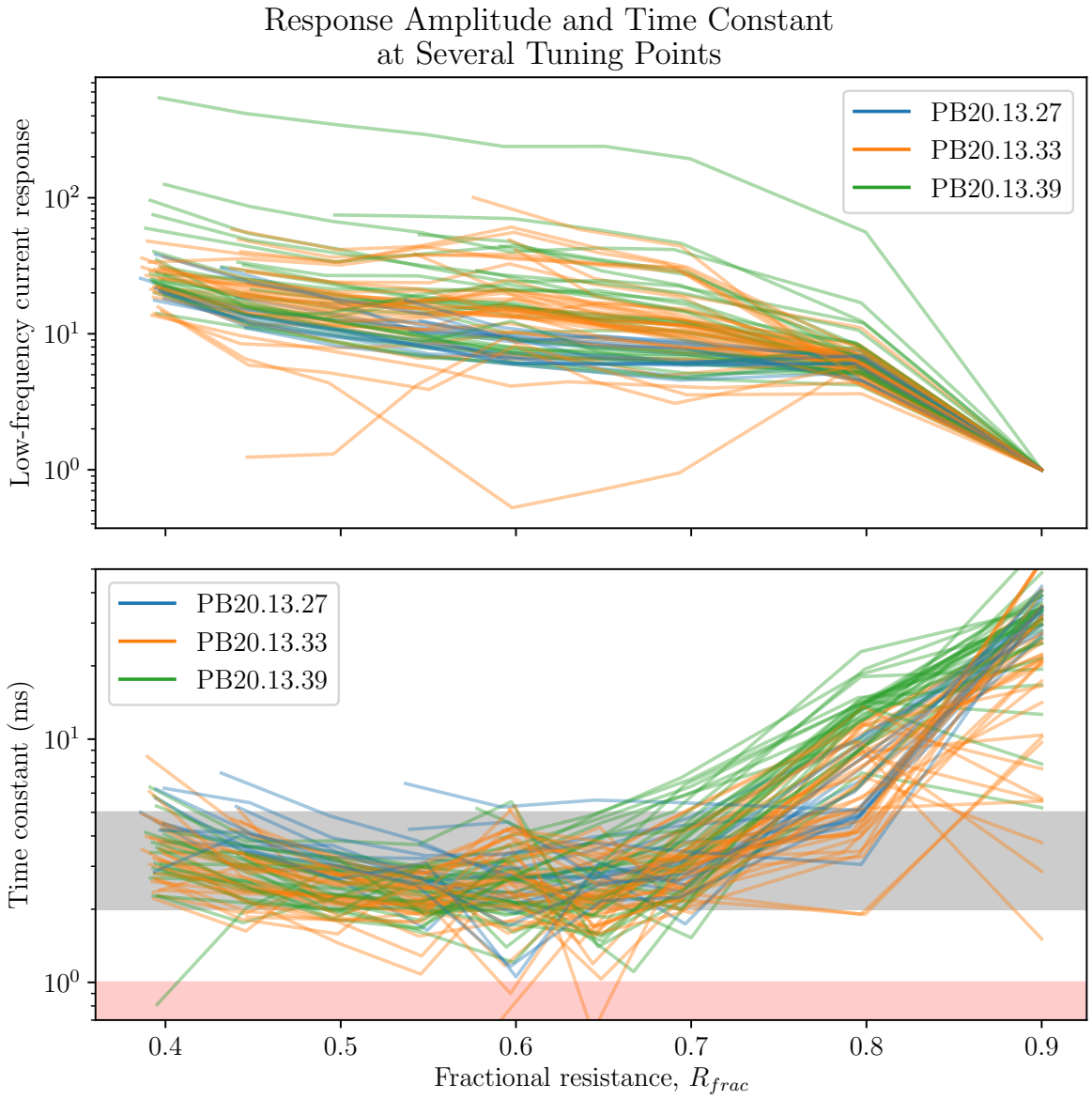

Figure 5.24: Low-frequency response and time constants of 85 detectors across three wafers in PB-2b Run18b are shown. In both plots, the line color represents the wafer that the bolometer belongs too. *Top*: The current response is plotted as a function of fractional resistance. The response has been normalized to 1 for all detectors at $R_{frac} = 0.9$. This was done to compensate for the fact that each detector is likely receiving a different amplitude of optical power input. The responsivity increases by a factor of about 10-100 across the R_{frac} range shown here. *Bottom*: The time constants of 85 detectors in Run 18b are shown here. The gray band in the top plot indicates the range of target time constants and the red band indicates the instability region due to the bandwidth of the bias circuit. Most TESs have acceptable time constants for R_{fracs} in the range of 0.4-0.7.

time constant model developed in Sec. 5.1.2. Detector time constants were measured at R_{fracs} in the range of 0.4 to 0.9 using a chopped optical source with chop frequencies between 4 Hz and 31 Hz.

Detector time constants were measured at R_{fracs} in the range of 0.4 to 0.9.

In order to validate the stray impedance model in Sec. 5.1.2, I compared the measured values of τ for a subset of detectors on PB20.13.17 to the time constant equation:

$$\tau = \frac{\tau_0}{\mathcal{L}\frac{R_0 - R_s}{R_0 + R_s} + 1}. \tag{5.46}$$

The loop gain, $\mathcal{L}$, can be retrieved from IV curves of PB20.13.17 using Eq. 5.35. Substituting Eq. 5.35 into Eq. 5.46 yields this equation for the time constant:

$$\tau = \tau_0 \left[\left(\frac{1 - R_{tot}\frac{\delta I}{\delta V}}{1 + (R_{tot} - 2R_s)\frac{\delta I}{\delta V}} \right) \left(\frac{R_{tot} - 2R_s}{R_{tot}} \right) + 1 \right]^{-1} \tag{5.47}$$

where I am using the total resistance, $R_{tot} \equiv R_0 + R_s$. This is a two-parameter model that can be used to predict the time constant of the TES given a previous IV curve measurement. The two parameters of the model are R_s and τ_0.

I fit the measured time constant data to this model using the previously measured IV curves to obtain $\frac{\delta I}{\delta V}$. The data and resulting fits are shown in Fig. 5.25. The retrieved values of τ_0 are approximately 30 ms, which is consistent with our expectations based on their design. The retrieved values of R_s are consistent with the R_s values measured using IV curves to within a few percent. The model appears to accurately describe the electrothermal response time of the TES as it transitions. Additionally, the expected time constant in the absence of stray impedance is shown in Fig. 5.25. The model in Eq. 5.47 does not match the data well when the constraint $R_s = 0$ is imposed.

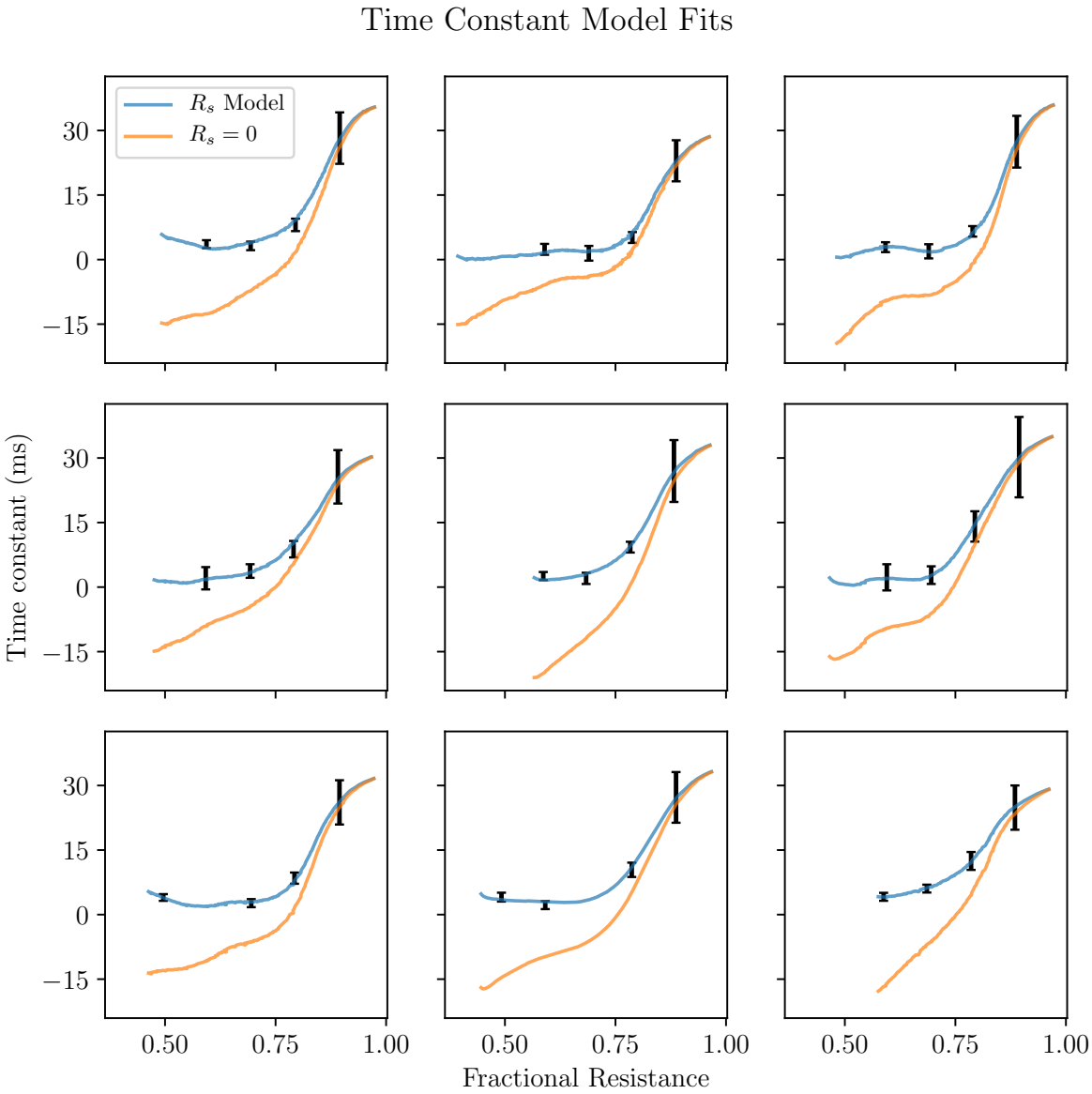

Figure 5.25: Measured time constants for nine detectors are plotted as a function of fractional resistance in black. The vertical extent of the black lines represent the uncertainty of the time constant value. The blue line is a fit of the model in Eq. 5.47. The orange line shows the prediction of the model in Eq. 5.47 when the constraint $R_s = 0$ is imposed. Clearly, the model that allows for a nonzero value of R_s is a much better fit to the data. Note that using a larger value of τ_0 for the orange line will not prevent the model from crossing $\tau = 0$ nor will it change the fractional resistance at which the crossing occurs.

5.4 Conclusions

Characterizing TES parameters was a key task in ensuring that SA would not be limited by detector performance. TES parameters were measured in dark conditions in a test cryostat and the PB-2b receiver. In order to accurately interpret the results of TES measurements, the author developed a model of stray impedances in the DfMux cryogenic circuit and used that model to calibrate the measured data. This model was used to characterize PB-2a and PB-2b detectors.

In order to understand the impacts of stray impedance on TES behavior, the small-signal response of the TES in a model with stray impedance was studied. It was shown that a stray series resistance increases the TES responsivity, increases the TES time constant, and creates a mechanism for instability. The dependence of the TES time constant on the model parameters was derived and shown to agree with data.

5.5 Acknowledgments

This chapter conatins an updated reprint of material as it appears in T. Elleflot, Y. Akiba, K. Arnold, J. Avva, D. Barron, A. N. Bender, A. Cukierman, T. deHaan, M. Dobbs, J. Groh, M. Hasegawa, M. Hazumi, W. Holzapfel, L. Howe, G. Jaehnig, B. Keating, A. Kusaka, A. T. Lee, L. Lowry, J. Montgomery, H. Nishino, C. Raum, K. M. Rotermund, M. Silva-Feaver, A. Suzuki, B. Westbrook, and N. Whitehorn, "Detector and readout assembly and characterization for the simons array," Journal of Low Temperature Physics, vol. 193, pp. 1094–1102, Dec 2018. The dissertation author was the primary author of this work.

This chapter conatins an updated reprint of material as it appears in T. Elleflot, K. Arnold, D. Barron, K. T. Crowley, M. Dobbs, J. Groh, M. Hasegawa, M. Hazumi, C. Hill, L. Howe, J. Ito, O. Jeong, D. Kaneko, N. Katayama, B. Keating, A. Kusaka, A. T. Lee, L. N. Lowry, C. Raum, J. Seibert, M. Silva-Feaver, P. Siritanasak, A. Suzuki, S. Takakura, S. Takatori, C. Tsai, B. Westbrook. "Effect of Stray Impedance in Frequency-Division Multiplexed Readout

of TES Sensors in POLARBEAR-2B." Submitted to Journal of Low Temperature Physics. The dissertation author was the primary author of this work.

Chapter 6

Simons Array Status and Path Forward

6.1 PB-2a Deployment

PB-2a was deployed to Chile in November and December of 2018. Pictures of the deployment are shown in Figs. 6.1-6.3.

During the deployment I performed the room temperature electrical verification of the cryogenic readout circuit that is described in detail in Sec. 4.2.5. The result of this verification was that 97% of the multiplexing circuits were properly connected, which was considered an acceptable yield. The remaining 3% had problems that were not reparable without significantly disassembling the detector module, which presents significant risk of causing further damage. A picture of the detector wafers installed in the POLARBEAR-2a receiver is shown in Fig. 6.1.

I also built and installed the PB-2a saddlebags during this deployment. Pictures of the saddlebags taken during and after the PB-2a deployment are shown in Figs. 6.2, 6.2, and 6.4.

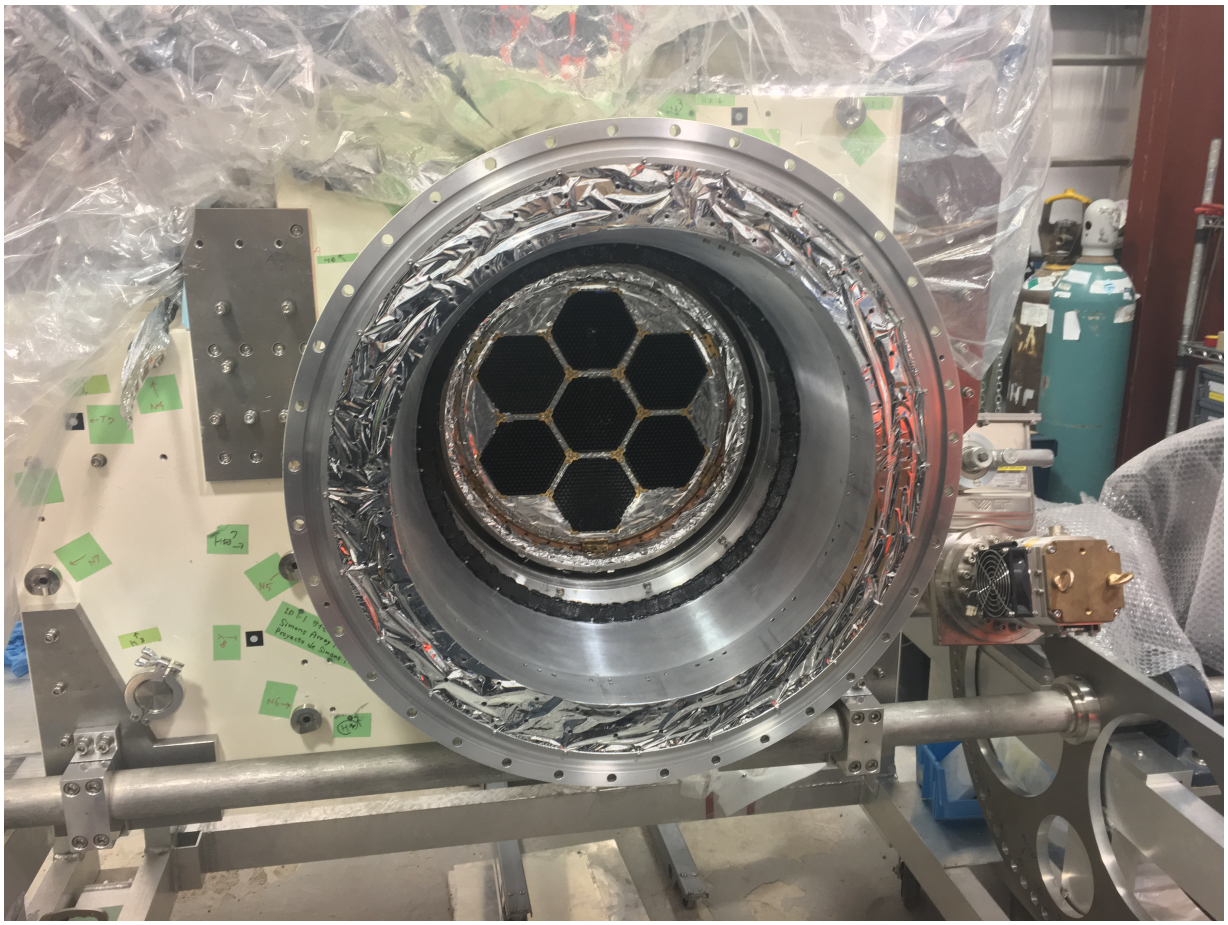

Figure 6.1: A picture of the POLARBEAR-2a receiver during its deployment to Chile, taken in November 2018 by the author. We are looking down the boresight of the optics tube before any of the optical elements have been installed. The seven detectors wafers are installed and can be seen.

Figure 6.2: A picture of the POLARBEAR-2a telescope with two saddlebags installed taken in November 2018 by the author.

Figure 6.3: A picture of the POLARBEAR-2a telescope with all four saddlebags installed. This picture was taken in November 2019. Image credit: Lindsay Lowry.

Figure 6.4: A picture of the POLARBEAR-2b telescope with all four saddlebags installed. This picture was taken in November 2019. Image credit: Daisuke Kaneko.

6.2 PB-2b Commissioning

The last in-lab cooldown of PB-2b took place from June to November 2019 at UCSD. The receiver has been validated and will be deployed to Chile in early 2020.

To provide site-like conditions, we installed all of the readout and control electronics into replica saddlebags in the same layout that we plan to install them in the field. The replica saddlebags have the same dimensions as the actual saddlebags and use the same electrically isolating polycarbonate electronics rack. We paid careful attention to grounding, providing separate ground paths for the readout electronics and auxiliary electronics. Proper grounding has been shown to be very important for readout noise performance. In order to achieve the proper grounding configuration, we also installed fiber communications to carry the 10 MHz clock signal and the IRIG-B signal to the readout and auxiliary electronics, identically to how this is done on the telescope.

There were a number of criteria enumerated that needed to be met in order to consider the cooldown a success. The criteria include validation of the CHWP operation, detectors, receiver optics, SQUIDs, and receiver vibrational response. The detector validation is covered in detail in earlier chapters. Receiver optics were validated by measuring detector beams and looking for truncation from the Lyot stop. The truncation appeared where expected, so this was a success. Receiver vibrational response was measured at room temperature and at cryogenic temperatures and the result is that we will likely need to modify the focal plane tower to be less susceptible to vibrational heating. The SQUID performance has been measured and the data will be used to determine the best SQUIDs and the proper polarity to install them with.

Photos of the assembly process and of the CHWP encoder signal during it's first spin in the PB-2b receiver are shown in Fig. 6.5.

Figure 6.5: Pictures of the assembly and commissioning of the PB-2b optics tube and CHWP taken by the author. *Top right:* The collimator lens and RF shield has been installed. *Top right:* The CHWP is being installed. *Bottom left:* The cryogenic parts of the optics tube are fully assembled, except for the RT-MLI. The visible off-white piece is the alumina filter. *Bottom right:* The first spinning of the CHWP in the PB-2b receiver. The oscilloscope is reading the signal from the CHWP encoder. The CHWP is spinning stably at 2 Hz.

Bibliography

[1] P. Collaboration, N. Aghanim, Y. Akrami, M. Ashdown, J. Aumont, C. Baccigalupi, M. Ballardini, A. J. Banday, R. B. Barreiro, N. Bartolo, S. Basak, K. Benabed, J. P. Bernard, M. Bersanelli, P. Bielewicz, J. R. Bond, J. Borrill, F. R. Bouchet, F. Boulanger, M. Bucher, C. Burigana, E. Calabrese, J. F. Cardoso, J. Carron, A. Challinor, H. C. Chiang, L. P. L. Colombo, C. Combet, F. Couchot, B. P. Crill, F. Cuttaia, P. de Bernardis, A. de Rosa, G. de Zotti, J. Delabrouille, J. M. Delouis, E. D. Valentino, J. M. Diego, O. Doré, M. Douspis, A. Ducout, X. Dupac, G. Efstathiou, F. Elsner, T. A. Enßlin, H. K. Eriksen, E. Falgarone, Y. Fantaye, F. Finelli, M. Frailis, A. A. Fraisse, E. Franceschi, A. Frolov, S. Galeotta, S. Galli, K. Ganga, R. T. Génova-Santos, M. Gerbino, T. Ghosh, J. González-Nuevo, K. M. Górski, S. Gratton, A. Gruppuso, J. E. Gudmundsson, W. Handley, F. K. Hansen, S. Henrot-Versillé, D. Herranz, E. Hivon, Z. Huang, A. H. Jaffe, W. C. Jones, A. Karakci, E. Keihänen, R. Keskitalo, K. Kiiveri, J. Kim, T. S. Kisner, N. Krachmalnicoff, M. Kunz, H. Kurki-Suonio, G. Lagache, J. M. Lamarre, A. Lasenby, M. Lattanzi, C. R. Lawrence, F. Levrier, M. Liguori, P. B. Lilje, V. Lindholm, M. López-Caniego, Y. Z. Ma, J. F. Macías-Pérez, G. Maggio, D. Maino, N. Mandolesi, A. Mangilli, P. G. Martin, E. Martínez-González, S. Matarrese, N. Mauri, J. D. McEwen, A. Melchiorri, A. Mennella, M. Migliaccio, M. A. Miville-Deschênes, D. Molinari, A. Moneti, L. Montier, G. Morgante, A. Moss, S. Mottet, P. Natoli, L. Pagano, D. Paoletti, B. Partridge, G. Patanchon, L. Patrizii, O. Perdereau, F. Perrotta, V. Pettorino, F. Piacentini, J. L. Puget, J. P. Rachen, M. Reinecke, M. Remazeilles, A. Renzi, G. Rocha, G. Roudier, L. Salvati, M. Sandri, M. Savelainen, D. Scott, C. Sirignano, G. Sirri, L. D. Spencer, R. Sunyaev, A. S. Suur-Uski, J. A. Tauber, D. Tavagnacco, M. Tenti, L. Toffolatti, M. Tomasi, M. Tristram, T. Trombetti, J. Valiviita, F. Vansyngel, B. V. Tent, L. Vibert, P. Vielva, F. Villa, N. Vittorio, B. D. Wandelt, I. K. Wehus, and A. Zonca, "Planck 2018 results. iii. high frequency instrument data processing and frequency maps," 2018.

[2] P. Collaboration, Y. Akrami, F. Arroja, M. Ashdown, J. Aumont, C. Baccigalupi, M. Ballardini, A. J. Banday, R. B. Barreiro, N. Bartolo, S. Basak, K. Benabed, J. P. Bernard, M. Bersanelli, P. Bielewicz, J. J. Bock, J. R. Bond, J. Borrill, F. R. Bouchet, F. Boulanger, M. Bucher, C. Burigana, R. C. Butler, E. Calabrese, J. F. Cardoso, J. Carron, A. Challinor, H. C. Chiang, L. P. L. Colombo, C. Combet, D. Contreras, B. P. Crill, F. Cuttaia, P. de Bernardis, G. de Zotti, J. Delabrouille, J. M. Delouis, E. D. Valentino, J. M. Diego, S. Donzelli, O. Doré, M. Douspis, A. Ducout, X. Dupac, S. Dusini, G. Efstathiou, F. Elsner, T. A. Enßlin, H. K. Eriksen, Y. Fantaye, J. Fergusson, R. Fernandez-Cobos, F. Finelli,

F. Forastieri, M. Frailis, E. Franceschi, A. Frolov, S. Galeotta, S. Galli, K. Ganga, C. Gauthier, R. T. Génova-Santos, M. Gerbino, T. Ghosh, J. González-Nuevo, K. M. Górski, S. Gratton, A. Gruppuso, J. E. Gudmundsson, J. Hamann, W. Handley, F. K. Hansen, D. Herranz, E. Hivon, D. C. Hooper, Z. Huang, A. H. Jaffe, W. C. Jones, E. Keihänen, R. Keskitalo, K. Kiiveri, J. Kim, T. S. Kisner, N. Krachmalnicoff, M. Kunz, H. Kurki-Suonio, G. Lagache, J. M. Lamarre, A. Lasenby, M. Lattanzi, C. R. Lawrence, M. L. Jeune, J. Lesgourgues, F. Levrier, A. Lewis, M. Liguori, P. B. Lilje, V. Lindholm, M. Lpez-Caniego, P. M. Lubin, Y. Z. Ma, J. F. Macías-Pérez, G. Maggio, D. Maino, N. Mandolesi, A. Mangilli, A. Marcos-Caballero, M. Maris, P. G. Martin, E. Martínez-González, S. Matarrese, N. Mauri, J. D. McEwen, P. D. Meerburg, P. R. Meinhold, A. Melchiorri, A. Mennella, M. Migliaccio, S. Mitra, M. A. Miville-Deschênes, D. Molinari, A. Moneti, L. Montier, G. Morgante, A. Moss, M. Münchmeyer, P. Natoli, H. U. Nørgaard-Nielsen, L. Pagano, D. Paoletti, B. Partridge, G. Patanchon, H. V. Peiris, F. Perrotta, V. Pettorino, F. Piacentini, L. Polastri, G. Polenta, J. L. Puget, J. P. Rachen, M. Reinecke, M. Remazeilles, A. Renzi, G. Rocha, C. Rosset, G. Roudier, J. A. Rubiño-Martín, B. Ruiz-Granados, L. Salvati, M. Sandri, M. Savelainen, D. Scott, E. P. S. Shellard, M. Shiraishi, C. Sirignano, G. Sirri, L. D. Spencer, R. Sunyaev, A. S. Suur-Uski, J. A. Tauber, D. Tavagnacco, M. Tenti, L. Toffolatti, M. Tomasi, T. Trombetti, J. Valiviita, B. V. Tent, P. Vielva, F. Villa, N. Vittorio, B. D. Wandelt, I. K. Wehus, S. D. M. White, A. Zacchei, J. P. Zibin, and A. Zonca, "Planck 2018 results. x. constraints on inflation," 2018.

[3] S. Adachi, M. A. O. A. Faúndez, K. Arnold, C. Baccigalupi, D. Barron, D. Beck, S. Beckman, F. Bianchini, D. Boettger, J. Borrill, J. Carron, S. Chapman, K. Cheung, Y. Chinone, K. Crowley, A. Cukierman, M. Dobbs, H. E. Bouhargani, T. Elleflot, J. Errard, G. Fabbian, C. Feng, T. Fujino, N. Galitzki, N. Goeckner-Wald, J. Groh, G. Hall, N. Halverson, T. Hamada, M. Hasegawa, M. Hazumi, C. A. Hill, L. Howe, Y. Inoue, G. Jaehnig, O. Jeong, D. Kaneko, N. Katayama, B. Keating, R. Keskitalo, S. Kikuchi, T. Kisner, N. Krachmalnicoff, A. Kusaka, A. T. Lee, D. Leon, E. Linder, L. N. Lowry, A. Mangu, F. Matsuda, Y. Minami, M. Navaroli, H. Nishino, A. T. P. Pham, D. Poletti, G. Puglisi, C. L. Reichardt, Y. Segawa, M. Silva-Feaver, P. Siritanasak, N. Stebor, R. Stompor, A. Suzuki, O. Tajima, S. Takakura, S. Takatori, D. Tanabe, G. P. Teply, C. Tsai, C. Verges, B. Westbrook, and Y. Zhou, "A measurement of the degree scale cmb b-mode angular power spectrum with polarbear," 2019.

[4] K. Arnold, N. Stebor, P. A. R. Ade, Y. Akiba, A. E. Anthony, M. Atlas, D. Barron, A. Bender, D. Boettger, J. Borrill, S. Chapman, Y. Chinone, A. Cukierman, M. Dobbs, T. Elleflot, J. Errard, G. Fabbian, C. Feng, A. Gilbert, N. Goeckner-Wald, N. W. Halverson, M. Hasegawa, K. Hattori, M. Hazumi, W. L. Holzapfel, Y. Hori, Y. Inoue, G. C. Jaehnig, A. H. Jaffe, N. Katayama, B. Keating, Z. Kermish, R. Keskitalo, T. Kisner, M. L. Jeune, A. T. Lee, E. M. Leitch, E. Linder, F. Matsuda, T. Matsumura, X. Meng, N. J. Miller, H. Morii, M. J. Myers, M. Navaroli, H. Nishino, T. Okamura, H. Paar, J. Peloton, D. Poletti, C. Raum, G. Rebeiz, C. L. Reichardt, P. L. Richards, C. Ross, K. M. Rotermund, D. E. Schenck, B. D. Sherwin, I. Shirley, M. Sholl, P. Siritanasak, G. Smecher, B. Steinbach, R. Stompor, A. Suzuki, J. Suzuki, S. Takada, S. Takakura, T. Tomaru, B. Wilson, A. Yadav, and O. Zahn, "The

Simons Array: expanding POLARBEAR to three multi-chroic telescopes," in *Millimeter, Submillimeter, and Far-Infrared Detectors and Instrumentation for Astronomy VII* (W. S. Holland and J. Zmuidzinas, eds.), vol. 9153, pp. 466 – 473, International Society for Optics and Photonics, SPIE, 2014.

[5] Y. Inoue, P. Ade, Y. Akiba, C. Aleman, K. Arnold, C. Baccigalupi, B. Barch, D. Barron, A. Bender, D. Boettger, J. Borrill, S. Chapman, Y. Chinone, A. Cukierman, T. de Haan, M. A. Dobbs, A. Ducout, R. Dünner, T. Elleflot, J. Errard, G. Fabbian, S. Feeney, C. Feng, G. Fuller, A. J. Gilbert, N. Goeckner-Wald, J. Groh, G. Hall, N. Halverson, T. Hamada, M. Hasegawa, K. Hattori, M. Hazumi, C. Hill, W. L. Holzapfel, Y. Hori, L. Howe, F. Irie, G. Jaehnig, A. Jaffe, O. Jeong, N. Katayama, J. P. Kaufman, K. Kazemzadeh, B. G. Keating, Z. Kermish, R. Keskitalo, T. S. Kisner, A. Kusaka, M. L. Jeune, A. T. Lee, D. Leon, E. V. Linder, L. Lowry, F. Matsuda, T. Matsumura, N. Miller, K. Mizukami, J. Montgomery, M. Navaroli, H. Nishino, H. Paar, J. Peloton, D. Poletti, G. Puglisi, C. R. Raum, G. M. Rebeiz, C. L. Reichardt, P. L. Richards, C. Ross, K. M. Rotermund, Y. Segawa, B. D. Sherwin, I. Shirley, P. Siritanasak, N. Stebor, R. Stompor, J. Suzuki, A. Suzuki, O. Tajima, S. Takada, S. Takatori, G. P. Teply, A. Tikhomirov, T. Tomaru, N. Whitehorn, A. Zahn, and O. Zahn, "POLARBEAR-2: an instrument for CMB polarization measurements," in *Millimeter, Submillimeter, and Far-Infrared Detectors and Instrumentation for Astronomy VIII* (W. S. Holland and J. Zmuidzinas, eds.), vol. 9914, pp. 372 – 380, International Society for Optics and Photonics, SPIE, 2016.

[6] L. Howe, C. Tsai, L. Lowry, K. Arnold, G. Coppi, J. Groh, X. Guo, B. Keating, A. Lee, A. J. May, L. Piccirillo, N. Stebor, and G. Teply, "Design and characterization of the POLARBEAR-2b and POLARBEAR-2c cosmic microwave background cryogenic receivers," in *Millimeter, Submillimeter, and Far-Infrared Detectors and Instrumentation for Astronomy IX* (J. Zmuidzinas and J.-R. Gao, eds.), vol. 10708, pp. 624 – 643, International Society for Optics and Photonics, SPIE, 2018.

[7] B. Westbrook, P. A. R. Ade, M. Aguilar, Y. Akiba, K. Arnold, C. Baccigalupi, D. Barron, D. Beck, S. Beckman, A. N. Bender, F. Bianchini, D. Boettger, J. Borrill, S. Chapman, Y. Chinone, G. Coppi, K. Crowley, A. Cukierman, T. de Haan, R. Dünner, M. Dobbs, T. Elleflot, J. Errard, G. Fabbian, S. M. Feeney, C. Feng, G. Fuller, N. Galitzki, A. Gilbert, N. Goeckner-Wald, J. Groh, N. W. Halverson, T. Hamada, M. Hasegawa, M. Hazumi, C. A. Hill, W. Holzapfel, L. Howe, Y. Inoue, G. Jaehnig, A. Jaffe, O. Jeong, D. Kaneko, N. Katayama, B. Keating, R. Keskitalo, T. Kisner, N. Krachmalnicoff, A. Kusaka, M. Le Jeune, A. T. Lee, D. Leon, E. Linder, L. Lowry, A. Madurowicz, D. Mak, F. Matsuda, A. May, N. J. Miller, Y. Minami, J. Montgomery, M. Navaroli, H. Nishino, J. Peloton, A. Pham, L. Piccirillo, D. Plambeck, D. Poletti, G. Puglisi, C. Raum, G. Rebeiz, C. L. Reichardt, P. L. Richards, H. Roberts, C. Ross, K. M. Rotermund, Y. Segawa, B. Sherwin, M. Silva-Feaver, P. Siritanasak, R. Stompor, A. Suzuki, O. Tajima, S. Takakura, S. Takatori, D. Tanabe, R. Tat, G. P. Teply, A. Tikhomirov, T. Tomaru, C. Tsai, N. Whitehorn, and A. Zahn, "The polarbear-2 and simons array focal plane fabrication status," *Journal of Low Temperature Physics*, vol. 193, pp. 758–770, Dec 2018.

[8] P. Collaboration, N. Aghanim, Y. Akrami, M. Ashdown, J. Aumont, C. Baccigalupi, M. Ballardini, A. J. Banday, R. B. Barreiro, N. Bartolo, S. Basak, R. Battye, K. Benabed, J. P. Bernard, M. Bersanelli, P. Bielewicz, J. J. Bock, J. R. Bond, J. Borrill, F. R. Bouchet, F. Boulanger, M. Bucher, C. Burigana, R. C. Butler, E. Calabrese, J. F. Cardoso, J. Carron, A. Challinor, H. C. Chiang, J. Chluba, L. P. L. Colombo, C. Combet, D. Contreras, B. P. Crill, F. Cuttaia, P. de Bernardis, G. de Zotti, J. Delabrouille, J. M. Delouis, E. D. Valentino, J. M. Diego, O. Doré, M. Douspis, A. Ducout, X. Dupac, S. Dusini, G. Efstathiou, F. Elsner, T. A. Enßlin, H. K. Eriksen, Y. Fantaye, M. Farhang, J. Fergusson, R. Fernandez-Cobos, F. Finelli, F. Forastieri, M. Frailis, A. A. Fraisse, E. Franceschi, A. Frolov, S. Galeotta, S. Galli, K. Ganga, R. T. Génova-Santos, M. Gerbino, T. Ghosh, J. González-Nuevo, K. M. Górski, S. Gratton, A. Gruppuso, J. E. Gudmundsson, J. Hamann, W. Handley, F. K. Hansen, D. Herranz, S. R. Hildebrandt, E. Hivon, Z. Huang, A. H. Jaffe, W. C. Jones, A. Karakci, E. Keihänen, R. Keskitalo, K. Kiiveri, J. Kim, T. S. Kisner, L. Knox, N. Krachmalnicoff, M. Kunz, H. Kurki-Suonio, G. Lagache, J. M. Lamarre, A. Lasenby, M. Lattanzi, C. R. Lawrence, M. L. Jeune, P. Lemos, J. Lesgourgues, F. Levrier, A. Lewis, M. Liguori, P. B. Lilje, M. Lilley, V. Lindholm, M. López-Caniego, P. M. Lubin, Y. Z. Ma, J. F. Macías-Pérez, G. Maggio, D. Maino, N. Mandolesi, A. Mangilli, A. Marcos-Caballero, M. Maris, P. G. Martin, M. Martinelli, E. Martínez-González, S. Matarrese, N. Mauri, J. D. McEwen, P. R. Meinhold, A. Melchiorri, A. Mennella, M. Migliaccio, M. Millea, S. Mitra, M. A. Miville-Deschênes, D. Molinari, L. Montier, G. Morgante, A. Moss, P. Natoli, H. U. Nørgaard-Nielsen, L. Pagano, D. Paoletti, B. Partridge, G. Patanchon, H. V. Peiris, F. Perrotta, V. Pettorino, F. Piacentini, L. Polastri, G. Polenta, J. L. Puget, J. P. Rachen, M. Reinecke, M. Remazeilles, A. Renzi, G. Rocha, C. Rosset, G. Roudier, J. A. Rubiño-Martín, B. Ruiz-Granados, L. Salvati, M. Sandri, M. Savelainen, D. Scott, E. P. S. Shellard, C. Sirignano, G. Sirri, L. D. Spencer, R. Sunyaev, A. S. Suur-Uski, J. A. Tauber, D. Tavagnacco, M. Tenti, L. Toffolatti, M. Tomasi, T. Trombetti, L. Valenziano, J. Valiviita, B. V. Tent, L. Vibert, P. Vielva, F. Villa, N. Vittorio, B. D. Wandelt, I. K. Wehus, M. White, S. D. M. White, A. Zacchei, and A. Zonca, "Planck 2018 results. vi. cosmological parameters," 2018.

[9] S. Dodelson, *Modern cosmology*. San Diego, CA: Academic Press, 2003.

[10] V. C. Rubin, J. Ford, W. K., and N. Thonnard, "Extended rotation curves of high-luminosity spiral galaxies. IV. Systematic dynamical properties, Sa - Sc.," *The Astrophysical Journal*, vol. 225, pp. L107–L111, Nov 1978.

[11] A. G. Riess, A. V. Filippenko, P. Challis, A. Clocchiatti, A. Diercks, P. M. Garnavich, R. L. Gilliland, C. J. Hogan, S. Jha, R. P. Kirshner, B. Leibundgut, M. M. Phillips, D. Reiss, B. P. Schmidt, R. A. Schommer, R. C. Smith, J. Spyromilio, C. Stubbs, N. B. Suntzeff, and J. Tonry, "Observational evidence from supernovae for an accelerating universe and a cosmological constant," *The Astronomical Journal*, vol. 116, pp. 1009–1038, sep 1998.

[12] A. H. Guth, "Inflationary universe: A possible solution to the horizon and flatness problems," *Phys. Rev. D*, vol. 23, pp. 347–356, Jan 1981.

[13] P. A. R. Ade, Z. Ahmed, R. W. Aikin, K. D. Alexander, D. Barkats, S. J. Benton, C. A. Bischoff, J. J. Bock, R. Bowens-Rubin, J. A. Brevik, I. Buder, E. Bullock, V. Buza, J. Connors, J. Cornelison, B. P. Crill, M. Crumrine, M. Dierickx, L. Duband, C. Dvorkin, J. P. Filippini, S. Fliescher, J. Grayson, G. Hall, M. Halpern, S. Harrison, S. R. Hildebrandt, G. C. Hilton, H. Hui, K. D. Irwin, J. Kang, K. S. Karkare, E. Karpel, J. P. Kaufman, B. G. Keating, S. Kefeli, S. A. Kernasovskiy, J. M. Kovac, C. L. Kuo, N. A. Larsen, K. Lau, E. M. Leitch, M. Lueker, K. G. Megerian, L. Moncelsi, T. Namikawa, C. B. Netterfield, H. T. Nguyen, R. O'Brient, R. W. Ogburn, S. Palladino, C. Pryke, B. Racine, S. Richter, A. Schillaci, R. Schwarz, C. D. Sheehy, A. Soliman, T. St. Germaine, Z. K. Staniszewski, B. Steinbach, R. V. Sudiwala, G. P. Teply, K. L. Thompson, J. E. Tolan, C. Tucker, A. D. Turner, C. Umiltà, A. G. Vieregg, A. Wandui, A. C. Weber, D. V. Wiebe, J. Willmert, C. L. Wong, W. L. K. Wu, H. Yang, K. W. Yoon, and C. Zhang, "Constraints on primordial gravitational waves using *planck*, wmap, and new bicep2/*keck* observations through the 2015 season," *Phys. Rev. Lett.*, vol. 121, p. 221301, Nov 2018.

[14] A. A. Penzias and R. W. Wilson, "A measurement of excess antenna temperature at 4080 mc/s.," *ApJ*, vol. 142, pp. 419–421, Jul 1965.

[15] R. H. Dicke, P. J. E. Peebles, P. G. Roll, and D. T. Wilkinson, "Cosmic Black-Body Radiation.," *ApJ*, vol. 142, pp. 414–419, Jul 1965.

[16] J. C. Mather, E. S. Cheng, D. A. Cottingham, J. Eplee, R. E., D. J. Fixsen, T. Hewagama, R. B. Isaacman, K. A. Jensen, S. S. Meyer, P. D. Noerdlinger, S. M. Read, L. P. Rosen, R. A. Shafer, E. L. Wright, C. L. Bennett, N. W. Boggess, M. G. Hauser, T. Kelsall, J. Moseley, S. H., R. F. Silverberg, G. F. Smoot, R. Weiss, and D. T. Wilkinson, "Measurement of the Cosmic Microwave Background Spectrum by the COBE FIRAS Instrument," *ApJ*, vol. 420, p. 439, Jan 1994.

[17] D. J. Fixsen, E. S. Cheng, J. M. Gales, J. C. Mather, R. A. Shafer, and E. L. Wright, "The cosmic microwave background spectrum from the FullCOBEFIRAS data set," *ApJ*, vol. 473, pp. 576–587, dec 1996.

[18] G. F. Smoot, C. L. Bennett, A. Kogut, E. L. Wright, J. Aymon, N. W. Boggess, E. S. Cheng, G. de Amici, S. Gulkis, M. G. Hauser, G. Hinshaw, P. D. Jackson, M. Janssen, E. Kaita, T. Kelsall, P. Keegstra, C. Lineweaver, K. Loewenstein, P. Lubin, J. Mather, S. S. Meyer, S. H. Moseley, T. Murdock, L. Rokke, R. F. Silverberg, L. Tenorio, R. Weiss, and D. T. Wilkinson, "Structure in the COBE Differential Microwave Radiometer First-Year Maps," *ApJ*, vol. 396, p. L1, Sep 1992.

[19] R. K. Sachs and A. M. Wolfe, "Perturbations of a Cosmological Model and Angular Variations of the Microwave Background," *The Astrophysical Journal*, vol. 147, p. 73, Jan 1967.

[20] P. Collaboration, Y. Akrami, F. Arroja, M. Ashdown, J. Aumont, C. Baccigalupi, M. Ballardini, A. J. Banday, R. B. Barreiro, N. Bartolo, S. Basak, R. Battye, K. Benabed, J. P.

Bernard, M. Bersanelli, P. Bielewicz, J. J. Bock, J. R. Bond, J. Borrill, F. R. Bouchet, F. Boulanger, M. Bucher, C. Burigana, R. C. Butler, E. Calabrese, J. F. Cardoso, J. Carron, B. Casaponsa, A. Challinor, H. C. Chiang, L. P. L. Colombo, C. Combet, D. Contreras, B. P. Crill, F. Cuttaia, P. de Bernardis, G. de Zotti, J. Delabrouille, J. M. Delouis, F. X. Désert, E. D. Valentino, C. Dickinson, J. M. Diego, S. Donzelli, O. Doré, M. Douspis, A. Ducout, X. Dupac, G. Efstathiou, F. Elsner, T. A. Enßlin, H. K. Eriksen, E. Falgarone, Y. Fantaye, J. Fergusson, R. Fernandez-Cobos, F. Finelli, F. Forastieri, M. Frailis, E. Franceschi, A. Frolov, S. Galeotta, S. Galli, K. Ganga, R. T. Génova-Santos, M. Gerbino, T. Ghosh, J. González-Nuevo, K. M. Górski, S. Gratton, A. Gruppuso, J. E. Gudmundsson, J. Hamann, W. Handley, F. K. Hansen, G. Helou, D. Herranz, E. Hivon, Z. Huang, A. H. Jaffe, W. C. Jones, A. Karakci, E. Keihänen, R. Keskitalo, K. Kiiveri, J. Kim, T. S. Kisner, L. Knox, N. Krachmalnicoff, M. Kunz, H. Kurki-Suonio, G. Lagache, J. M. Lamarre, M. Langer, A. Lasenby, M. Lattanzi, C. R. Lawrence, M. L. Jeune, J. P. Leahy, J. Lesgourgues, F. Levrier, A. Lewis, M. Liguori, P. B. Lilje, M. Lilley, V. Lindholm, M. López-Caniego, P. M. Lubin, Y. Z. Ma, J. F. Macías-Pérez, G. Maggio, D. Maino, N. Mandolesi, A. Mangilli, A. Marcos-Caballero, M. Maris, P. G. Martin, E. Martínez-González, S. Matarrese, N. Mauri, J. D. McEwen, P. D. Meerburg, P. R. Meinhold, A. Melchiorri, A. Mennella, M. Migliaccio, M. Millea, S. Mitra, M. A. Miville-Deschênes, D. Molinari, A. Moneti, L. Montier, G. Morgante, A. Moss, S. Mottet, M. Münchmeyer, P. Natoli, H. U. Nørgaard-Nielsen, C. A. Oxborrow, L. Pagano, D. Paoletti, B. Partridge, G. Patanchon, T. J. Pearson, M. Peel, H. V. Peiris, F. Perrotta, V. Pettorino, F. Piacentini, L. Polastri, G. Polenta, J. L. Puget, J. P. Rachen, M. Reinecke, M. Remazeilles, A. Renzi, G. Rocha, C. Rosset, G. Roudier, J. A. Rubiño-Martín, B. Ruiz-Granados, L. Salvati, M. Sandri, M. Savelainen, D. Scott, E. P. S. Shellard, M. Shiraishi, C. Sirignano, G. Sirri, L. D. Spencer, R. Sunyaev, A. S. Suur-Uski, J. A. Tauber, D. Tavagnacco, M. Tenti, L. Terenzi, L. Toffolatti, M. Tomasi, T. Trombetti, J. Valiviita, B. V. Tent, L. Vibert, P. Vielva, F. Villa, N. Vittorio, B. D. Wandelt, I. K. Wehus, M. White, S. D. M. White, A. Zacchei, and A. Zonca, "Planck 2018 results. i. overview and the cosmological legacy of planck," 2018.

[21] U. b. u. Seljak and M. Zaldarriaga, "Signature of gravity waves in the polarization of the microwave background," *Phys. Rev. Lett.*, vol. 78, pp. 2054–2057, Mar 1997.

[22] K. Abazajian, K. Arnold, J. Austermann, B. Benson, C. Bischoff, J. Bock, J. Bond, J. Borrill, E. Calabrese, J. Carlstrom, C. Carvalho, C. Chang, H. Chiang, S. Church, A. Cooray, T. Crawford, K. Dawson, S. Das, M. Devlin, M. Dobbs, S. Dodelson, O. Doré, J. Dunkley, J. Errard, A. Fraisse, J. Gallicchio, N. Halverson, S. Hanany, S. Hildebrandt, A. Hincks, R. Hlozek, G. Holder, W. Holzapfel, K. Honscheid, W. Hu, J. Hubmayr, K. Irwin, W. Jones, M. Kamionkowski, B. Keating, R. Keisler, L. Knox, E. Komatsu, J. Kovac, C.-L. Kuo, C. Lawrence, A. Lee, E. Leitch, E. Linder, P. Lubin, J. McMahon, A. Miller, L. Newburgh, M. Niemack, H. Nguyen, H. Nguyen, L. Page, C. Pryke, C. Reichardt, J. Ruhl, N. Sehgal, U. Seljak, J. Sievers, E. Silverstein, A. Slosar, K. Smith, D. Spergel, S. Staggs, A. Stark, R. Stompor, A. Vieregg, G. Wang, S. Watson, E. Wollack, W. Wu, K. Yoon, and O. Zahn, "Neutrino physics from the cosmic microwave background and large scale structure," *Astroparticle Physics*, vol. 63, pp. 66 – 80, 2015. Dark Energy and CMB.

[23] Z. D. Kermish, P. Ade, A. Anthony, K. Arnold, D. Barron, D. Boettger, J. Borrill, S. Chapman, Y. Chinone, M. A. Dobbs, J. Errard, G. Fabbian, D. Flanigan, G. Fuller, A. Ghribi, W. Grainger, N. Halverson, M. Hasegawa, K. Hattori, M. Hazumi, W. L. Holzapfel, J. Howard, P. Hyland, A. Jaffe, B. Keating, T. Kisner, A. T. Lee, M. L. Jeune, E. Linder, M. Lungu, F. Matsuda, T. Matsumura, X. Meng, N. J. Miller, H. Morii, S. Moyerman, M. J. Myers, H. Nishino, H. Paar, E. Quealy, C. L. Reichardt, P. L. Richards, C. Ross, A. Shimizu, M. Shimon, C. Shimmin, M. Sholl, P. Siritanasak, H. Spieler, N. Stebor, B. Steinbach, R. Stompor, A. Suzuki, T. Tomaru, C. Tucker, and O. Zahn, "The POLARBEAR experiment," in *Millimeter, Submillimeter, and Far-Infrared Detectors and Instrumentation for Astronomy VI* (W. S. Holland, ed.), vol. 8452, pp. 366 – 380, International Society for Optics and Photonics, SPIE, 2012.

[24] T. P. C. P. A. R. Ade, Y. Akiba, A. E. Anthony, K. Arnold, M. Atlas, D. Barron, D. Boettger, J. Borrill, S. Chapman, Y. Chinone, M. Dobbs, T. Elleflot, J. Errard, G. Fabbian, C. Feng, D. Flanigan, A. Gilbert, W. Grainger, N. W. Halverson, M. Hasegawa, K. Hattori, M. Hazumi, W. L. Holzapfel, Y. Hori, J. Howard, P. Hyland, Y. Inoue, G. C. Jaehnig, A. H. Jaffe, B. Keating, Z. Kermish, R. Keskitalo, T. Kisner, M. L. Jeune, A. T. Lee, E. M. Leitch, E. Linder, M. Lungu, F. Matsuda, T. Matsumura, X. Meng, N. J. Miller, H. Morii, S. Moyerman, M. J. Myers, M. Navaroli, H. Nishino, A. Orlando, H. Paar, J. Peloton, D. Poletti, E. Quealy, G. Rebeiz, C. L. Reichardt, P. L. Richards, C. Ross, I. Schanning, D. E. Schenck, B. D. Sherwin, A. Shimizu, C. Shimmin, M. Shimon, P. Siritanasak, G. Smecher, H. Spieler, N. Stebor, B. Steinbach, R. Stompor, A. Suzuki, S. Takakura, T. Tomaru, B. Wilson, A. Yadav, and O. Zahn, "A MEASUREMENT OF THE COSMIC MICROWAVE BACKGROUNDB-MODE POLARIZATION POWER SPECTRUM AT SUB-DEGREE SCALES WITH POLARBEAR," *The Astrophysical Journal*, vol. 794, p. 171, oct 2014.

[25] and P. A. R. Ade, M. Aguilar, Y. Akiba, K. Arnold, C. Baccigalupi, D. Barron, D. Beck, F. Bianchini, D. Boettger, J. Borrill, S. Chapman, Y. Chinone, K. Crowley, A. Cukierman, R. Dünner, M. Dobbs, A. Ducout, T. Elleflot, J. Errard, G. Fabbian, S. M. Feeney, C. Feng, T. Fujino, N. Galitzki, A. Gilbert, N. Goeckner-Wald, J. C. Groh, G. Hall, N. Halverson, T. Hamada, M. Hasegawa, M. Hazumi, C. A. Hill, L. Howe, Y. Inoue, G. Jaehnig, A. H. Jaffe, O. Jeong, D. Kaneko, N. Katayama, B. Keating, R. Keskitalo, T. Kisner, N. Krachmalnicoff, A. Kusaka, M. L. Jeune, A. T. Lee, E. M. Leitch, D. Leon, E. Linder, L. Lowry, F. Matsuda, T. Matsumura, Y. Minami, J. Montgomery, M. Navaroli, H. Nishino, H. Paar, J. Peloton, A. T. P. Pham, D. Poletti, G. Puglisi, C. L. Reichardt, P. L. Richards, C. Ross, Y. Segawa, B. D. Sherwin, M. Silva-Feaver, P. Siritanasak, N. Stebor, R. Stompor, A. Suzuki, O. Tajima, S. Takakura, S. Takatori, D. Tanabe, G. P. Teply, T. Tomaru, C. Tucker, N. Whitehorn, and A. Zahn, "A measurement of the cosmic microwave BackgroundB-mode polarization power spectrum at subdegree scales from two years of polarbear data," *The Astrophysical Journal*, vol. 848, p. 121, oct 2017.

[26] P. A. R. Ade, Y. Akiba, A. E. Anthony, K. Arnold, M. Atlas, D. Barron, D. Boettger, J. Borrill, C. Borys, S. Chapman, Y. Chinone, M. Dobbs, T. Elleflot, J. Errard, G. Fabbian, C. Feng, D. Flanigan, A. Gilbert, W. Grainger, N. W. Halverson, M. Hasegawa, K. Hattori,

M. Hazumi, W. L. Holzapfel, Y. Hori, J. Howard, P. Hyland, Y. Inoue, G. C. Jaehnig, A. Jaffe, B. Keating, Z. Kermish, R. Keskitalo, T. Kisner, M. Le Jeune, A. T. Lee, E. M. Leitch, E. Linder, M. Lungu, F. Matsuda, T. Matsumura, X. Meng, N. J. Miller, H. Morii, S. Moyerman, M. J. Myers, M. Navaroli, H. Nishino, H. Paar, J. Peloton, D. Poletti, E. Quealy, G. Rebeiz, C. L. Reichardt, P. L. Richards, C. Ross, K. Rotermund, I. Schanning, D. E. Schenck, B. D. Sherwin, A. Shimizu, C. Shimmin, M. Shimon, P. Siritanasak, G. Smecher, H. Spieler, N. Stebor, B. Steinbach, R. Stompor, A. Suzuki, S. Takakura, A. Tikhomirov, T. Tomaru, B. Wilson, A. Yadav, and O. Zahn, "Evidence for gravitational lensing of the cosmic microwave background polarization from cross-correlation with the cosmic infrared background," *Phys. Rev. Lett.*, vol. 112, p. 131302, Apr 2014.

[27] P. A. R. Ade, Y. Akiba, A. E. Anthony, K. Arnold, M. Atlas, D. Barron, D. Boettger, J. Borrill, S. Chapman, Y. Chinone, M. Dobbs, T. Elleflot, J. Errard, G. Fabbian, C. Feng, D. Flanigan, A. Gilbert, W. Grainger, N. W. Halverson, M. Hasegawa, K. Hattori, M. Hazumi, W. L. Holzapfel, Y. Hori, J. Howard, P. Hyland, Y. Inoue, G. C. Jaehnig, A. Jaffe, B. Keating, Z. Kermish, R. Keskitalo, T. Kisner, M. Le Jeune, A. T. Lee, E. Linder, E. M. Leitch, M. Lungu, F. Matsuda, T. Matsumura, X. Meng, N. J. Miller, H. Morii, S. Moyerman, M. J. Myers, M. Navaroli, H. Nishino, H. Paar, J. Peloton, E. Quealy, G. Rebeiz, C. L. Reichardt, P. L. Richards, C. Ross, I. Schanning, D. E. Schenck, B. Sherwin, A. Shimizu, C. Shimmin, M. Shimon, P. Siritanasak, G. Smecher, H. Spieler, N. Stebor, B. Steinbach, R. Stompor, A. Suzuki, S. Takakura, T. Tomaru, B. Wilson, A. Yadav, and O. Zahn, "Measurement of the cosmic microwave background polarization lensing power spectrum with the polarbear experiment," *Phys. Rev. Lett.*, vol. 113, p. 021301, Jul 2014.

[28] S. Takakura, M. Aguilar, Y. Akiba, K. Arnold, C. Baccigalupi, D. Barron, S. Beckman, D. Boettger, J. Borrill, S. Chapman, Y. Chinone, A. Cukierman, A. Ducout, T. Elleflot, J. Errard, G. Fabbian, T. Fujino, N. Galitzki, N. Goeckner-Wald, N. W. Halverson, M. Hasegawa, K. Hattori, M. Hazumi, C. Hill, L. Howe, Y. Inoue, A. H. Jaffe, O. Jeong, D. Kaneko, N. Katayama, B. Keating, R. Keskitalo, T. Kisner, N. Krachmalnicoff, A. Kusaka, A. T. Lee, D. Leon, L. Lowry, F. Matsuda, T. Matsumura, M. Navaroli, H. Nishino, H. Paar, J. Peloton, D. Poletti, G. Puglisi, C. L. Reichardt, C. Ross, P. Siritanasak, A. Suzuki, O. Tajima, S. Takatori, and G. Teply, "Performance of a continuously rotating half-wave plate on the POLARBEAR telescope," *Journal of Cosmology and Astroparticle Physics*, vol. 2017, pp. 008–008, may 2017.

[29] M. F. Takayuki, *Cosmic Microwave Background Polarization Science and Optical Design of the POLARBEAR and Simons Array Experiments*. PhD thesis, 2017.

[30] T. Murphy, E. M. Sadler, R. D. Ekers, M. Massardi, P. J. Hancock, E. Mahony, R. Ricci, S. Burke-Spolaor, M. Calabretta, R. Chhetri, G. De Zotti, P. G. Edwards, J. A. Ekers, C. A. Jackson, M. J. Kesteven, E. Lindley, K. Newton-McGee, C. Phillips, P. Roberts, R. J. Sault, L. Staveley-Smith, R. Subrahmanyan, M. A. Walker, and W. E. Wilson, "The Australia Telescope 20 GHz Survey: the source catalogue," *Monthly Notices of the Royal Astronomical Society*, vol. 402, pp. 2403–2423, 03 2010.

[31] Planck Collaboration, Ade, P. A. R., Aghanim, N., Argüeso, F., Armitage-Caplan, C., Arnaud, M., Ashdown, M., Atrio-Barandela, F., Aumont, J., Baccigalupi, C., Banday, A. J., Barreiro, R. B., Bartlett, J. G., Battaner, E., Beelen, A., Benabed, K., Benoît, A., Benoit-Lévy, A., Bernard, J.-P., Bersanelli, M., Bielewicz, P., Bobin, J., Bock, J. J., Bonaldi, A., Bonavera, L., Bond, J. R., Borrill, J., Bouchet, F. R., Bridges, M., Bucher, M., Burigana, C., Butler, R. C., Cardoso, J.-F., Carvalho, P., Catalano, A., Challinor, A., Chamballu, A., Chen, X., Chiang, H. C., Chiang, L.-Y, Christensen, P. R., Church, S., Clemens, M., Clements, D. L., Colombi, S., Colombo, L. P. L., Couchot, F., Coulais, A., Crill, B. P., Curto, A., Cuttaia, F., Danese, L., Davies, R. D., Davis, R. J., de Bernardis, P., de Rosa, A., de Zotti, G., Delabrouille, J., Delouis, J.-M., Désert, F.-X., Dickinson, C., Diego, J. M., Dole, H., Donzelli, S., Doré, O., Douspis, M., Dupac, X., Efstathiou, G., Enßlin, T. A., Eriksen, H. K., Finelli, F., Forni, O., Frailis, M., Franceschi, E., Galeotta, S., Ganga, K., Giard, M., Giardino, G., Giraud-Héraud, Y., González-Nuevo, J., Górski, K. M., Gratton, S., Gregorio, A., Gruppuso, A., Hansen, F. K., Hanson, D., Harrison, D. L., Henrot-Versillé, S., Hernández-Monteagudo, C., Herranz, D., Hildebrandt, S. R., Hivon, E., Hobson, M., Holmes, W. A., Hornstrup, A., Hovest, W., Huffenberger, K. M., Jaffe, A. H., Jaffe, T. R., Jones, W. C., Juvela, M., Keihänen, E., Keskitalo, R., Kisner, T. S., Kneissl, R., Knoche, J., Knox, L., Kunz, M., Kurki-Suonio, H., Lagache, G., Lähteenmäki, A., Lamarre, J.-M., Lasenby, A., Laureijs, R. J., Lawrence, C. R., Leahy, J. P., Leonardi, R., León-Tavares, J., Leroy, C., Lesgourgues, J., Liguori, M., Lilje, P. B., Linden-Vørnle, M., López-Caniego, M., Lubin, P. M., Macías-Pérez, J. F., Maffei, B., Maino, D., Mandolesi, N., Maris, M., Marshall, D. J., Martin, P. G., Martínez-González, E., Masi, S., Massardi, M., Matarrese, S., Matthai, F., Mazzotta, P., McGehee, P., Meinhold, P. R., Melchiorri, A., Mendes, L., Mennella, A., Migliaccio, M., Mitra, S., Miville-Deschênes, M.-A., Moneti, A., Montier, L., Morgante, G., Mortlock, D., Munshi, D., Murphy, J. A., Naselsky, P., Nati, F., Natoli, P., Negrello, M., Netterfield, C. B., Nørgaard-Nielsen, H. U., Noviello, F., Novikov, D., Novikov, I., O´Dwyer, I. J., Osborne, S., Oxborrow, C. A., Paci, F., Pagano, L., Pajot, F., Paladini, R., Paoletti, D., Partridge, B., Pasian, F., Patanchon, G., Pearson, T. J., Perdereau, O., Perotto, L., Perrotta, F., Piacentini, F., Piat, M., Pierpaoli, E., Pietrobon, D., Plaszczynski, S., Pointecouteau, E., Polenta, G., Ponthieu, N., Popa, L., Poutanen, T., Pratt, G. W., Prézeau, G., Prunet, S., Puget, J.-L., Rachen, J. P., Reach, W. T., Rebolo, R., Reinecke, M., Remazeilles, M., Renault, C., Ricciardi, S., Riller, T., Ristorcelli, I., Rocha, G., Rosset, C., Roudier, G., Rowan-Robinson, M., Rubiño-Martín, J. A., Rusholme, B., Sandri, M., Santos, D., Savini, G., Scott, D., Seiffert, M. D., Shellard, E. P. S., Spencer, L. D., Starck, J.-L., Stolyarov, V., Stompor, R., Sudiwala, R., Sunyaev, R., Sureau, F., Sutton, D., Suur-Uski, A.-S., Sygnet, J.-F., Tauber, J. A., Tavagnacco, D., Terenzi, L., Toffolatti, L., Tomasi, M., Tristram, M., Tucci, M., Tuovinen, J., Türler, M., Umana, G., Valenziano, L., Valiviita, J., Van Tent, B., Varis, J., Vielva, P., Villa, F., Vittorio, N., Wade, L. A., Walter, B., Wandelt, B. D., Yvon, D., Zacchei, A., and Zonca, A., "Planck 2013 results. xxviii. the planck catalogue of compact sources," *A&A*, vol. 571, p. A28, 2014.

[32] T. Tomaru, M. Hazumi, A. T. Lee, P. Ade, K. Arnold, D. Barron, J. Borrill, S. Chapman, Y. Chinone, M. Dobbs, J. Errard, G. Fabbian, A. Ghribi, W. Grainger, N. Halverson,

M. Hasegawa, K. Hattori, W. L. Holzapfel, Y. Inoue, S. Ishii, Y. Kaneko, B. Keating, Z. Kermish, N. Kimura, T. Kisner, W. Kranz, F. Matsuda, T. Matsumura, H. Morii, M. J. Myers, H. Nishino, T. Okamura, E. Quealy, C. L. Reichardt, P. L. Richards, D. Rosen, C. Ross, A. Shimizu, M. Sholl, P. Siritanasak, P. Smith, N. Stebor, R. Stompor, A. Suzuki, J. ichi Suzuki, S. Takada, K. ichi Tanaka, and O. Zahn, "The POLARBEAR-2 experiment," in *Millimeter, Submillimeter, and Far-Infrared Detectors and Instrumentation for Astronomy VI* (W. S. Holland, ed.), vol. 8452, pp. 437 – 446, International Society for Optics and Photonics, SPIE, 2012.

[33] Y. Inoue, N. Stebor, P. A. R. Ade, Y. Akiba, K. Arnold, A. E. Anthony, M. Atlas, D. Barron, A. Bender, D. Boettger, J. Borrilll, S. Chapman, Y. Chinone, A. Cukierman, M. Dobbs, T. Elleflot, J. Errard, G. Fabbian, C. Feng, A. Gilbert, N. W. Halverson, M. Hasegawa, K. Hattori, M. Hazumi, W. L. Holzapfel, Y. Hori, G. C. Jaehnig, A. H. Jaffe, N. Katayama, B. Keating, Z. Kermish, R. Keskitalo, T. Kisner, M. L. Jeune, A. T. Lee, E. M. Leitch, E. Linder, F. Matsuda, T. Matsumura, X. Meng, H. Morii, M. J. Myers, M. Navaroli, H. Nishino, T. Okamura, H. Paar, J. Peloton, D. Poletti, G. Rebeiz, C. L. Reichardt, P. L. Richards, C. Ross, D. E. Schenck, B. D. Sherwin, P. Siritanasak, G. Smecher, M. Sholl, B. Steinbach, R. Stompor, A. Suzuki, J. Suzuki, S. Takada, S. Takakura, T. Tomaru, B. Wilson, A. Yadav, H. Yamaguchi, and O. Zahn, "Thermal and optical characterization for POLARBEAR-2 optical system," in *Millimeter, Submillimeter, and Far-Infrared Detectors and Instrumentation for Astronomy VII* (W. S. Holland and J. Zmuidzinas, eds.), vol. 9153, pp. 1018 – 1026, International Society for Optics and Photonics, SPIE, 2014.

[34] J. C. Mather, "Bolometer noise: nonequilibrium theory," *Appl. Opt.*, vol. 21, pp. 1125–1129, Mar 1982.

[35] P. L. Richards, "Bolometers for infrared and millimeter waves," *Journal of Applied Physics*, vol. 76, no. 1, pp. 1–24, 1994.

[36] C. A. Hill, S. M. M. Bruno, S. M. Simon, A. Ali, K. S. Arnold, P. C. Ashton, D. Barron, S. Bryan, Y. Chinone, G. Coppi, K. T. Crowley, A. Cukierman, S. Dicker, J. Dunkley, G. Fabbian, N. Galitzki, P. A. Gallardo, J. E. Gudmundsson, J. Hubmayr, B. Keating, A. Kusaka, A. T. Lee, F. Matsuda, P. D. Mauskopf, J. McMahon, M. D. Niemack, G. Puglisi, M. S. Rao, M. Salatino, C. Sierra, S. Staggs, A. Suzuki, G. Teply, J. N. Ullom, B. Westbrook, Z. Xu, and N. Zhu, "BoloCalc: a sensitivity calculator for the design of Simons Observatory," in *Millimeter, Submillimeter, and Far-Infrared Detectors and Instrumentation for Astronomy IX* (J. Zmuidzinas and J.-R. Gao, eds.), vol. 10708, pp. 698 – 718, International Society for Optics and Photonics, SPIE, 2018.

[37] A. Suzuki, K. Arnold, J. Edwards, G. Engargiola, W. Holzapfel, B. Keating, A. T. Lee, X. F. Meng, M. J. Myers, R. O'Brient, E. Quealy, G. Rebeiz, P. L. Richards, D. Rosen, and P. Siritanasak, "Multi-chroic dual-polarization bolometric detectors for studies of the cosmic microwave background," *Journal of Low Temperature Physics*, vol. 176, pp. 650–656, Sep 2014.

[38] P. Siritanasak, C. Aleman, K. Arnold, A. Cukierman, M. Hazumi, K. Kazemzadeh, B. Keating, T. Matsumura, A. T. Lee, C. Lee, E. Quealy, D. Rosen, N. Stebor, and A. Suzuki, "The broadband anti-reflection coated extended hemispherical silicon lenses for polarbear-2 experiment," *Journal of Low Temperature Physics*, vol. 184, pp. 553–558, Aug 2016.

[39] A. N. Bender, J.-F. Cliche, T. de Haan, M. A. Dobbs, A. J. Gilbert, J. Montgomery, N. Rowlands, G. M. Smecher, K. Smith, and A. Wilson, "Digital frequency domain multiplexing readout electronics for the next generation of millimeter telescopes," in *Millimeter, Submillimeter, and Far-Infrared Detectors and Instrumentation for Astronomy VII* (W. S. Holland and J. Zmuidzinas, eds.), vol. 9153, pp. 430 – 444, International Society for Optics and Photonics, SPIE, 2014.

[40] K. Hattori, Y. Akiba, K. Arnold, D. Barron, A. Bender, M. A. Dobbs, T. de Haan, N. Harrington, M. Hasegawa, M. Hazumi, W. L. Holzapfel, Y. Hori, B. G. Keating, A. T. Lee, J. Montgomery, H. Morii, M. J. Myers, K. Rotermund, I. Shirley, G. M. Smecher, N. Stebor, A. Suzuki, and T. Tomaru, "Optimization of cold resonant filters for frequency domain multiplexed readout of POLARBEAR-2," in *Millimeter, Submillimeter, and Far-Infrared Detectors and Instrumentation for Astronomy VII* (W. S. Holland and J. Zmuidzinas, eds.), vol. 9153, pp. 445 – 453, International Society for Optics and Photonics, SPIE, 2014.

[41] D. Barron, P. A. R. Ade, Y. Akiba, C. Aleman, K. Arnold, M. Atlas, A. Bender, J. Borrill, S. Chapman, Y. Chinone, A. Cukierman, M. Dobbs, T. Elleflot, J. Errard, G. Fabbian, G. Feng, A. Gilbert, N. W. Halverson, M. Hasegawa, K. Hattori, M. Hazumi, W. L. Holzapfel, Y. Hori, Y. Inoue, G. C. Jaehnig, N. Katayama, B. Keating, Z. Kermish, R. Keskitalo, T. Kisner, M. L. Jeune, A. T. Lee, F. Matsuda, T. Matsumura, H. Morii, M. J. Myers, M. Navroli, H. Nishino, T. Okamura, J. Peloton, G. Rebeiz, C. L. Reichardt, P. L. Richards, C. Ross, M. Sholl, P. Siritanasak, G. Smecher, N. Stebor, B. Steinbach, R. Stompor, A. Suzuki, J. Suzuki, S. Takada, T. Takakura, T. Tomaru, B. Wilson, H. Yamaguchi, and O. Zahn, "Development and characterization of the readout system for POLARBEAR-2," in *Millimeter, Submillimeter, and Far-Infrared Detectors and Instrumentation for Astronomy VII* (W. S. Holland and J. Zmuidzinas, eds.), vol. 9153, pp. 993 – 1000, International Society for Optics and Photonics, SPIE, 2014.

[42] K. Rotermund, B. Barch, S. Chapman, K. Hattori, A. Lee, N. Palaio, I. Shirley, A. Suzuki, and C. Tran, "Planar lithographed superconducting lc resonators for frequency-domain multiplexed readout systems," *Journal of Low Temperature Physics*, vol. 184, pp. 486–491, Jul 2016.

[43] J. S. Avva, P. A. R. Ade, Z. Ahmed, A. J. Anderson, J. E. Austermann, R. B. Thakur, D. Barron, A. N. Bender, B. A. Benson, J. E. Carlstrom, F. W. Carter, T. Cecil, C. L. Chang, J. F. Cliche, A. Cukierman, E. V. Denison, T. de Haan, J. Ding, M. A. Dobbs, D. Dutcher, T. Elleflot, W. Everett, A. Foster, R. N. Gannon, A. Gilbert, J. C. Groh, N. W. Halverson, A. H. Harke-Hosemann, N. L. Harrington, M. Hasegawa, K. Hattori, J. W. Henning, G. C. Hilton, W. L. Holzapfel, Y. Hori, N. Huang, K. D. Irwin, O. B. Jeong, M. Jonas, T. Khaire, A. M. Kofman, M. Korman, D. Kubik, S. Kuhlmann, C. L. Kuo,

A. T. Lee, A. E. Lowitz, S. S. Meyer, J. Montgomery, A. Nadolski, T. Natoli, H. Nguyen, H. Nishino, G. I. Noble, V. Novosad, S. Padin, Z. Pan, J. Pearson, C. M. Posada, A. Rahlin, K. Rotermund, J. E. Ruhl, L. J. Saunders, J. T. Sayre, I. Shirley, E. Shirokoff, G. Smecher, J. A. Sobrin, A. A. Stark, K. T. Story, A. Suzuki, Q. Y. Tang, K. L. Thompson, C. Tucker, L. R. Vale, K. Vanderlinde, J. D. Vieira, G. Wang, N. Whitehorn, V. Yefremenko, K. W. Yoon, and M. R. Young, "Design and assembly of spt-3g cold readout hardware," *Journal of Low Temperature Physics*, vol. 193, pp. 547–555, Nov 2018.

[44] A. N. Bender, P. A. R. Ade, Z. Ahmed, A. J. Anderson, J. S. Avva, K. Aylor, P. S. Barry, R. B. Thakur, B. A. Benson, L. S. Bleem, S. Bocquet, K. Byrum, J. E. Carlstrom, F. W. Carter, T. W. Cecil, C. L. Chang, H.-M. Cho, J. F. Cliche, T. M. Crawford, A. Cukierman, T. de Haan, E. V. Denison, J. Ding, M. A. Dobbs, S. Dodelson, D. Dutcher, W. Everett, A. Foster, J. Gallicchio, A. Gilbert, J. C. Groh, S. T. Guns, N. W. Halverson, A. H. Harke-Hosemann, N. L. Harrington, J. W. Henning, G. C. Hilton, G. P. Holder, W. L. Holzapfel, N. Huang, K. D. Irwin, O. B. Jeong, M. Jonas, A. Jones, T. S. Khaire, L. Knox, A. M. Kofman, M. Korman, D. L. Kubik, S. Kuhlmann, C.-L. Kuo, A. T. Lee, E. M. Leitch, A. E. Lowitz, S. S. Meyer, D. Michalik, J. Montgomery, A. Nadolski, T. Natoli, H. Ngyuen, G. I. Noble, V. Novosad, S. Padin, Z. Pan, J. Pearson, C. M. Posada, W. Quan, S. Raghunathan, A. Rahlin, C. L. Reichardt, J. E. Ruhl, J. T. Sayre, E. Shirokoff, G. Smecher, J. A. Sobrin, A. A. Stark, K. T. Story, A. Suzuki, K. L. Thompson, C. Tucker, L. R. Vale, K. Vanderlinde, J. D. Vieira, G. Wang, N. Whitehorn, W. L. K. Wu, V. Yefremenko, K. W. Yoon, and M. R. Young, "Year two instrument status of the SPT-3G cosmic microwave background receiver," in *Millimeter, Submillimeter, and Far-Infrared Detectors and Instrumentation for Astronomy IX* (J. Zmuidzinas and J.-R. Gao, eds.), vol. 10708, pp. 1 – 21, International Society for Optics and Photonics, SPIE, 2018.

[45] S.-F. Lee, J. M. Gildemeister, W. Holmes, A. T. Lee, and P. L. Richards, "Voltage-biased superconducting transition-edge bolometer with strong electrothermal feedback operated at 370 mk," *Appl. Opt.*, vol. 37, pp. 3391–3397, Jun 1998.

[46] K. Irwin and G. Hilton, *Transition-Edge Sensors*, pp. 63–150. Berlin, Heidelberg: Springer Berlin Heidelberg, 2005.

[47] M. A. Dobbs, M. Lueker, K. A. Aird, A. N. Bender, B. A. Benson, L. E. Bleem, J. E. Carlstrom, C. L. Chang, H.-M. Cho, J. Clarke, T. M. Crawford, A. T. Crites, D. I. Flanigan, T. de Haan, E. M. George, N. W. Halverson, W. L. Holzapfel, J. D. Hrubes, B. R. Johnson, J. Joseph, R. Keisler, J. Kennedy, Z. Kermish, T. M. Lanting, A. T. Lee, E. M. Leitch, D. Luong-Van, J. J. McMahon, J. Mehl, S. S. Meyer, T. E. Montroy, S. Padin, T. Plagge, C. Pryke, P. L. Richards, J. E. Ruhl, K. K. Schaffer, D. Schwan, E. Shirokoff, H. G. Spieler, Z. Staniszewski, A. A. Stark, K. Vanderlinde, J. D. Vieira, C. Vu, B. Westbrook, and R. Williamson, "Frequency multiplexed superconducting quantum interference device readout of large bolometer arrays for cosmic microwave background measurements," *Review of Scientific Instruments*, vol. 83, no. 7, p. 073113, 2012.

[48] T. Elleflot, Y. Akiba, K. Arnold, J. Avva, D. Barron, A. N. Bender, A. Cukierman, T. de Haan, M. Dobbs, J. Groh, M. Hasegawa, M. Hazumi, W. Holzapfel, L. Howe, G. Jaehnig, B. Keating, A. Kusaka, A. T. Lee, L. Lowry, J. Montgomery, H. Nishino, C. Raum, K. M. Rotermund, M. Silva-Feaver, A. Suzuki, B. Westbrook, and N. Whitehorn, "Detector and readout assembly and characterization for the simons array," *Journal of Low Temperature Physics*, vol. 193, pp. 1094–1102, Dec 2018.

[49] A. I. Braginski and J. Clarke, *Introduction*, ch. 1, pp. 1–28. John Wiley & Sons, Ltd, 2005.

[50] T. M. Lanting, *Multiplexed readout of superconducting bolometers for cosmological observations*. PhD thesis, University of California, Berkeley, Jan 2006.

[51] A. N. Bender, A. J. Anderson, J. S. Avva, P. A. R. Ade, Z. Ahmed, P. S. Barry, R. B. Thakur, B. A. Benson, L. Bryant, K. Byrum, J. E. Carlstrom, F. W. Carter, T. W. Cecil, C. L. Chang, H. M. Cho, J. F. Cliche, A. Cukierman, T. de Haan, E. V. Denison, J. Ding, M. A. Dobbs, D. Dutcher, W. Everett, K. R. Ferguson, A. Foster, J. Fu, J. Gallicchio, A. E. Gambrel, R. W. Gardner, A. Gilbert, J. C. Groh, S. Guns, R. Guyser, N. W. Halverson, A. H. Harke-Hosemann, N. L. Harrington, J. W. Henning, G. C. Hilton, W. L. Holzapfel, D. Howe, N. Huang, K. D. Irwin, O. B. Jeong, M. Jonas, A. Jones, T. S. Khaire, A. M. Kofman, M. Korman, D. L. Kubik, S. Kuhlmann, C. L. Kuo, A. T. Lee, E. M. Leitch, A. E. Lowitz, S. S. Meyer, D. Michalik, J. Montgomery, A. Nadolski, T. Natoli, H. Nguyen, G. I. Noble, V. Novosad, S. Padin, Z. Pan, P. Paschos, J. Pearson, C. M. Posada, W. Quan, A. Rahlin, D. Riebel, J. E. Ruhl, J. T. Sayre, E. Shirokoff, G. Smecher, J. A. Sobrin, A. A. Stark, J. Stephen, K. T. Story, A. Suzuki, K. L. Thompson, C. Tucker, L. R. Vale, K. Vanderlinde, J. D. Vieira, G. Wang, N. Whitehorn, V. Yefremenko, K. W. Yoon, and M. R. Young, "On-sky performance of the spt-3g frequency-domain multiplexed readout," 2019.

[52] J. Montgomery, "Development of multiplexed bolometer readout electronics for mm-wave space astronomy ," Master's thesis, McGill University, 2015.

[53] D. Dutcher, P. A. R. Ade, Z. Ahmed, A. J. Anderson, J. S. Avva, R. B. Thakur, A. N. Bender, B. A. Benson, J. E. Carlstrom, F. W. Carter, T. W. Cecil, C. L. Chang, J. F. Cliche, A. Cukierman, T. de Haan, J. Ding, M. A. Dobbs, W. Everett, A. Foster, J. Gallicchio, A. Gilbert, J. C. Groh, A. H. Harke-Hosemann, S. T. Guns, N. W. Halverson, N. L. Harrington, J. W. Henning, W. L. Holzapfel, N. Huang, K. D. Irwin, O. B. Jeong, M. Jonas, T. S. Khaire, A. M. Kofman, M. Korman, D. L. Kubik, S. Kuhlmann, C.-L. Kuo, A. E. Lowitz, A. T. Lee, S. S. Meyer, D. Michalik, J. Montgomery, A. Nadolski, T. Natoli, H. Nguyen, G. I. Noble, V. Novosad, S. Padin, Z. Pan, J. Pearson, C. M. Posada, W. Quan, A. Rahlin, J. E. Ruhl, J. T. Sayre, E. Shirokoff, G. Smecher, J. A. Sobrin, A. A. Stark, K. T. Story, A. Suzuki, K. L. Thompson, C. Tucker, K. Vanderlinde, J. D. Vieira, G. Wang, N. Whitehorn, V. Yefremenko, K. W. Yoon, and M. R. Young, "Characterization and performance of the second-year SPT-3G focal plane," in *Millimeter, Submillimeter, and Far-Infrared Detectors and Instrumentation for Astronomy IX* (J. Zmuidzinas and J.-R. Gao, eds.), vol. 10708, pp. 246 – 258, International Society for Optics and Photonics, SPIE, 2018.

[54] A. J. Anderson, P. A. R. Ade, Z. Ahmed, J. S. Avva, P. S. Barry, R. B. Thakur, A. N. Bender, B. A. Benson, L. Bryant, K. Byrum, J. E. Carlstrom, F. W. Carter, T. W. Cecil, C. L. Chang, H.-M. Cho, J. F. Cliche, A. Cukierman, T. de Haan, E. V. Denison, J. Ding, M. A. Dobbs, D. Dutcher, W. Everett, K. R. Ferguson, A. Foster, J. Fu, J. Gallicchio, A. E. Gambrel, R. W. Gardner, A. Gilbert, J. C. Groh, S. T. Guns, R. Guyser, N. W. Halverson, A. H. Harke-Hosemann, N. L. Harrington, J. W. Henning, G. C. Hilton, W. L. Holzapfel, D. Howe, N. Huang, K. D. Irwin, O. B. Jeong, M. Jonas, A. Jones, T. S. Khaire, A. M. Kofman, M. Korman, D. L. Kubik, S. Kuhlmann, C.-L. Kuo, A. T. Lee, E. M. Leitch, A. E. Lowitz, S. S. Meyer, D. Michalik, J. Montgomery, A. Nadolski, T. Natoli, H. Nguyen, G. I. Noble, V. Novosad, S. Padin, Z. Pan, P. Paschos, J. Pearson, C. M. Posada, W. Quan, A. Rahlin, D. Riebel, J. E. Ruhl, J. T. Sayre, E. Shirokoff, G. Smecher, J. A. Sobrin, A. A. Stark, J. Stephen, K. T. Story, A. Suzuki, K. L. Thompson, C. Tucker, L. R. Vale, K. Vanderlinde, J. D. Vieira, G. Wang, N. Whitehorn, V. Yefremenko, K. W. Yoon, and M. R. Young, "Performance of al–mn transition-edge sensor bolometers in spt-3g," *Journal of Low Temperature Physics*, Nov 2019.

[55] B. Wilson, M. Atlas, P. Lowell, S. Moyerman, N. Stebor, J. Ullom, and B. Keating, "A robust cooling platform for nis junction refrigeration and sub-kelvin cryogenic systems," *Journal of Low Temperature Physics*, vol. 176, pp. 243–248, Aug 2014.